Author: Torren, Alexander J.H. van der
Title: Growing oxide thin films in a low-energy electron microscope
Issue Date: 2016-12-05

Growing oxide thin films in a Low-Energy Electron Microscope

Proefschrift

ter verkrijging van
de graad van Doctor aan de Universiteit Leiden,
op gezag van Rector Magnificus prof. mr. C.J.J.M. Stolker,
volgens besluit van het College voor Promoties
te verdedigen op 5 december 2016
klokke 11:15 uur

door

Alexander Johannes Hendrikus van der Torren

geboren te Heerlen
in 1987

Promotor:	Prof. dr. J. Aarts	
Co-Promotor:	Dr. ir. S.J. van der Molen	
Promotiecommissie:	Prof. dr. R. Dittmann	(Forschungszentrum Jülich / RWTH Aachen)
	Prof. dr. A.J.H.M. Rijnders	(Universiteit Twente)
	Dr. A. Caviglia	(Technische Universiteit Delft)
	Prof. dr. E. R. Eliel	
	Prof. dr. ir. T.H. Oosterkamp	

Casimir PhD series, Delft-Leiden 2016-32
ISBN 978-90-8593-276-5
An electronic version of this thesis can be found at
`https://openaccess.leidenuniv.nl`.

The work described in this thesis is supported by the Netherlands Organisation for Scientific Research (NWO) by means of a ”NWO Groot” grant and by the Leiden-Delft Consortium NanoFront.

The work is part of the research programmes NWOnano and DESCO, administered by the Foundation for Fundamental Research on Matter (FOM), which is part of NWO.

The cover shows images produced by various types of measurements that can be performed with the Leiden low-energy electron microscope.

Contents

1

Introduction

1.1 Introduction

Silicon is the workhorse for modern electronics. The performance of Si-based devices is mainly boosted by their miniaturization, which will soon be limited by quantum mechanical obstacles. A way to overcome this is to find other materials than the covalent semiconductors, that can be used in electronics. Silicon is a conventional semiconductor where the conductance or metallicity derives from exciting electrons over the band gap, or doping the material with either electrons or holes. In all cases, the number of charge carriers is low, with in particular long screening lengths for electric fields as a consequence. In silicon, the charge carriers behave as independent particles, with little interaction between them selves or with the lattice. In contrast, in transition metal oxides (TMO) the metallicity is determined by details of the electron-electron interaction between the 3d electrons of the transition metal ion. The carrier concentration can be very high, in the order of an electron per atom, and screening lengths small. Also, the interactions can lead to complex phenomena such as high-temperature superconductivity or colossal magnetoresistance. Special properties and phenomena can also be achieved at the interface between different oxides. As Herbert Kroemer said during his Nobel lecture: "Often, it may be said that the interface is the device" [1]. Already many devices based on conventional semiconductors exploit interfaces, for example transistors, lasers, memory and solar cells. The interfaces between TMOs, however open up a new world of interesting physics.

Research of TMO devices was long held back by the difficulties in growing TMO multilayers. Developments in the last decades have improved this. The ability to obtain well-defined interfaces by fabricating surfaces consisting of only a single well-defined ionic or atomic plane, the so-called singly-terminated surface, has been a key step to obtain sharp interfaces[2]. Furthermore, the ability to grow clean multilayers by molecular-beam epitaxy (MBE)[3], and pulsed laser deposition (PLD)[4] has been of utmost importance. Moreover, the development of in-situ reflection high-energy electron diffraction (RHEED)[5] for PLD at elevated pressures has led to thickness control down to the unit cell range.

To further optimize the material properties more information during the growth process would be of great value. Especially the structural and electronic properties are important for the resulting film. Basic structural information can be obtained from the diffraction pattern obtained by RHEED but, electronic information is mostly missing. Other analysis techniques have been hampered by the extreme conditions, i.e. high temperature and oxygen background pressures. The requirements of surface sensitivity and non-invasive, non-contact techniques limit the analysis to electron optical techniques.

As most widely used system to grow TMOs we focus on PLD. We extend the possibility for in-situ film growth analysis by introducing low-energy electron microscopy (LEEM), with in-situ PLD system, as a new technique in this field. RHEED does not allow for spatial resolution and is more difficult to analyze than low-energy electron diffraction (LEED). Low-energy electron microscopy (LEEM) is able to combine spatial resolution with LEED. New developments, partially in our lab, allow one to investigate the electronic structure of a surface or thin film[6]. This extends LEEM to a versatile set-up for material science, combining structural and electronic properties with lateral resolution and fast investigation.

An ideal device for electronics would be a two dimensional electron gas (2-DEG) at the interface between two insulators, with high electron mobility, tunable by a gate and working at room temperature. The 2-DEG found between the TMO band-insulators $LaAlO_3$ and $SrTiO_3$ was a remarkable discovery[7], which comes close to this ideal device. However, the exact origin of this 2-DEG is still not understood. In this thesis we will use LEEM as a method to investigate the film properties of the hetero-structure during growth.

1.2 Thesis outline

The main material system to be investigated is the $LaAlO_3/SrTiO_3$ interface. This will be introduced in chapter 2 and the method used for studying the interface, LEEM with its full set of subtechniques, in chapter 3. While the $SrTiO_3$ building block has already been studied in LEEM by Hesselberth *et al.*[8] we continue with the other building block, $LaAlO_3$, in chapter 4. For the growth studies we require a PLD system. Its development is described in chapter 5. Also its abilities are demonstrated by the growth of homoepitaxial $SrTiO_3$. With the building blocks and equipment in place we study the formation of the $LaAlO_3/SrTiO_3$ hetero-structure in chapter 6. Finally, we use our knowledge about the $LaAlO_3/SrTiO_3$ hetero-structure to investigate $LaAlO_3/SrTiO_3$ on $Ca_2Nb_3O_{10}$ nanosheets deposited on Si, in chapter 7. In this chapter everything comes together and the spatial resolution of the LEEM is of great importance.

References

[1] H. Kroemer, *Nobel Lecture: Quasielectric fields and band offsets: teaching electrons new tricks*, Reviews of Modern Physics **73**, 783 (2001).

[2] M. Kawasaki, K. Takahashi, T. Maeda, R. Tsuchiya, M. Shinohara, O. Ishiyama, T. Yonezawa, M. Yoshimoto, and H. Koinuma, *Atomic Control of the* $SrTiO_3$ *Crystal Surface*, Science **266**, 1540 (1994).

[3] D. G. Schlom, J. N. Eckstein, E. S. Hellman, S. K. Streiffer, J. S. H. Jr, M. R. Beasley, J. C. Bravman, T. H. Geballe, C. Webb, K. E. v. Dessonneck, and F. Turner, *Molecular beam epitaxy of layered DyBaCuO compounds*, Applied Physics Letters **53**, 1660 (1988).

[4] D. Dijkkamp, T. Venkatesan, X. D. Wu, S. A. Shaheen, N. Jisrawi, Y. H. Min-Lee, W. L. McLean, and M. Croft, *Preparation of YBaCu oxide superconductor thin films using pulsed laser evaporation from high Tc bulk material*, Applied Physics Letters **51**, 619 (1987).

[5] G. J. H. M. Rijnders, G. Koster, D. H. A. Blank, and H. Rogalla, *In situ monitoring during pulsed laser deposition of complex oxides using reflection high energy electron diffraction under high oxygen pressure*, Applied Physics Letters **70**, 1888 (1997).

[6] J. Jobst, J. Kautz, D. Geelen, R. M. Tromp, and S. J. van der Molen, *Nanoscale measurements of unoccupied band dispersion in few-layer graphene*, Nature Communications **6**, 8926 (2015).

[7] A. Ohtomo and H. Y. Hwang, *A high-mobility electron gas at the* $LaAlO_3/SrTiO_3$ *heterointerface*, Nature **427**, 423 (2004).

[8] M. B. S. Hesselberth, S. J. v. d. Molen, and J. Aarts, *The surface structure of* $SrTiO_3$ *at high temperatures under influence of oxygen*, Applied Physics Letters **104**, 051609 (2014).

2

The $LaAlO_3/SrTiO_3$ interface

$LaAlO_3$ and $SrTiO_3$ are cubic perovskites and wide band gap insulators which differ in one aspect: $SrTiO_3$ is a non-polar material, where each layer stacked along a principal axis of the cube is change-neutral. $LaAlO_3$ is polar, with layers having alternating charges of ±e per unit cell. In 2004, Ohtomo and Wang made the remarkable discovery of a two dimensional electron gas (2-DEG) forming at the interface. Such a conducting layer has potential for applications, but despite much reseurch, many details of its formation are still unclear. This chapter describes the basic understanding of the $LaAlO_3/SrTiO_3$ interface.

2.1 Transition-metal oxides

Transition metal oxides (TMO's) show many exciting phenomena compared to simple covalent semiconductors. Strong Coulomb repulsion between the 3d electrons of the TM ion, parametrized by U, tend to localize them on the atoms, leading to an insulating state. The energy gap to the conducting states is roughly determined by $U - 2zt$, where t is the site-to-site transfer integral of the d-electrons, and z is the number of nearest neighbors. If $t << U$, as is often the case, this leads to the so-called Mott-insulating state. Such an insulator is very different from covalent semiconductors such as Si, and GaAs, where the four hybridized sp^3 electrons form shared pairs with four nearest neighbor atoms. The electrons localize between the atoms, as a result of the competition between electron-nucleus attraction and electron-electron repulsion. The Mott state is charge-ordered, but the subtle interplay between charge, spin, and lattice structure also leads to spin and orbital order. Figure 2.1a and b show the doping phase diagrams of $La_{1\text{-}x}Sr_xMnO_3$ and $La_{2\text{-}x}Sr_xCuO_4$, respectively. In (La,Sr)MnO_3 the Sr^{2+} ion dopes holes into the MnO_2 complex, leading to a mix of Mn^{3+} and Mn^{4+} valencies. The latter results in a hole in the d-band and (at low temperatures) a change from an antiferromagnetic canted insulator (CI in Fig. 2.1a) to a ferromagnetic metal (FM). This state becomes paramagnetic insulating at higher temperatures, resulting in the well-known colossal magnetoresistance effect. In (La,Sr_2)CuO_4 the doping leads to even more dramatic effects. Doping holes into the CuO_2 complexes now yields high-temperature superconductivity.

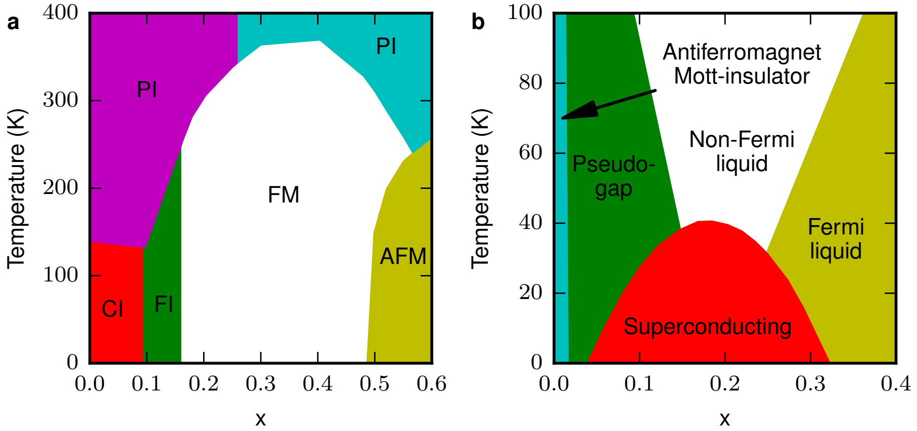

FIGURE 2.1: Phase diagram of (a) $La_{1\text{-}x}Sr_xMnO_3$, based on data from Ref.[1–3]. PM, PI, FM, AFM, FI, and CI denote, paramagnetic metal, paramagnetic insulator, ferromagnetic metal, antiferromagnetic metal, ferromagnetic insulator, and spin-canted insulator states, respectively. (b) $La_{2\text{-}x}Sr_xCuO_4$, based on data from Ref.[4].

The effective masses of charge carriers in TMOs are an order of magnitude higher than in semiconductors, which is partly due to the strong coupling with the lattice and the reorientation possibilities for the oxygen octahedra. Together with high carrier concentrations this leads to short screening lengths for electric fields, in the order of 1 to 100 nm.

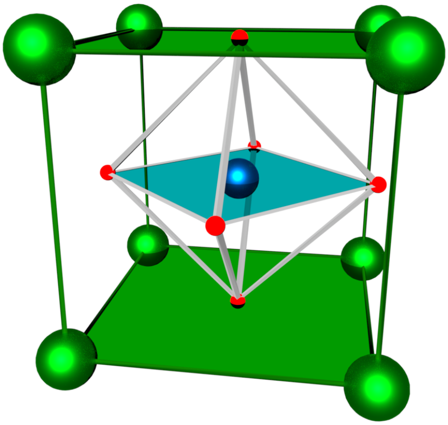

FIGURE 2.2: Unit cells of the perovskite structure with the ABO_3 chemical formula. Here A is in green (corner), B in blue (center) and O in red (cube faces). Furthermore, the AO plane is shown in green and the BO_2 plane in blue.

A much studied structure of TMOs is the cubic perovskite structure (Fig. 2.2). The chemical structure is ABO_3. Here the A is an alkaline earth metal or a rare earth metal and the B is a transition metal or a metalloid. Under pressure and temperature the structure can change from cubic to orthorhombic, tetragonal, rhombohedral or monoclinic. Along the (001) direction the structure can be seen as, built up from AO and BO_2 planes, indicated with blue and green planes in figure 2.2.

In this thesis I will focus on the 2-dimensional electron gas between the TMOs $SrTiO_3$ and $LaAlO_3$. Strictly speaking, $SrTiO_3$ is a TMO, but not a Mott-insulator, the Ti^{4+} has an empty d-shell. However, doping can fill the Ti d-shell in the $SrTiO_3$, showing TMO physics. Moreover, $LaAlO_3$ is not strictly a TMO, since Al is not a transition metal, but structure and physics is close to the one of the TMOs and it is in general seen as part of the group. $SrTiO_3$ and $LaAlO_3$ are both perovskites and insulators with bandgaps of 3.2 eV[5] and 5.6 eV[6] respectively. Their lattice constants (STO: 3.905 Å[7], LAO: 3.789 Å[8]) have only a small mismatch of 3 %, resulting in epitaxial growth when stacking the two materials. Both materials are widely used as substrates, and are easily commercially available as single crystals. As-received crystals have a mixed terminated surface with both areas with AO and BO_2 planes. For $SrTiO_3$ the termination can chemically be changed to TiO_2[9,10], whereas the SrO termination can only be made reliably by growing a monolayer of

SrO on a TiO_2 terminated surface. For $LaAlO_3$ the termination is more complex and it will be discussed in chapter 4.

2.2 The $LaAlO_3/SrTiO_3$ Interface

At the interface of $LaAlO_3$ and $SrTiO_3$ a conducting interface is found. This is a different interface than in covalent semiconductors. Where for instance at the interface of the covalent semiconductors $GaAs/Al_xGa_{1-x}As$ the mobile carriers move into two-dimensional subbands within the quantum well generated by band bending, at the $LaAlO_3/SrTiO_3$ interface multiple quantum wells are found given by the ionic potentials of the TiO_6 octahedra (see fig. 2.3). The electrons are subject to the correlations of the Ti 3d bands and form an two dimensional electron liquid (2-DEL) rather than a gas[12]. This electron liquid is strongly confined, which is very advantageous for screening and switching applications as well as for miniaturization of devices. For historic reasons we will often still use 2-DEG instead of 2-DEL.

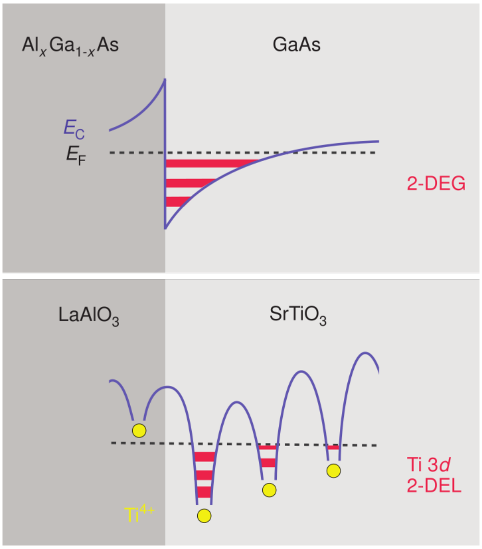

FIGURE 2.3: Comparison between the 2-DEG at the $GaAs/Al_xGa_{1-x}As$ interface (top) and the 2-DEL at the $LaAlO_3/SrTiO_3$ interface (bottom). Taken from Ref.[11].

The interface can actually be made in two different configurations. First, when the $SrTiO_3$ is TiO_2 terminated, growing epitaxial $LaAlO_3$ results in a TiO_2/LaO interface, which can become conducting. Second, when the terminating layer is SrO the interface will be SrO/AlO_2. This interface turns out to be insulating[13,14]. For the conducting interface, Thiel *et al.*[15] found that the surface only becomes conducting when the $LaAlO_3$ layer consists of four or more unit cells. One and two unit cells result in a fully insulating interface, while a three-unit-cell interface can be made conducting by gating.

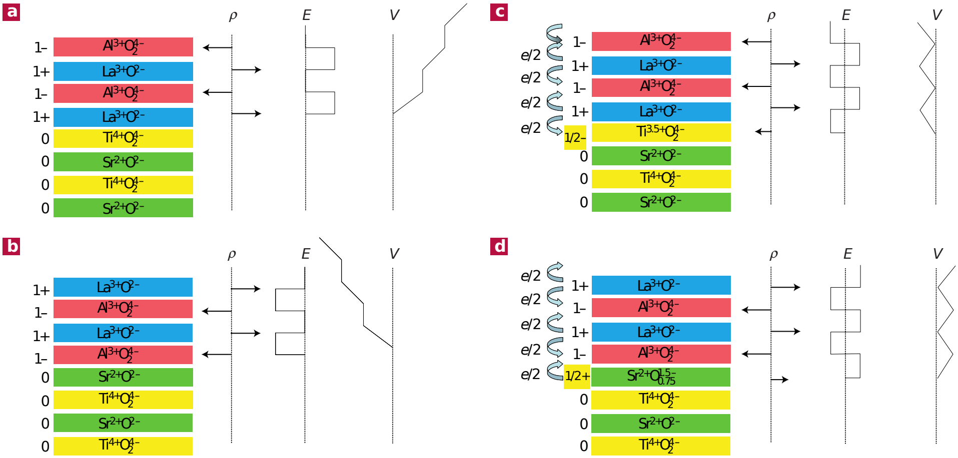

FIGURE 2.4: Illustration of the polar catastrophe model in the $LaAlO_3/SrTiO_3$ hetero-structure. The stacking sequence of $LaAlO_3$ and $SrTiO_3$ layers is shown with their oxidation levels and final net charge per layer. In the diagrams ρ is the net charge per layer, E the resulting electric field and V the potential buildup. a and b illustrate the potential buildup for a n-type (TiO_2/LaO) and p-type (SrO/AlO_2) interface respectively, leading to a diverging potential. In c half an electron charge is transferred from the surface to the interface to avoid the divergence. For the p-type interface, one would expect the electron is transferred from the interface to the surface. However, an energetically more favorable structural reconstruction[16] appears. Image from Ref.[14].

To understand this remarkable effect of a 2-dimensional electron gas between two insulators, the role of the $SrTiO_3$ and $LaAlO_3$ layers are now further discussed. These building blocks can be described as stacked AO and BO_2 layers as stated earlier. Writing down these layers and their charges we find for the $SrTiO_3$, $Sr^{2+}O^{2-}$ and $Ti^{4+}O_2^{4-}$, both having zero net charge. In contrast, for $LaAlO_3$ the layers are $La^{3+}O^{2-}$ and $Al^{3+}O_2^{4-}$, respectively positive and negatively charged. This is illustrated in figure 2.4. The charged layers in the $LaAlO_3$ can be seen as parallel plate capacitors with a charge ρ, resulting in an electric field E between them, which results in a potential buildup V. Starting from a neutral $SrTiO_3$ layer the potential builds up without bound, as the thickness of $LaAlO_3$ grows (Fig. 2.4a), which is not physically possible. This can be solved by an electronic or structural reconstruction. In the case of an electronic reconstruction, half an electron is transferred from the $LaAlO_3$ surface towards the interface (Fig. 2.4c), resulting in half a free electron per unit cell at the interface creating half the charge at the interface. This is the so called polar catastrophe[13,14] model. This potential buildup fits reasonably well with the transition from insulating to conducting interface at three to four unit cells. Only for four unit cells and more the potential buildup is strong enough for the electron transfer to take place.

The resulting electrons at the interface will change the Ti^{4+} to Ti^{3+}. In that case, we call it a n-type interface. On the other hand if the $SrTiO_3$ surface is SrO terminated the potential buildup is opposite (Fig. 2.4b) and half an electron has to be transferred away from the interface to the $LaAlO_3$ surface (Fig. 2.4d). This would result in a p-type interface as an electron has to be removed from the O-2p band. This is energetically more expensive and a structural reconstruction is more favorable[16] resulting in an insulating interface.

Although this model presents a good description of the conducting interface, it cannot be the full story. In particular core-level X-ray photoemission spectroscopy (XPS) measurements have not been able to measure the potential buildup[17,18]. Furthermore, there is strong evidence for an important role of defects and stoichiometry, which now will be discussed.

2.3 Oxygen vacancies

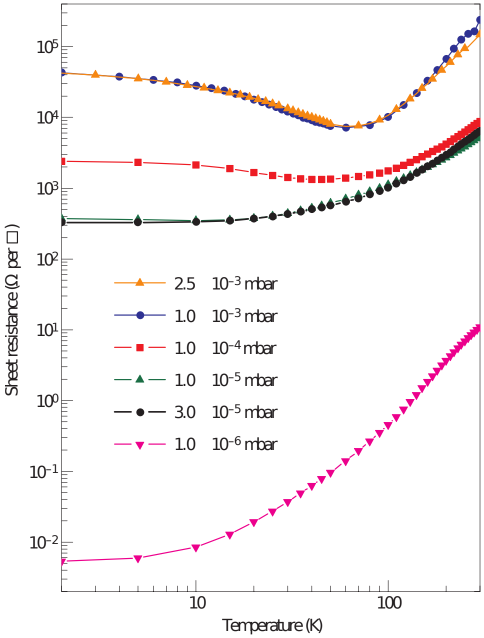

FIGURE 2.5: Sheet resistance as function of temperature of the $LaAlO_3/SrTiO_3$ interface depending on oxygen background pressure during growth as indicated in the figure. Note the minimum who occurs for pressures above 10^{-4} mbar. Taken from Ref.[19].

The number of oxygen vacancies is mainly influenced by the oxygen background pressure during growth and is well described by Brinkman *et al.*[19]. Figure 2.5 summarizes the salient behavior of the sheet resistance of the interface as function of temperature for different values of the oxygen background pressure during growth. At pressures of 1×10^{-6} mbar and lower the amount of oxygen in the $SrTiO_3$ crystal is reduced and bulk conductivity starts to play a role. For pressures above 1×10^{-2} mbar the interface is found the be insulating, while in the intermediate regime different types of physics are found at the interface, such as superconductivity[20–22] and magnetism[19,23–25]. The minimum occurring at pressures above 1×10^{-4} mbar is often connected to the presence of some kind of magnetism. To stay clearly away from bulk conductivity, but preserve UHV conditions in our low-energy electron microscope without taking extra precautions, we decided to use a background pressure of 5×10^{-5} mbar O_2 in the experiments involving the $LaAlO_3/SrTiO_3$ interface.

2.4 Stoichiometry

It has been found that also the stoichiometry of the deposited $LaAlO_3$-layer is of crucial importance for rendering the interface conducting or insulating[26–29]. Warusawithana *et al.*[27] using molecular beam epitaxy (MBE), found that the La/Al ratio has to be smaller than 0.97 to obtain a conducting interface. Breckenfeld *et al.*[30], using PLD, found that at 2 K the interface sheet resistances using 4 % La-deficient $LaAlO_3$ is almost ten orders of magnitude lower than the interface sheet resistance using 5 % La-excess $LaAlO_3$. Also, Dildar *et al.*[26] found that $LaAlO_3$ deposited on $SrTiO_3$ by sputtering in 1 mbar of oxygen showed a La-excess of 7 %, while the interface was insulating. This stoichiometry dependence emphasizes the importance of defects in the $SrTiO_3$ and $LaAlO_3$ during the formation of the interface conductance. In particular, it has been pointed out that excess Al can substitute on the La-sites, while La excess leads to Al_2O_3-vacancy complexes[27], with significant differences in the way the charge distribution problem can be solved. However, how this exactly leads to either a conducting or a non-conducting interface is not yet fully understood.

The stoichiometry issue is the more important since it is strongly influenced by the growth conditions. Growth of $LaAlO_3/SrTiO_3$ interfaces is most frequently performed by pulsed laser deposition (PLD), the primary work horse for complex oxide growth. Apart from the fact that PLD is a relative cheap option compared to MBE, it was long believed that PLD was a technique which would transfer a material preserving the stoichiometry. However, also PLD is a complex process where laser fluence and background pressure play an important role in the stoichiometry of the film. Here the ablation efficiency of the ions and the scattering processes between ions and the background gas play an important role[31]. In these scattering processes the particle mass is very important, changing the stoichiometry of the plume. All in all, having some knowledge of the stoichiometry during growth, also in deposition processes where the elements are not controlled separately as in MBE, would be quite advantageous. We shall come back to this issue in chapter 6.

References

[1] E. Dagotto, T. Hotta, and A. Moreo, *Colossal magnetoresistant materials: the key role of phase separation*, Physics Reports **344**, 1 (2001).

[2] A. Urushibara, Y. Moritomo, T. Arima, A. Asamitsu, G. Kido, and Y. Tokura, *Insulator-metal transition and giant magnetoresistance in* $La_{1-x}Sr_xMnO_3$, Physical Review B **51**, 14103 (1995).

[3] H. Fujishiro, M. Ikebe, and Y. Konno, *Phase Transition to Antiferromagnetic State in $La_{1-X}Sr_XMnO_3$ (X0.5)*, Journal of the Physical Society of Japan **67**, 1799 (1998).

[4] M. P. M. Dean, G. Dellea, R. S. Springell, F. Yakhou-Harris, K. Kummer, N. B. Brookes, X. Liu, Y.-J. Sun, J. Strle, T. Schmitt, L. Braicovich, G. Ghiringhelli, I. Boovi, and J. P. Hill, *Persistence of magnetic excitations in $La_{2x}Sr_xCuO_4$ from the undoped insulator to the heavily overdoped non-superconducting metal*, Nature Materials **12**, 1019 (2013).

[5] H. Weakliem, W. Burke, and V. Korsun, *Optical Properties of $SrTiO_3$ and $LiNbO_3$*, R.C.A. Review **36**, 149 (1975).

[6] S.-G. Lim, S. Kriventsov, T. N. Jackson, J. H. Haeni, D. G. Schlom, A. M. Balbashov, R. Uecker, P. Reiche, J. L. Freeouf, and G. Lucovsky, *Dielectric functions and optical bandgaps of high-K dielectrics for metal-oxide-semiconductor field-effect transistors by far ultraviolet spectroscopic ellipsometry*, Journal of Applied Physics **91**, 4500 (2002).

[7] J. G. Bednorz and H. J. Scheel, *Flame-fusion growth of $SrTiO_3$*, Journal of Crystal Growth **41**, 5 (1977).

[8] S. Geller and V. B. Bala, *Crystallographic studies of perovskite-like compounds. II. Rare earth alluminates*, Acta Crystallographica **9**, 1019 (1956).

[9] M. Kawasaki, K. Takahashi, T. Maeda, R. Tsuchiya, M. Shinohara, O. Ishiyama, T. Yonezawa, M. Yoshimoto, and H. Koinuma, *Atomic Control of the $SrTiO_3$ Crystal Surface*, Science **266**, 1540 (1994).

[10] G. Koster, B. L. Kropman, G. J. H. M. Rijnders, D. H. A. Blank, and H. Rogalla, *Quasi-ideal strontium titanate crystal surfaces through formation of strontium hydroxide*, Applied Physics Letters **73**, 2920 (1998).

[11] J. Mannhart and D. G. Schlom, *Oxide Interfaces–An Opportunity for Electronics*, Science **327**, 1607 (2010).

[12] M. Breitschaft, V. Tinkl, N. Pavlenko, S. Paetel, C. Richter, J. R. Kirtley, Y. C. Liao, G. Hammerl, V. Eyert, T. Kopp, and J. Mannhart, *Two-dimensional electron liquid state at $LaAlO_3$-$SrTiO_3$ interfaces*, Physical Review B **81**, 153414 (2010).

[13] A. Ohtomo and H. Y. Hwang, *A high-mobility electron gas at the* $LaAlO_3/SrTiO_3$ *heterointerface*, Nature **427**, 423 (2004).

[14] N. Nakagawa, H. Y. Hwang, and D. A. Muller, *Why some interfaces cannot be sharp*, Nature Materials **5**, 204 (2006).

[15] S. Thiel, G. Hammerl, A. Schmehl, C. W. Schneider, and J. Mannhart, *Tunable Quasi-Two-Dimensional Electron Gases in Oxide Heterostructures*, Science **313**, 1942 (2006).

[16] L. Zhang, X.-F. Zhou, H.-T. Wang, J.-J. Xu, J. Li, E. G. Wang, and S.-H. Wei, *Origin of insulating behavior of the p-type* $LaAlO_3/SrTiO_3$ *interface: Polarization-induced asymmetric distribution of oxygen vacancies*, Physical Review B **82**, 125412 (2010).

[17] Y. Segal, J. H. Ngai, J. W. Reiner, F. J. Walker, and C. H. Ahn, *X-ray photoemission studies of the metal-insulator transition in* $LaAlO_3/SrTiO_3$ *structures grown by molecular beam epitaxy*, Physical Review B **80**, 241107 (2009).

[18] M. Takizawa, S. Tsuda, T. Susaki, H. Y. Hwang, and A. Fujimori, *Electronic charges and electric potential at* $LaAlO_3/SrTiO_3$ *interfaces studied by core-level photoemission spectroscopy*, Physical Review B **84**, 245124 (2011).

[19] A. Brinkman, M. Huijben, M. van Zalk, J. Huijben, U. Zeitler, J. C. Maan, W. G. van der Wiel, G. Rijnders, D. H. A. Blank, and H. Hilgenkamp, *Magnetic effects at the interface between non-magnetic oxides*, Nature Materials **6**, 493 (2007).

[20] N. Reyren, S. Thiel, A. D. Caviglia, L. F. Kourkoutis, G. Hammerl, C. Richter, C. W. Schneider, T. Kopp, A.-S. Ruetschi, D. Jaccard, M. Gabay, D. A. Muller, J.-M. Triscone, and J. Mannhart, *Superconducting Interfaces Between Insulating Oxides*, Science **317**, 1196 (2007).

[21] A. Joshua, S. Pecker, J. Ruhman, E. Altman, and S. Ilani, *A universal critical density underlying the physics of electrons at the* $LaAlO_3/SrTiO_3$ *interface*, Nature Communications **3**, 1129 (2012).

[22] A. D. Caviglia, S. Gariglio, N. Reyren, D. Jaccard, T. Schneider, M. Gabay, S. Thiel, G. Hammerl, J. Mannhart, and J.-M. Triscone, *Electric field control of the* $LaAlO_3/SrTiO_3$ *interface ground state*, Nature **456**, 624 (2008).

[23] Ariando, X. Wang, G. Baskaran, Z. Q. Liu, J. Huijben, J. B. Yi, A. Annadi, A. R. Barman, A. Rusydi, S. Dhar, Y. P. Feng, J. Ding, H. Hilgenkamp, and T. Venkatesan, *Electronic phase separation at the* $LaAlO_3/SrTiO_3$ *interface*, Nature Communications **2**, 188 (2011).

[24] D. A. Dikin, M. Mehta, C. W. Bark, C. M. Folkman, C. B. Eom, and V. Chandrasekhar, *Coexistence of Superconductivity and Ferromagnetism in Two Dimensions*, Physical Review Letters **107**, 056802 (2011).

[25] J. A. Bert, B. Kalisky, C. Bell, M. Kim, Y. Hikita, H. Y. Hwang, and K. A. Moler, *Direct imaging of the coexistence of ferromagnetism and superconductivity at the* $LaAlO_3/SrTiO_3$ *interface*, Nature Physics **7**, 767 (2011).

[26] I. M. Dildar, D. B. Boltje, M. H. S. Hesselberth, J. Aarts, Q. Xu, H. W. Zandbergen, and S. Harkema, *Non-conducting interfaces of* $LaAlO_3/SrTiO_3$ *produced in sputter deposition: The role of stoichiometry*, Applied Physics Letters **102**, 121601 (2013).

[27] M. P. Warusawithana, C. Richter, J. A. Mundy, P. Roy, J. Ludwig, S. Paetel, T. Heeg, A. A. Pawlicki, L. F. Kourkoutis, M. Zheng, M. Lee, B. Mulcahy, W. Zander, Y. Zhu, J. Schubert, J. N. Eckstein, D. A. Muller, C. S. Hellberg, J. Mannhart, and D. G. Schlom, $LaAlO_3$ *stoichiometry is key to electron liquid formation at* $LaAlO_3/SrTiO_3$ *interfaces*, Nature Communications **4** (2013).

[28] H. K. Sato, C. Bell, Y. Hikita, and H. Y. Hwang, *Stoichiometry control of the electronic properties of the* $LaAlO_3/SrTiO_3$ *heterointerface*, Applied Physics Letters **102**, 251602 (2013).

[29] E. Breckenfeld, R. Wilson, J. Karthik, A. R. Damodaran, D. G. Cahill, and L. W. Martin, *Effect of Growth Induced (Non)Stoichiometry on the Structure, Dielectric Response, and Thermal Conductivity of* $SrTiO_3$ *Thin Films*, Chemistry of Materials **24**, 331 (2012).

[30] E. Breckenfeld, N. Bronn, J. Karthik, A. R. Damodaran, S. Lee, N. Mason, and L. W. Martin, *Effect of Growth Induced (Non)Stoichiometry on Interfacial Conductance in* $LaAlO_3/SrTiO_3$, Physical Review Letters **110**, 196804 (2013).

[31] S. Wicklein, A. Sambri, S. Amoruso, X. Wang, R. Bruzzese, A. Koehl, and R. Dittmann, *Pulsed laser ablation of complex oxides: The role of congruent ablation and preferential scattering for the film stoichiometry*, Applied Physics Letters **101**, 131601 (2012).

3

Low-Energy Electron Microscopy (LEEM)

Low-energy electron microscopy (LEEM) is a powerful surface science technique. It allows for real-time, in-situ imaging at elevated temperatures up to 1500 °C *with nanometer resolution. The surface sensitivity and large temperature window make it an ideal technique to study the formation of oxide surfaces and interfaces. In the following, I give a short introduction to LEEM and in more detail to our LEEM system called ESCHER. Furthermore, I will discuss the imaging techniques used to study the oxide interfaces.*

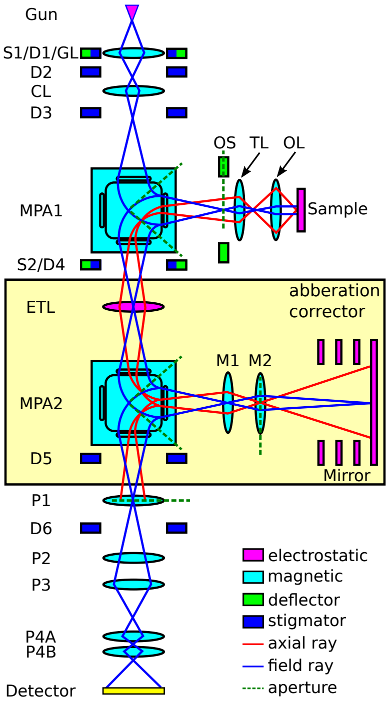

FIGURE 3.1: Schematic view of the electron-optical system of a LEEM. The yellow part is only included in the aberration corrected version. All electron-optical elements like lenses, deflectors and stigmators are labeled, and explained in the text.

3.1 Introduction to LEEM

Low-energy electron microscopy uses electrons up to 100 eV to perform surface sensitive imaging and spectroscopy. These low-energy electrons are very surface sensitive due to their low inelastic mean free path, which limits their penetration depth and is in the order of a few atomic layers[1].

Unlike scanning electron microscopes (SEM), LEEM illuminates the entire field of view at once. This allows for real-time imaging of dynamic processes. Two important components of a LEEM, are the magnetic prism array (MPA) and cathode objective lens. The MPA allows for transfer of the full field of view to the detector by separating the incoming, illuminating electrons from back-scattered electrons, used to form an image. The cathode lens is the crucial part for the low energy electrons as will be discussed later on. An illustration of the setup is shown in figure 3.1. First I will explain the non-aberration corrected version, in which the yellow part in figure 3.1 is absent.

Starting from the top, electrons leaving the electron gun are accelerated to an energy of 15 keV. These high energies are required for optimal performance of the electron lenses. The electrons are focused by the gun lens (GL) and condenser lens (CL) and can be steered by a set of deflectors (D1-D3) before entering the magnetic prism array (MPA1), which bends the electrons by 90 ° towards the sample. After passing the transfer lens (TL) the electrons arrive at the objective lens (OL). The objective lens consists of a magnetic lens and an electrostatic lens of which the sample forms the cathode. The sample is biased with a tunable negative high voltage close to the electron gun potential of 15 kV. The strong electric field ($\approx$ 10 kV/mm) decelerates the electrons to a selected energy in the range of 0 - 100 eV. An energy of 0 eV is called mirror mode, because the electrons just start to turn around before any interaction happened, and the sample becomes a mirror. After interaction with the sample, the electrons will be accelerated back to 15 keV in the same electric field. A diffraction pattern or in general the angular distribution of the electrons, is formed at the back focal plane of the objective lens and further along, a real-space image is formed at the image plane in the center of the magnetic prism array. To clarify the optical path, the field (blue) and axial (red) rays are drawn into figure 3.1. The axial or marginal ray starts at the point where the object crosses the optical axis and ends at the aperture stop. This ray crosses the optical axis at all points where an image is made. The field ray is parallel to the optical axis at the object and crosses the optical axis at the back focal plane.

Once the electrons are back at the prism array MPA1, it deflects the electrons downwards into the projector column. The projector column with lenses P1-4, magnifies and transfers the image onto the detector. Fast switching between imaging and diffraction mode is possible by turning on lens (P2) in the projector column. The lenses P4A-B can be used as a rotation free doublet for low magnifications or as a telescope for very strong magnification. The detector is build up out of a micro-channel plate, phosphor screen and camera. The channel plate amplifies the signal my multiplying the incoming electrons. The outgoing electrons are converted to photons with a phosphor screen, the photons are detected by a camera.

3.2 Aberration-corrected LEEM

The ESCHER (Electronic, Structural and CHEmical nanoimaging in Real-time) machine is the LEEM system located at Leiden University. It is based on the aberration corrected FE-LEEM P90 instrument (SPECS GmbH, Berlin) designed by Tromp[2,3]. The advantage of an aberration corrected LEEM is an increased spatial resolution up to 1.4 nm, a world record for LEEM, which was measured on this machine. The resolution of a LEEM machine is limited by the chromatic and spherical aberrations induced by the cathode objective lens OL. While these aberrations cannot be corrected by lenses since electron lenses can only be convex, the lowest order aberrations can be corrected by an electrostatic mirror[4]. The mirror is built up out of three high voltage rings, allowing for three degrees of freedom in the mirror shape. The voltages can be chosen such that the chromatic and spherical aberrations are opposite to the ones induced by the cathode lens while the mirror back plane stays in focus. The mirror is incorporated into the LEEM

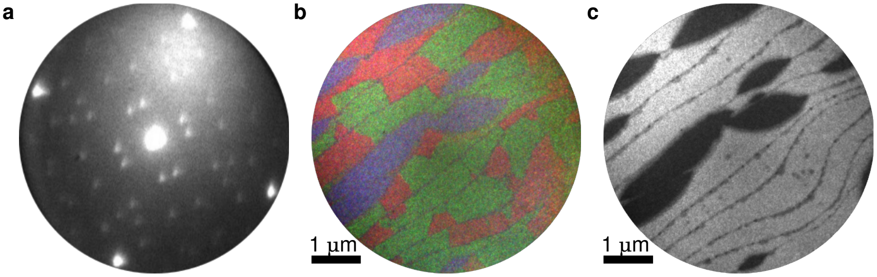

FIGURE 3.2: a) A LEED pattern of mixed terminated $SrTiO_3$ sample, taken at 14 eV. On the edge the four bright diffraction spots of the cubic perovskite unit cell can be seen while the spots around the center are from two rotations of the $\sqrt{13} \times \sqrt{13}$ R33.7 surface reconstruction. The spots of the 2×2 surface reconstruction are very vague. b) A multi darkfield image taken at 12 eV, red and green are the two rotations of the $\sqrt{13} \times \sqrt{13}$ R33.7 surface reconstruction while the blue area is 2×2 reconstructed. c) A bright field image taken at 12 eV of the same sample. The 2×2 reconstructed area is dark. Also the step edges are dark, due to destructive interference or phase contrast.

by introducing a second magnetic prism array (MPA2, Fig. 3.1). An electrostatic transfer lens (ETL) is placed between the two prisms to invert the image without rotations such that the dispersion of the two prisms cancel. An extra set of lenses (M1/M2) is placed between MPA2 and mirror to create a rotation-free defocused image on the mirror, optimizing the mirror performance.

3.3 Standard imaging techniques

A low energy electron microscope offers a unique opportunity in sample analysis by combining many measurement techniques. In the following sections I will briefly describe the main techniques used.

3.3.1 Low-energy electron diffraction (LEED)

The driving force behind many of the imaging techniques ina LEEM is the opportunity to combine real-space imaging with diffraction experiments. For electrons, crystalline samples will act as a grating and a diffraction pattern in the far field is the result. This technique is called low-energy electron diffraction (LEED) An example is shown in figure 3.2a of a $SrTiO_3$ crystal annealed at 1200 °C in air for 12 hours. The annealing leads to a mixed terminated surface with areas of TiO_2 and SrO areas[5,6]. On the edge of the image, bright spots are seen in a square pattern, the square surface net of $SrTiO_3$. In the center the specular spot represents the electrons scattered back perpendicular to the surface. The other spots are a combination of a $\sqrt{13} \times \sqrt{13}$ R33.7 surface reconstruction, with different directions, and a 2×2 reconstruction. The $\sqrt{13} \times \sqrt{13}$ R33.7 surface reconstruction is known to exists on the TiO_2 terminated part[7]. The 2×2 reconstruction is likely to be caused by SrO termination[5,6].

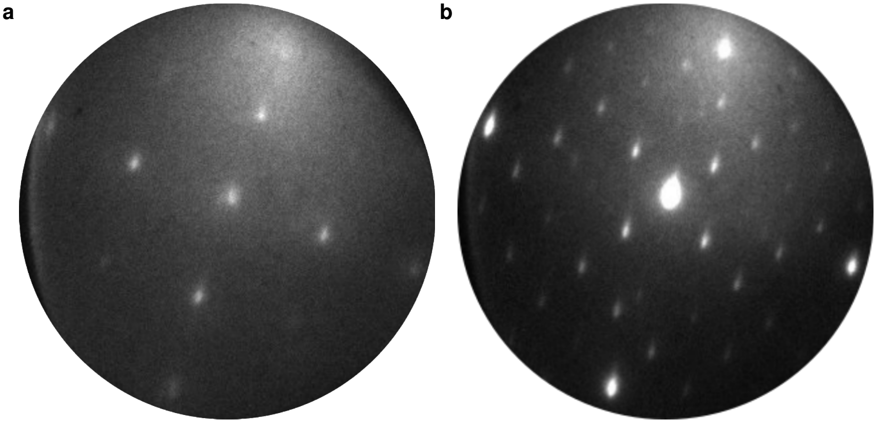

FIGURE 3.3: µLEED images of a mixed terminated $SrTiO_3$ sample. a) Taken at the 2×2 reconstructed part, blue in figure 3.2b. b) One of the two rotations of the $\sqrt{13} \times \sqrt{13}$ R33.7 reconstructed part. Both images are taken at 14 eV.

3.3.2 Bright field & dark field LEEM and µLEED

As stated earlier the strength of LEEM is combining real-space and diffraction information. By placing an aperture around one of the diffraction spots, the areas contributing to this spot can be imaged in real-space. An example is shown in figure 3.2b where three images are merged by adding them in red, green and blue. For every color in the image a diffraction spot of one of the three surface reconstructions is selected. The spots of the two rotations of the $\sqrt{13} \times \sqrt{13}$ R33.7 reconstruction are selected for red and green while a spot of the 2×2 reconstruction is selected for blue. In the results we can clearly see the diffraction patterns originate from distinct areas of the surface.

One can also select the center or specular diffraction spot. The real-space image now shows contributions of two effects. In the first place the intensity at a given energy is related to the (electronic) structure as will be described in more detail in section 3.4.4. This can be observed in figure 3.2c, where the intensity is different on the TiO_2 and SrO terminated areas. A second effect originates from the wave nature of the electrons. The electron waves can cause destructive interference at the step edges, for specific energies of the incoming electrons. This produces dark lines as shown in figure 3.2c and is called phase contrast.

Not only a part of the diffraction image can be selected, but also a part of a real-space image. The aperture now selects only a small region on the sample and the reconstruction on this region can be imaged. This is demonstrated in figure 3.3, where figure 3.3a is taken on a TiO_2 terminated area and figure 3.3b on a SrO terminated area of the $SrTiO_3$ sample. This technique is called micro-LEED (µLEED).

3.3.3 LEEM-IV

More quantitative data can be obtained from a diffraction pattern by not only collecting the position of the diffraction spots, but also the intensity dependence on the landing energy (or sample voltage) of the electrons. These are so called LEED-IV curves and can be used as a fingerprint or be compared with calculations of a model system. Compared to standard LEED the energies used in LEEM are even lower. This is sometimes called very low energy electron diffraction or VLEED. In this range multiple scattering is less important and for the specular diffraction spot, the data are close to the unoccupied band structure[8,9]. In LEEM this method can be extended with spatial resolution by selecting the specular diffraction spot with an aperture and image the real space IV-curve[10].

3.3.4 Photoemission electron microscopy (PEEM)

By turning off the electron beam and illuminating the sample with UV light the machine can be changed to a photoemission electron microscope (PEEM). Although this is an interesting technique in itself, in this thesis it is mainly used for alignment and as a localization technique. The spot of the electron beam is around 5 µm while the UV light illuminates the full sample so that images of a few hundred microns can be made.

3.4 Extending the possibilities

For the investigation of electronic and growth properties of perovskites like $SrTiO_3$ and $LaAlO_3$, a low-energy electron microscope is very suitable. It can perform real-time imaging while allowing for the high measurement temperatures required for the growth of these oxide materials. However, many other components still had to be added. In the following section I will explain more about the extensions we developed for the study of perovskite growth. First of all, the hardware: pulsed laser deposition (PLD), preparation chamber, heating laser (including laser safety). However, these days a complex measurement machine cannot be controlled without software and long and repeatable growth experiments cannot be achieved without automation. To achieve the automation a flexible software system has been developed.

Furthermore, the layer-by-layer growth of the perovskites studied in this thesis requires imaging techniques not commonly used in LEEM. Section 3.4.3 will introduce spot-profile analysis LEED (SPA-LEED). Improving the technique of angle-resolved reflection electron spectroscopy (ARRES) developed in our group allowed for repetitive probing of the electronic structure as will be explained in section 3.4.4.

3.4.1 Hardware

First of all, a pulsed laser deposition (PLD) system was added for the growth of perovskites. This PLD setup is described in chapter 5. Besides the PLD system the machine has also been equipped with a preparation chamber where in combination

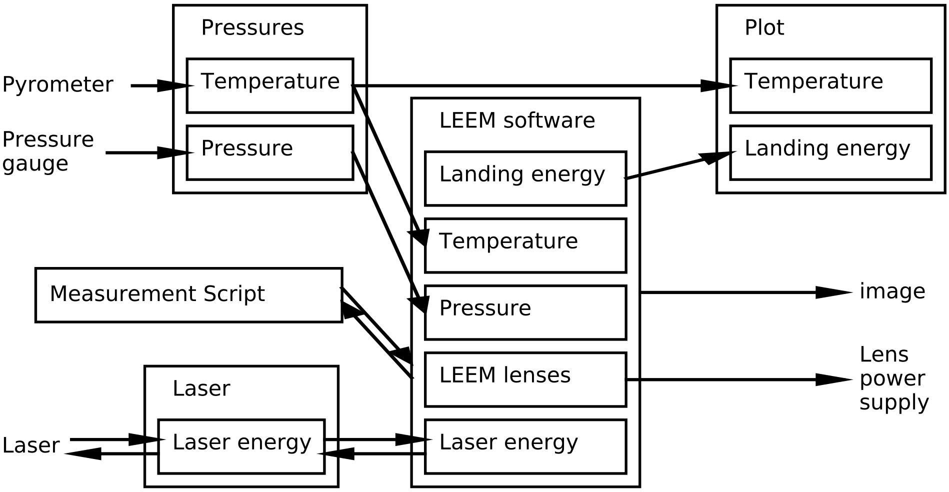

FIGURE 3.4: Example of data flow between software programs.

with a 100 W, 808 nm diode laser, the perovskite samples can be annealed in high oxygen pressures. This laser heater can also be attached to the main sample chamber to serve as an alternative for the electron bombardment heater. I developed a flexible interlock system enabling the heater to be used in combination with or next to the pulsed laser deposition system in both sample and preparation chamber while the machine is standing in an open experimental hall.

3.4.2 Software

Long repeatable growth processes require logging of growth parameters during the process as well as automatic control of the equipment. For this, new software has been developed. Figure 3.4 shows a flow diagram of the software programs and the data flows between them.

The existing LEEM software consists of a database containing all the electron lens values. These values can be controlled from the software as well as via a network transparent protocol. The program has been changed to extend the communication protocol and to save the database to the header of every image in order to have a complete description of the 'machine state' at the time the image was taken. Furthermore, the database can be extended with new variables via the communication protocol.

In order to flexibly add new hardware, a python program has been written, accommodating a parallel database containing the state of equipment around the machine. This program uses the network interface to communicate with the main LEEM program in order to exchange necessary data. The image acquisition time of the order of 100 to 250 ms only requires to push the data a few times a second. The advantage of this parallel database is flexibility for extension without loss of stability or the need to restart the LEEM control software. Figure 3.4 shows a program 'pressures' which reads the pressure gauge and temperature and pushes it to LEEM software. The program writes to a log file to support plotting of temperature and pressure independent of imaging.

On the fly hardware changes are required when changing from standard LEEM to pulsed laser deposition (chapter 5) or other new developments like potentiometry[11] or eV-TEM[12]. For the hardware control the communication protocol is extended with a callback function. When the callback function is enabled, the LEEM software sends a signal to the python program when the variable is changed. The python software can then communicate the change to the hardware. Figure 3.4 also shows a 'Laser control' program communicating back and forth to the hardware, and the LEEM software.

Once the basic protocols are in place, extra features can be added like a plotting script which can now communicate to our python server as well as directly to the LEEM software to plot for example the electron landing energy or sample temperature.

Measurement automation scripts can use the same protocol to communicate to LEEM software. For this purpose the communication protocol has been further extended. In the first place one would like to stop and test scripts without the risk of ending up in an unwanted machine state, where possibly the alignment of the microscope is lost. To accommodate this, variables have to be locked when a script it started. When a variable is locked, the value is stored and when the connection to the measurement script is lost, the value is restored to its original state. Moreover, collision between scripts is avoided by allowing only one script to change a variable.

3.4.3 Spot-profile-analysis LEED (SPA-LEED)

Measurement automation allows for new measurement techniques. One of these techniques is spot-profile-analysis low-energy electron diffraction (SPA-LEED). In SPA-LEED we use the fact that the diffraction pattern yields more information than only the intensity and position of the diffraction spots, which results in crystal structure information. By analyzing the shape of the diffraction spots we can learn about the surface roughness. This is an important analysis for layer-by-layer growth, where the surface roughens when a layer starts to grow and flattens when a full layer has been grown.

An example is shown in figure 3.5 for the specular diffraction spot. Here figure 3.5a shows the intensity versus energy (LEED-IV-curve) and figure 3.5b shows two example spot profiles at 40 eV (red) and 75 eV (green, dashed). This SPA-LEED technique is not so commonly used in combination with LEEM. An important reason is the change in intensity of the reflected electrons in the order of 10^4 when scanning the energy as can be seen in figure 3.5a. This large range of intensities make it impossible to resolve the spot shape over the full range, with a camera of only 12-bit image depth.

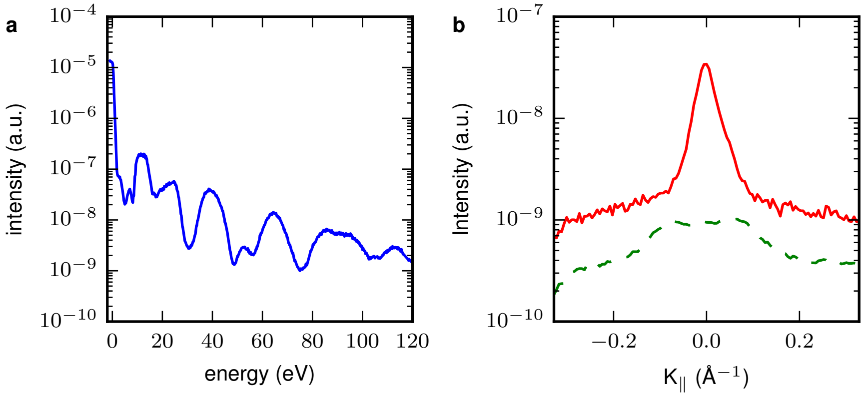

FIGURE 3.5: a) Maximum specular spot intensity versus energy for 1/2 unit cell homo-epitaxial $SrTiO_3$. b) Spot profile for the same sample at 40 eV (red) and 75 eV (green, dashed). $K_{||}$ is the in-plane wave vector of the electrons forming the diffraction spot.

To gain enough image depth for the images shown in figure 3.5, a method was developed to automatically adjust the gain of our imaging system, keeping the maximum intensity on the camera around 75% of its maximum. As described before, the imaging system here is a microchannel plate detector which multiplies the incoming electrons. The outgoing electrons are converted to photons with a phosphor screen, the photons are finally detected by the camera. The gain of the channel plates can easily be adopted by changing the amplification voltage. We characterized this gain to follow $I = (I_{cmr} - b)e^{-GV_{cp}}$, where I_{cmr} is the intensity measured by the camera, b the background signal originating from the camera readout noise, V_{cp} is the voltage over the channel plates in kV, G is the gain and I is the final intensity. Here the gain was measured to be 20 kV^{-1}. In practice the channel plate voltage V_{cp} lies between 0.9 kV and 1.7 kV resulting in a six orders of magnitude amplification range.

For a so-called high-dynamic range energy scan, automatic adjustment of the gain is implemented in the energy scan script by calculating the gain required for 75% saturation of the camera after each image. This gain is used to capture the next frame. Expecting a smooth and slowly changing brightness, the intensity of the next image will thus lie within range of the camera.

For real-time growth analysis the high-dynamic range scans are automatically analyzed and time versus full-width-half-max (FWHM) of the specular diffraction spot is plotted to analyze the growth.

3.4.4 Angle-resolved reflection electron spectroscopy (ARRES)

Parallel to my work Johannes Jobst and Jaap Kautz developed a technique to probe the unoccupied band structure of graphene[9] in our LEEM setup. In this technique the intensity of the specular spot is measured as function of the energy and in-plane momentum of the electrons. In first order the signal depends on the availability of a state in the material with the same energy and in-plane momentum $k_{\|}$ as the electron. If this state is available the electron will couple into the material, otherwise it will reflect.

This measurement can be done in diffraction, where one averages the signal over a 5 micron spot, as well as in real-space where an aperture is used around the specular spot and full spatial resolution can be obtained. I improved this technique and made it easy to use for quick and repetitive measurements by adding high dynamic range as well as full automation of the measurement. For automation of real-space ARRES it is important to not only change the parallel momentum $k_{\|}$ of the electron by changing deflector D1 (Fig. 3.1), but also to keep the imaged area constant by correcting any beam shift by D3. Furthermore, the aperture in the diffraction plane has to be moved due to the displacement of the specular spot in the diffraction plane when $k_{\|}$ is changed.

References

[1] S. Tanuma, C. J. Powell, and D. R. Penn, *Calculations of electron inelastic mean free paths. V. Data for 14 organic compounds over the 502000 eV range*, Surface and Interface Analysis **21**, 165 (1994).

[2] R. Tromp, J. Hannon, A. Ellis, W. Wan, A. Berghaus, and O. Schaff, *A new aberration-corrected, energy-filtered LEEM/PEEM instrument. I. Principles and design*, Ultramicroscopy **110**, 852 (2010).

[3] R. Tromp, J. Hannon, W. Wan, A. Berghaus, and O. Schaff, *A new aberration-corrected, energy-filtered LEEM/PEEM instrument II. Operation and results*, Ultramicroscopy (2013).

[4] S. M. Schramm, J. Kautz, A. Berghaus, O. Schaff, R. M. Tromp, and S. J. van der Molen, *Low-energy electron microscopy and spectroscopy with ESCHER: Status and prospects*, IBM Journal of Research and Development **55**, 1:1 (2011).

[5] R. Bachelet, F. Snchez, F. J. Palomares, C. Ocal, and J. Fontcuberta, *Atomically flat SrO-terminated SrTiO3(001) substrate*, Applied Physics Letters **95**, 141915 (2009).

[6] R. Bachelet, F. Snchez, J. Santiso, C. Munuera, C. Ocal, and J. Fontcuberta, *Self-Assembly of SrTiO3(001) Chemical-Terminations: A Route for Oxide-Nanostructure Fabrication by Selective Growth*, Chemistry of Materials **21**, 2494 (2009).

[7] D. M. Kienzle, A. E. Becerra-Toledo, and L. D. Marks, *Vacant-Site Octahedral Tilings on* $\mathrm{SrTiO_3}$ *(001), the* $(\sqrt{13} \times \sqrt{13})R33.7^\circ$ *Surface, and Related Structures*, Physical Review Letters **106**, 176102 (2011).

[8] V. N. Strocov, H. I. Starnberg, P. O. Nilsson, H. E. Brauer, and L. J. Holleboom, *New Method for Absolute Band Structure Determination by Combining Photoemission with Very-Low-Energy Electron Diffraction: Application to Layered* $\mathrm{VSe_2}$, Physical Review Letters **79**, 467 (1997).

[9] J. Jobst, J. Kautz, D. Geelen, R. M. Tromp, and S. J. van der Molen, *Nanoscale measurements of unoccupied band dispersion in few-layer graphene*, Nature Communications **6**, 8926 (2015).

[10] J. B. Hannon, J. Sun, K. Pohl, and G. L. Kellogg, *Origins of Nanoscale Heterogeneity in Ultrathin Films*, Physical Review Letters **96**, 246103 (2006).

[11] J. Kautz, J. Jobst, C. Sorger, R. M. Tromp, H. B. Weber, and S. J. van der Molen, *Low-Energy Electron Potentiometry: Contactless Imaging of Charge Transport on the Nanoscale*, Scientific Reports **5** (2015).

[12] D. Geelen, A. Thete, O. Schaff, A. Kaiser, S. J. van der Molen, and R. Tromp, *eV-TEM: Transmission electron microscopy in a low energy cathode lens instrument*, Ultramicroscopy **159**, 482 (2015).

4

Formation of a mixed ordered termination on the surface of $LaAlO_3(001)$

We have investigated the surface termination of $LaAlO_3(001)$ at elevated temperatures by Low-Energy Electron Microscopy (LEEM). The terminating layer can be LaO or AlO_2. The LaO surface shows a $\sqrt{5} \times \sqrt{5}\,\mathrm{R}26$ reconstruction which can be used as a signature for the LaO termination, while the AlO_2 termination is unreconstructed. We find that heating of as-delivered substrates in vacuum, or heating substrates which were previously annealed in air or oxygen, can lead to a reconstructed surface as observed in diffraction. However, the real-space image shows that the reconstructed areas only cover about a third of the surface and that the termination is actually an ordered mixture of the reconstructed LaO and the unreconstructed AlO_2 terminations. This conclusion is supported by data from Atomic Force Microscopy. We also demonstrate how the disordered mixture of both terminations changes to large LaO islands in the middle of the AlO_2 terraces upon heating.

This chapter has been published as:

A.J.H. van der Torren, S.J. van der Molen, J. Aarts
Formation of a mixed ordered termination on the $LaAlO_3$ surface
Phys. Rev. B. **91**, 245426 (2015)

4.1 Introduction

Much effort is currently directed to investigating the properties of interfaces between perovskite oxides, in particular those of the ABO_3 type, with particular emphasis on the two-dimensional electron gas (2-DEG) which is formed between the insulators $SrTiO_3$ (STO) and $LaAlO_3$ (LAO)[1]. Of prime importance here is control over and knowledge of the atomic termination layer of the surface on which the interface is prepared. For instance, in order to form the 2-DEG, it is well known that the STO surface has to be terminated with a TiO_2 layer. Recipes exist for the fabrication of different termination layers on the various substrates which are used in oxide research. Of recent interest are endeavors to fabricate mixed ordered terminations, which allow for the possibility to perform selective area growth.

In this study we focus on the surface of $LaAlO_3(001)$, which can be A-site terminated with a layer of LaO or B-site terminated with a layer of AlO_2. In the literature, contradictory reports can be found on the issue of fabricating singly terminated surfaces. Kim *et al.*[2] use an 1100 °C annealing step in oxygen and find a predominantly AlO_2 termination, while Gunnarsson *et al.*[3] come to the conclusion that the surface is doubly terminated when only annealed in oxygen. They report that etching the surface with HCl, followed by annealing in oxygen at the relatively low temperature of 800 °C leads to AlO_2 termination[3]. Early work suggested that also a complete A-site termination can be obtained even at 250 °C[4,5], but this finding could not be reproduced[6]. An LaO terminated surface was reported after annealing at 700 °C in UHV using He atom scattering[7], while similar annealing was found to yield an AlO_2 surface with 10 nm LaO islands[8].
Extensive surface x-ray measurements were performed by Lanier *et al.* on surfaces which were prepared by annealing an $LaAlO_3$ substrate between 1100 °C and 1500 °C in air[9]. Such surfaces show a clear $\sqrt{5} \times \sqrt{5}\,\mathrm{R}26$ (RT5) reconstruction, and it was concluded that it is the LaO layer which reconstructs, yielding a surface with one La vacancy per surface unit cell and stoichiometry (VLa_4O_5) (with V the vacancy). We are not aware of a study of the occurrence of reconstructions on the AlO_2-terminated surface, and as a working hypothesis we assume that it does not reconstruct.
Here we use Low-Energy Electron Microscopy (LEEM) to study the behavior of the $LaAlO_3$ surface at high temperatures, an issue which is both relevant for surface preparation and for growth. With the LEEM technique, we are able to discern different terminations in two ways. One is through the diffraction pattern when different reconstructions occur on the two terminations. By using apertures in the outgoing beams, LEEM also allows us to make a real space image of the occurrence of different reconstructions with high lateral resolution. The other way is to measure the intensity of the diffraction spots (I), in particular of the specular beam, as function of the electron energy (V).
In this way we find for $LaAlO_3[001]$ that surfaces can be prepared with a single termination of AlO_2, but that high temperature treatments, presumably yielding a reconstructed LaO surface, actually lead to spatially separated areas with and

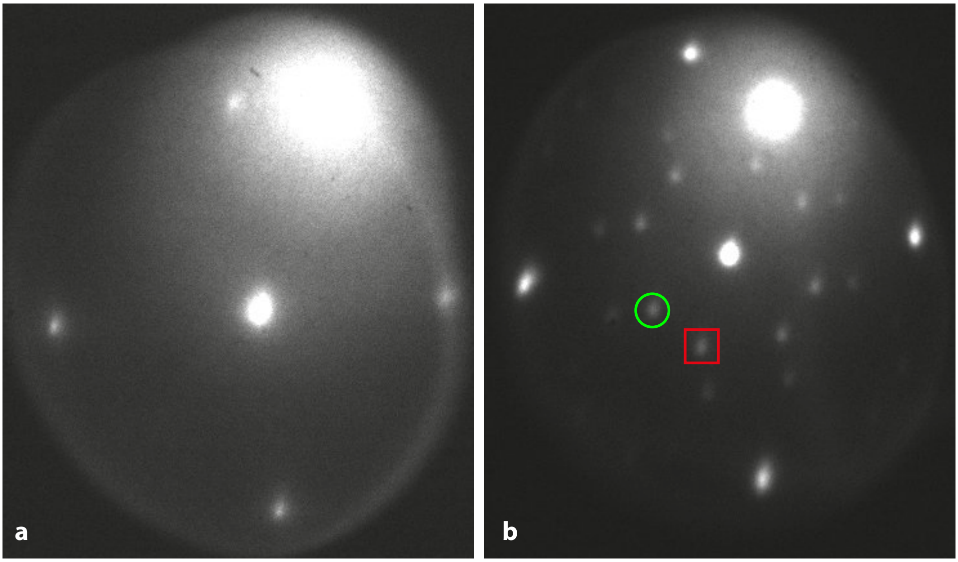

FIGURE 4.1: LEED pattern before a) and after b) annealing the sample at 1100 °C. The images were taken at 17 eV and at 875 °C and 910 °C respectively. In (b), the diffraction spots of the $\sqrt{5}\times\sqrt{5}$ R26 reconstruction are visible. Spots from two distinct domains are denoted with a green circle and a red square. The bright spot in the right top corner is due to secondary scattered electrons which are displaced from the center by dispersion in the system.

without reconstruction, and with different IV characteristics. Complementing the LEEM data with room temperature AFM, we conclude that the annealing process leads to a mixed but ordered termination of both LaO and AlO_2, with the LaO termination occurring predominantly in the middle of terraces on the otherwise atomically flat surface.

4.2 Experimental

The LEEM experiments were performed in the so-called "Escher" setup, a state-of-the-art aberration-corrected LEEM facility at Leiden University[10–13]. In the LEEM, electrons are accelerated from a cold field emission gun to an energy of 15 kV and deflected by a magnetic prism array over 90° towards the objective lens and the sample. Between the lens and the sample a decelerating field is applied, which is used to accurately tune the landing energy of the electrons on the sample in the range from 0 to 100 eV. The zero landing energy is influenced by the difference between sample and gun voltage supply, the work function of the gun filament and the work function of the sample. Determining the correct value for the zero of energy can in principle be done with an inaccuracy of less than 0.1 eV but in this work we did not put special attention to the optimization, leading to sample-to-sample variations of the order of 1 eV. At the sample the electrons are diffracted and accelerated again towards the objective lens. After passing the objective lens, they are deflected into the projection column and pass through a second magnetic prism deflecting the beam to an electrostatic mirror, a procedure which corrects for chromatic aberration[10]. Coming back from the mirror the electrons re-enter the projection column and form a real-space or reciprocal space image on the channelplate detector.

With this system, various imaging modes can be used. In the first place low energy electron diffraction (LEED) can be used to study the structure of the surface. Lateral variations in the structure can be imaged by placing an aperture in the diffraction plane around one of the diffraction spots. By changing the projector lenses to produce a real space image, we can then study which areas of the sample contribute to that diffraction condition. This is called dark-field imaging. For so called bright-field mode the aperture is placed around the zeroth order LEED spot. Here we can still have contrast between structures with different reflection intensities (given by the structure factor) at a given electron energy. By measuring the intensity of the diffracted beam as function of electron energy at the sample, the so-called IV-curve, a specific signature of the surface can be obtained[14–16]. Since the IV curve of a surface is determined by the precise positions of the atoms, contrast between reconstructed and non-reconstructed areas can also be found at certain energies in bright field mode. To determine which areas in bright field belong to which reconstruction, the dark-field images are used.

Experiments in the LEEM are performed in a vacuum of 10^{-9} mbar, and the sample can be continuously heated up to 1300 °C. Images are acquired with an acquisition time of 250 ms (four images per second) by a 1280x1024 pixel CCD camera behind a channel plate detector. Switching within less than a second between different magnifications and image modes results in fast real time imaging of changes in the surface morphology.

Atomic Force Microscopy was routinely used to characterize the surface topography. A special experiment was performed on two samples to compare the information of LEEM and AFM on the same area. For this, trenches were etched in the surface using electron beam lithography and Ar-ion etching. These trenches served as markers both in the light microscope attached to the AFM and in the photo-emission mode of the LEEM, both of which have a field of view of a few hundred micrometer.

Commercial substrates, polished on one side, were obtained from Crystal-GmbH in three different batches. For experiments where samples were annealed in air, the substrates were first loaded into a furnace and heated up to 1150 °C. After annealing they were loaded into the LEEM. Other samples were directly loaded into the LEEM and annealed in vacuum. The temperature in the LEEM was measured by a pyrometer assuming an emissivity of 0.9. During imaging, samples were kept at at least 400 °C to avoid charging of the insulating substrates.

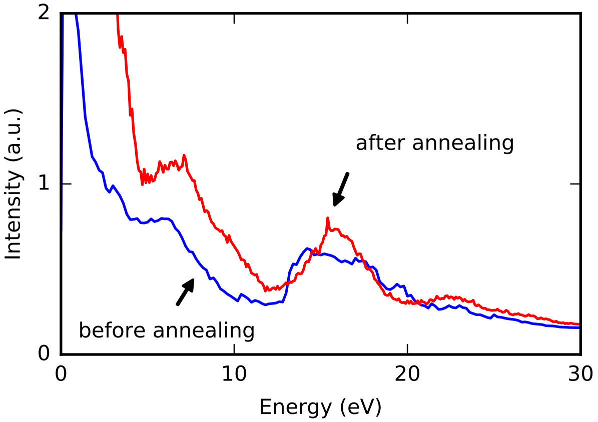

FIGURE 4.2: LEED-*IV* curves taken from the (0,0) spots of the LEED patterns shown in Fig. 4.1, before and after annealing the sample.

4.3 Results

An issue which surfaced in the research described here but which may well be more general, was that the as-received samples did not all behave in exactly the same manner. In the first set of experiments, a diffraction pattern pointing to a surface reconstruction could be directly obtained by annealing in vacuum at high temperatures, but several attempts to make an AlO_2-terminated surface by annealing in oxygen failed. With a different batch of substrates, this (B-site) termination could be prepared, but obtaining the (A-site) reconstructed surface was only possible for a part of the surface. This will be detailed below.

4.3.1 Reconstructed surfaces

In Fig. 4.1a we show the diffraction pattern of an as-received sample, taken at 875 °C, which shows an unreconstructed surface. The sample was then annealed in-situ for about 7 hours at a temperature of 1100 °C and cooled to 910 °C. This resulted in the diffraction pattern given in Fig. 4.1b. It has four extra spots deriving from a rotated square surface net indicative of the RT5 reconstruction. Moreover, as indicated in the figure, the extra spots are doubled due to the fact that there are two equivalent rotations of the reconstruction, and both types are formed as domains on the surface. Fig. 4.2 shows the *IV* curve of the (0,0) spot for the surface before and after annealing. They are quite similar, although the curve after annealing shows a more pronounced maximum at 18 V and an additional peak at 22 V.

With the two equivalent fractional order patterns in the LEED pattern, dark-field mode can be used to image the spatial extent of the two reconstructed domains

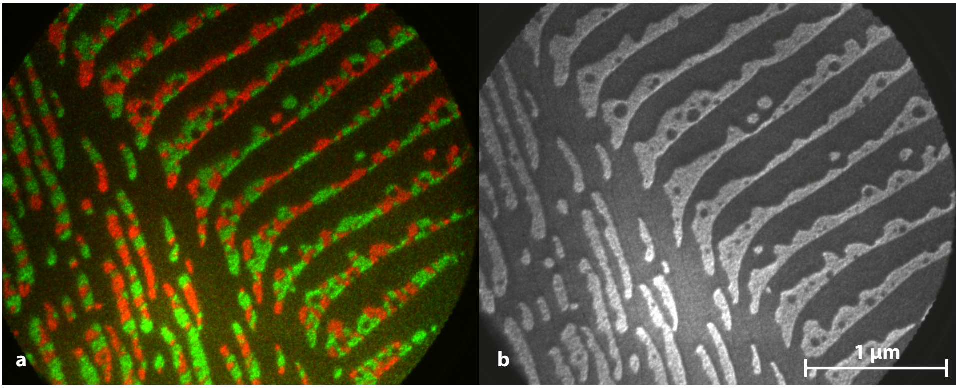

FIGURE 4.3: a) Multi dark field and b) bright field image of $LaAlO_3$ after annealing above 1070 °C. The images were taken at 15 eV and 17.6 respectively, at a temperature of 890 °C. The dark field image consists of the two images of the distinct RT5 domains, overlaid in green and red.

separately. This is shown in Fig. 4.3a, where the two RT5 domains are color-coded in red and green. Interestingly, the reconstruction does not fully cover the surface. Rather it forms in stripe-like patterns with a more or less random variation of the two rotations, covering no more than about a third of the surface. The larger fraction of the surface is therefore not reconstructed. The reconstruction can also be imaged in bright-field, by choosing the appropriate energy, as shown in Fig. 4.3b taken at 17.6 eV. The two types of rotation are now not distinguishable, but otherwise the image faithfully reproduces the areas where the reconstruction is present (bright) or absent (dark). By taking bright field images at different electron energies, it is also possible to generate *IV* curves at all positions on the surface. Fig. 4.4 shows such *IV* curves of the (0,0) beam, taken on either a reconstructed (bright) or unreconstructed (dark) area. They are quite different. The unreconstructed area shows peaks around 5 V, 9 V, 12 V and 18 V, plus a small maximum around 25 V. The one from a reconstructed area shows peaks around 10 V and 18 V and generally shows a higher intensity, which leads to the contrast seen in Fig. 4.3b taken at 17.6 V. Comparing these data to the *IV* curves in Fig. 4.2 emphasizes that *IV* curves taken on surfaces with a mix of reconstructed areas are of limited value. In particular the curve after annealing represents some weighted average of the two curves in Fig. 4.4 but cannot be used as the characteristic of either one of the surface terminations.

Although difficult to see in Fig. 4.3b there are also thin black lines visible in the bright-field image, which are related to and localized at step edges on the substrate. They can be seen to bend over roughly 90 ^{o} in the field of view, with the stripe-like domains following the direction of the steps. The relation between steps and domains was investigated further. For this we used a sample with Ar-ion etched markers as described in the previous section. Fig. 4.5a shows a bright-field image taken at 15.2 eV, an energy at which the step contrast is enhanced. Two steps are

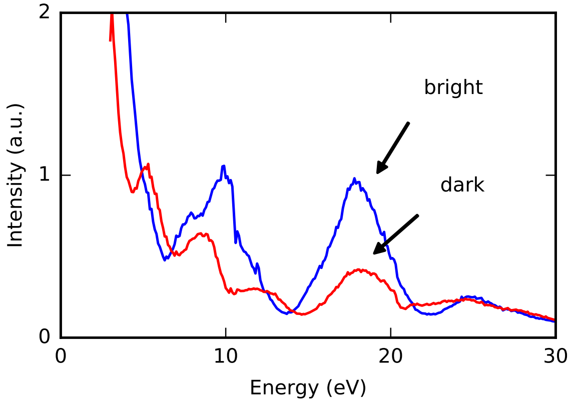

FIGURE 4.4: *IV* curves taken from a selected area of the zero-order beam and taken from the reconstructed (bright) and unreconstructed (dark) areas on the surface. A circle containing 1264 pixels (equivalent to a diameter of about 100 nm) within a bright field image is averaged for every energy. Figure 4.3b is one of the bright field images out of this energy series.

visible, indicated by red arrows, and it is seen that the reconstructed area lies in the middle of the terrace, which is defined by the two steps. Fig. 4.5b shows an AFM image made *on the same area*. The steps are sharp and clearly visible, but also the reconstructed area is visible in the AFM image, which therefore appears to be of different height. The cross-section from the AFM image, given in Fig. 4.5d shows that the steps around the reconstruction are about 0.35 nm high, corresponding to a full LaAlO$_3$ unit cell. The steps bordering the reconstruction are smaller, only about 0.1 nm, and the reconstructed areas lie deeper than the terrace on which they reside. The smaller steps can also be observed in the bright field image at the appropriate energy. Fig. 4.5c shows an image taken at 26.8 eV. This energy is chosen such that there is no contrast from the reconstruction, but there is (phase) contrast to observe the steps. The middle red arrow shows the right-hand step in the earlier image, but four extra steps appear (outer blue arrows) which border the reconstructed areas.

Most experiments in literature reporting the occurrence of the RT5 reconstruction and/or a mixed termination were performed by extensive annealing of the LaAlO$_3$ sample in air or oxygen rather than in UHV as described above. We therefore performed annealing experiments in air on samples from the third batch. One sample was annealed for ten hours in a tube furnace at 1150 °C. Figure 4.6a shows the resulting LEEM and AFM images, which are very comparable with the UHV annealed samples. The atomically flat patches in the AFM image are now somewhat larger, which makes determination of the height variations easier. As before, it is seen that the reconstructed area lies deeper than the surrounding terrace, but the strips now tend to lie closer to the steps rather than in the middles terrace. The

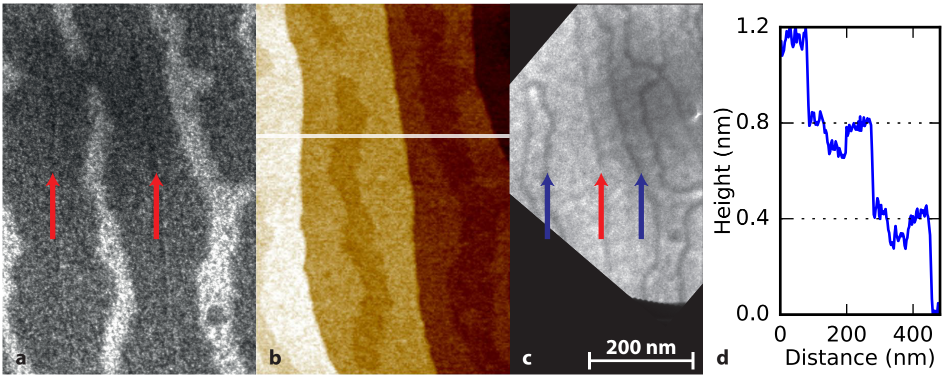

FIGURE 4.5: a) Bright field image of $LaAlO_3$ at 15.2 eV. Dark lines, indicated by red arrows, are unit cell steps between substrate terraces. The bright area is the $\sqrt{5} \times \sqrt{5}\,$R26 reconstructed area. b) AFM image of same area. The thin white bar indicates the position of the cross section shown in d). This cross section is averaged over 7 lines in the image. c) Bright field image taken at 26.8 eV. The red arrow again indicates the step between the terraces while the blue arrows indicate the step between the terrace and the reconstruction. d) Height profile of the area given by the white line in b).

steps between the reconstructed and unreconstructed areas are clearly of half-unit cell height. This was less clear in Fig. 4.5 which could be caused by incomplete LaO termination. Looking closely at Fig. 4.5a again reveals numerous small dark spots within the bright area. Possibly the LaO termination is not fully developed and small AlO_2 islands still remain. Averaging such AlO_2 areas with the LaO areas might result in an AFM height profile with less than half-unit cell steps.

4.3.2 The singly terminated surface

To further understand the difference between the reconstructed and unreconstructed areas we prepared a sample with a single terminated surface. As described in the introduction, how to prepare a single AlO_2 termination is not completely obvious. Samples from two batches were annealed in various ways, in oxygen at atmospheric pressure as well as in air and vacuum. Some where etched in HCl as reported in Ref. 3, others where directly annealed as reported by Ref. 17. None of them led to the desired unit-cell-step and terrace structure as reported e.g. in Ref. 3, 17. In a third batch, we succeeded using a two step process. The sample was first annealed at 800 °C in UHV, followed by exposure to air after cooling down to room temperature. A subsequent anneal at 1000 °C in UHV resulted in an unreconstructed surface (not shown). An AFM image of this surface is presented in Fig. 4.7a. Single steps with a height of 0.4 nm are visible, and equally important, no half-size steps were found in Fig. 4.5d, suggesting the surface is singly terminated, and presumably by AlO_2. A LEED-IV curve taken on this surface is shown in Fig. 4.8. Comparison of this IV curve with the one given in Fig. 4.4 of a dark (unreconstructed) area

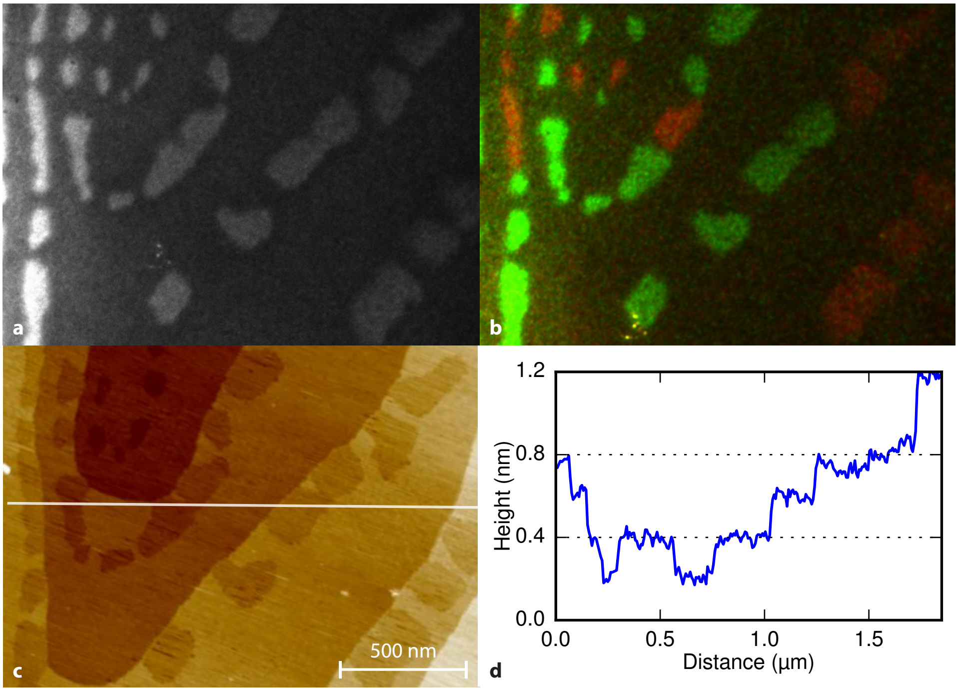

FIGURE 4.6: a) Bright field image at 9.2 eV and b) dark field images at 14 eV of an $LaAlO_3$ sample annealed in air; c) AFM image of the same area. According to the AFM image, the reconstructed areas clearly lie lower than the surrounding terraces. d) Height profile along the cross-section drawn in c). Both half-unit cell steps and full-unit cell steps are present. The half-unit cell steps correspond with the reconstructed areas while the full-unit cell steps are between two unreconstructed terraces.

on the reconstructed sample shows them to be virtually identical. From this we conclude that also the unreconstructed part of such surface is AlO_2 terminated.

4.3.3 On the formation of the mixed ordered termination

Being able to prepare and image the partial RT5 reconstruction and LaO termination by UHV annealing as discussed in Section 4.3.1 offers a unique opportunity to follow the process which leads to the mixed ordered termination. The first signs of the RT5 LEED pattern appear at a temperature of 930 °C, the lowest temperature where we can probe the mixed ordered termination. Figure 4.9 shows four bright-field images during the annealing process, taken at 935 °C, 1090 °C, 1155 °C and 1170 °C at an energy around 16.5 V. The first image shows a grainy structure which starts to form small stripes and spots in the second image. When increasing the temperature, the small spots form larger continuous areas. In the last image the small dots have mostly disappeared and the bright areas form wide

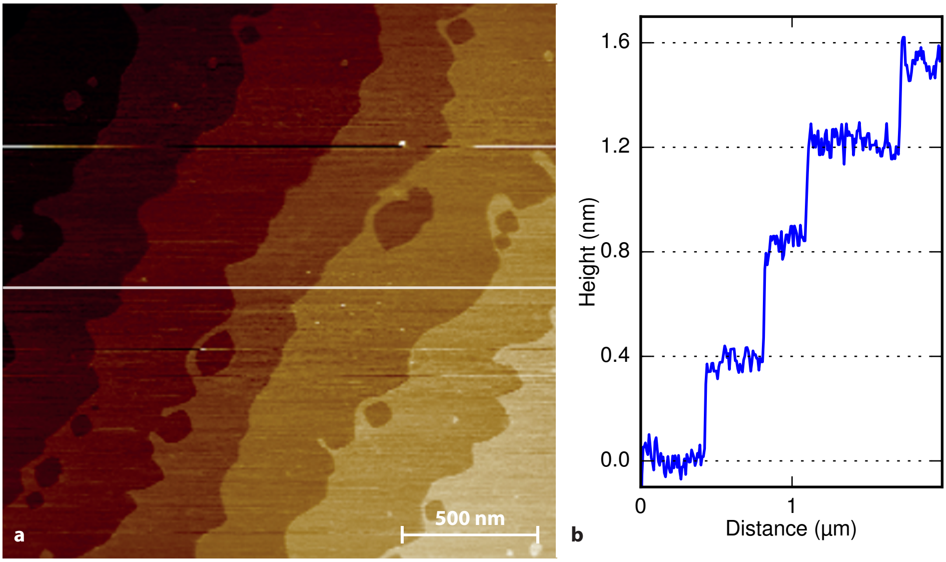

FIGURE 4.7: a) AFM image of a singly AlO_2 terminated sample; b) height profile taken along the line drawn in a). Only full unit cell steps can be seen, confirming that the sample is singly terminated.

and continuous stripes. Looking back at the first image, it suggests that there the reconstructed areas are very small, leading to relatively little coherent scattering. Repeating the experiment with different time scales we find no real differences. Going to 1200 °C in a few seconds or in an hour does not change the result. Also keeping the sample close to 1200 °C for seven hours did not change the morphology which formed initially.

4.4 Discussion

Taking the data together, the first point to remark is that we found variety in the way that samples from different batches behaved. Nevertheless, several clear conclusions can be drawn. A singly terminated AlO_2 surface can be prepared, although the procedure may vary. Without being complete, in the literature, a high temperature (1000 °C) anneal in flowing oxygen was used[2]; or a somewhat lower (800 °C) flowing oxygen anneal preceded by a cleaning step in HCl[3]; or a 900 °C anneal at very low oxygen pressure (10^{-6} mbar)[17]. This already shows that the recipe is not unique. We did not find single termination by these methods, but succeeded through a two-step process, an 800 °C anneal in UHV, followed by exposure to air and a 1000 °C anneal in UHV. This suggests that the process for preparing single termination depends on the history of the sample, possibly even including the polishing process. A successful procedure leads, in our case, to an atomically flat surface with only unit-cell steps of 0.4 nm height. This AlO_2-terminated sur-

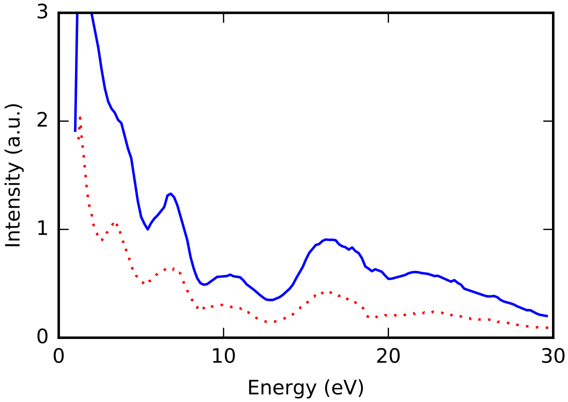

FIGURE 4.8: LEED-*IV* of the single terminated sample shown in Fig.4.7 (blue line). The *IV* curve of the unreconstructed area shown in Fig. 4.4 is shown for comparison (red dots). This curve was shifted by 2 eV since the zero of energy was not determined accurately.

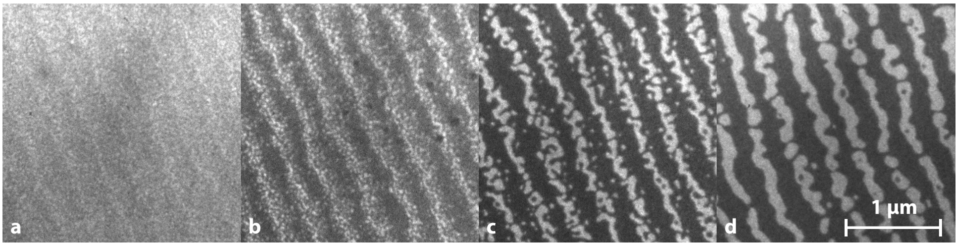

FIGURE 4.9: Bright field images of a $LaAlO_3$ surface. The images are taken during annealing at 935, 1090, 1155 and 1170 °C respectively. The landing energy of the electrons is around 16.5 eV.

face is unreconstructed and has a well-defined and unique LEED-*IV* signature. Using the occurrence of the RT5 reconstruction as a signature for LaO termination we come to the conclusion that a singly terminated LaO surface cannot be prepared. Preparing a reconstructed surface either by annealing in UHV or in air, we find from imaging by LEEM (both in bright-field and in dark-field) that the reconstructed areas form in stripe-like domains. From the step contrast it is seen that the stripes tend to be found in the middle of terraces, and the reconstructed LaO stripes have a LEED-*IV* signature which is different from the AlO_2 surface. Moreover, the unreconstructed part of the terraces do show the AlO_2 signature. From the AFM data we find that the reconstructed areas lie *lower* than the surrounding terraces, with a height difference of about half a unit cell. Our results indicate that the reconstruction starts forming at 930 °C when the RT5 LEED spots become visible and small islands of reconstructed surface are seen to form. This is roughly consistent with the results of Schmidt *et al.*[8] who find a mixture of small

LaO islands and AlO_2 islands spread over the surface after annealing at 670 °C. The presence of small islands might also be the explanation of the presence of steps less than half a unit cell in Fig. 4.5. In Fig. 4.5a the bright area still has small black speckles, indicating the LaO islands are not fully grown together and small AlO_2 islands are present within the LaO area. These differences are not resolved by the AFM and are averaged in the picture, resulting in the small steps. Finally, we note the fact that the LaO-based areas lie deeper than the AlO_2 surface. This suggests a scenario in which the starting surface has a mixed termination with AlO_2 islands on top. Increasing the temperature mobilizes the islands which seek step edges to form closed AlO_2 layers not fully covering the surface. At the same time the lower lying exposed LaO areas lose lanthanum and form the RT5 reconstruction. A fully singly terminated AlO_2 surface, on the other hand, is stable even at high temperatures.

4.5 Summary

We investigated the surface of $LaAlO_3$[001] single crystals by Low-Energy Electron Microscopy and Atomic Force Microscopy. Annealing from 930 °C to 1150 °C in UHV as well as in air we found a mixed ordered surface termination of unreconstructed AlO_2 and reconstructed ($\sqrt{5} \times \sqrt{5}\,\mathrm{R}26$) LaO, with the fraction of reconstructed LaO being about one third. We could follow the formation of the mixed ordered termination with temperature from a mixture of small islands of either kind to stripes of LaO in the middle of terraces of AlO_2, with the stripes lying lower than the surrounding terraces. By preparing a surface with a single AlO_2 termination we also demonstrated the difference in IV characteristics for the unreconstructed AlO_2 termination and the reconstructed LaO termination.

References

[1] A. Ohtomo and H. Y. Hwang, *A high-mobility electron gas at the* $LaAlO_3/SrTiO_3$ *heterointerface*, Nature **427**, 423 (2004).

[2] D.-W. Kim, D.-H. Kim, B.-S. Kang, T. W. Noh, D. R. Lee, and K.-B. Lee, *Roles of the first atomic layers in growth of* $SrTiO_3$ *films on* $LaAlO_3$ *substrates*, Applied Physics Letters **74**, 2176 (1999).

[3] R. Gunnarsson, A. Kalabukhov, and D. Winkler, *Evaluation of recipes for obtaining single terminated perovskite oxide substrates*, Surface Science **603**, 151 (2009).

[4] J. Yao, P. B. Merrill, S. S. Perry, D. Marton, and J. W. Rabalais, *Thermal stimulation of the surface termination of* $LaAlO_3\{100\}$, The Journal of Chemical Physics **108**, 1645 (1998).

[5] P. van der Heide and J. Rabalais, *Photoelectron spectroscopic study of the temperature-dependent termination of the* $LaAlO_3$*(100) surface*, Chemical Physics Letters **297**, 350 (1998).

[6] R. J. Francis, S. C. Moss, and A. J. Jacobson, *X-ray truncation rod analysis of the reversible temperature-dependent [001] surface structure of* $LaAlO_3$, Physical Review B **64**, 235425 (2001).

[7] H. Kawanowa, H. Ozawa, M. Ohtsuki, Y. Gotoh, and R. Souda, *Structure analysis of* $LaAlO_3$*(001) surfaces by low energy neutral scattering spectroscopy*, Surface Science **506**, 87 (2002).

[8] D. A. Schmidt, T. Ohta, Q. Yu, and M. A. Olmstead, *Influence of perovskite termination on oxide heteroepitaxy*, Journal of Applied Physics **99**, 113521 (2006).

[9] C. H. Lanier, J. M. Rondinelli, B. Deng, R. Kilaas, K. R. Poeppelmeier, and L. D. Marks, *Surface Reconstruction with a Fractional Hole:* $(\sqrt{5}\times\sqrt{5})R26.6$ $LaAlO_3$ *(001)*, Physical Review Letters **98**, 086102 (2007).

[10] R. Tromp, J. Hannon, A. Ellis, W. Wan, A. Berghaus, and O. Schaff, *A new aberration-corrected, energy-filtered LEEM/PEEM instrument. I. Principles and design*, Ultramicroscopy **110**, 852 (2010).

[11] S. M. Schramm, J. Kautz, A. Berghaus, O. Schaff, R. M. Tromp, and S. J. van der Molen, *Low-energy electron microscopy and spectroscopy with ESCHER: Status and prospects*, IBM Journal of Research and Development **55**, 1:1 (2011).

[12] S. M. Schramm, A. B. Pang, M. S. Altman, and R. M. Tromp, *A Contrast Transfer Function approach for image calculations in standard and aberration-corrected LEEM and PEEM*, Ultramicroscopy **115**, 88 (2012).

[13] R. Tromp, J. Hannon, W. Wan, A. Berghaus, and O. Schaff, *A new aberration-corrected, energy-filtered LEEM/PEEM instrument II. Operation and results*, Ultramicroscopy (2013).

[14] A. K. Schmid, W. wich, C. S. Rastomjee, B. Rausenberger, W. Engel, E. Zeitler, and A. M. Bradshaw, *Proceedings of the 14th European Conference on Surface ScienceThe chemistry of reaction-diffusion fronts investigated by microscopic LEED IV fingerprinting*, Surface Science **331**, 225 (1995).

[15] J. B. Hannon, J. Sun, K. Pohl, and G. L. Kellogg, *Origins of Nanoscale Heterogeneity in Ultrathin Films*, Physical Review Letters **96**, 246103 (2006).

[16] J. I. Flege and E. E. Krasovskii, *Intensityvoltage low-energy electron microscopy for functional materials characterization*, physica status solidi (RRL) Rapid Research Letters **8**, 463 (2014).

[17] T. Tachikawa, M. Minohara, Y. Nakanishi, Y. Hikita, M. Yoshita, H. Akiyama, C. Bell, and H. Y. Hwang, *Metal-to-insulator transition in anatase* TiO_2 *thin films induced by growth rate modulation*, Applied Physics Letters **101**, 022104 (2012).

5

Imaging pulsed laser deposition growth of homo-epitaxial $\mathrm{SrTiO_3}$ by Low-Energy Electron Microscopy

By combining low-energy electron microscopy with in-situ pulsed laser deposition we have developed a new technique for film growth analysis, making use of both diffraction and real-space information. Working at the growth temperature, we can use: the intensity and profile variations of the specular beam to follow the coverage in a layer-by-layer fashion; real-space microscopy to follow e.g. atomic steps at the surface; and electron reflectivity to probe the unoccupied band structure of the grown material. Here, we demonstrate our methodology for homo-epitaxial growth of $SrTiO_3$*. Interestingly, the same combination of techniques will also be applicable to hetero-epitaxial oxide growth, largely extending the scope of research possibilities.*

This chapter has been accepted as:

A.J.H. van der Torren, S.J. van der Molen, J. Aarts,
Imaging pulsed laser deposition growth of homo-epitaxial $SrTiO_3$ *by Low-Energy Electron Microscopy*
to be published in Nanotechnology

5.1 Introduction

Heterostructures of complex oxides have attracted great interest due to the possibility of combining a variety of physical properties by stacking multiple materials. Especially the 2-dimensional electron gas formed between the band insulators $SrTiO_3$ and $LaAlO_3$ has proven a fascinating research theme.[1,2]. The electronic properties of this electron gas are highly dependent on the substrate surface and the growth conditions[3–5].

To gain better control over the material properties, in-situ monitoring the growth, is of great importance. For the growth of these complex oxides, pulsed laser deposition (PLD) is the most widely used method to obtain high film quality. In-situ reflection high energy electron diffraction (RHEED) is commonly used for the growth monitoring, enabling layer-by-layer growth control[6–8]. However, this method only gives integral information and lacks spatial resolution. Spatially resolved measurements have been performed by scanning tunneling microscopy (STM)[9,10] and atomic force microscopy (AFM)[11], but these techniques can only be used after growth and not for in-situ monitoring. By combining PLD with low-energy electron microscopy (LEEM), we introduce a new possibility for layer-by-layer growth control combined with spatial resolution.

Here we present our development of pulsed laser deposition in a LEEM. We demonstrate this technique and the various imaging techniques that become available to study growth, in this case the growth of homo-epitaxial $SrTiO_3$. We show layer-by-layer growth control by spot-profile-analysis low-energy electron diffraction (SPA-LEED), while real-space images offer information on the terrace steps and surface morphology. Also, using energy-dependent electron reflectivity, we observe that the used growth conditions change the electronic structure.

5.2 Experimental

5.2.1 LEEM

The experiments were performed in the ”Escher” LEEM setup, an aberration corrected LEEM facility at Leiden University[12–15]. In principle, LEEM is a form of microscopy that makes use of low-energy electrons to create highly surface sensitive images. However, by now, LEEM has become an umbrella term for a diverse set of techniques that can all be applied in-situ and in real time. For a LEEM to perform optimally, high energy electrons are required for the electron optics to work best, while the energy at the sample has to be close to zero. In order to achieve this, electron gun and sample are lifted to -15 kV and -15 kV + E_0 respectively, with the rest of the machine grounded, to accelerate and decelerate the electrons. This results in a high electric field between the objective lens and the sample which are only 1.5 mm apart. By changing this field slightly, the landing energy E_0 of the electrons at the sample can be tuned between zero and a few hundred electron volts. After interaction with the sample, the same field accelerates the electrons back towards the objective lens after which they are deflected towards the aberration corrector and finally to the projector column. An essential part is the magnetic

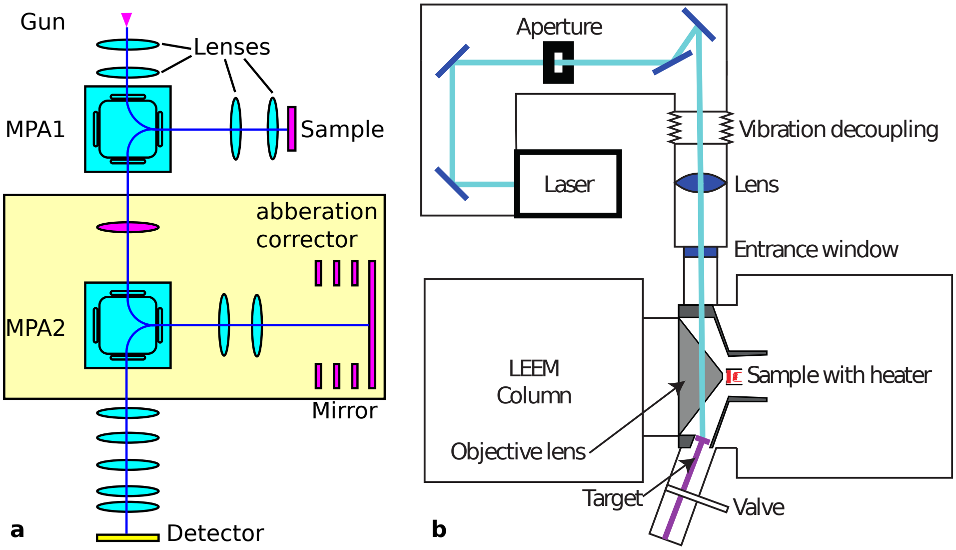

FIGURE 5.1: a) Sketch of the LEEM imaging system. Blue line shows the path of the electrons. The magnetic prism arrays are indicated by MPA1 and MPA2. b) The pulsed laser deposition setup incorporated into the LEEM. The target, objective lens and sample are to scale, the other components are not. The full laser path is enclosed for safety reasons.

prism array (MPA) splitting the pathways of the incoming electrons from the gun and outgoing electrons towards the detector. Images are finally obtained by amplifying the signal with a multichannel plate and converting the electrons to photons with a phosphor screen. The signal is then detected by a 12-bit ccd camera. A detailed sketch of the full imaging system is shown in figure 5.1(a).

5.2.2 In-situ pulsed laser deposition

The in-situ PLD system was designed along the following lines: The target-to-sample position was chosen to be between 40 and 60 mm as used in many PLD setups. For optimal performance of the microscope, the positions of sample and objective lens are fixed. This combination resulted in the target position as shown in figure 5.1(b). The target is placed on a linear transfer arm, allowing to change the target-to-sample distance. Every sample grown is ablated from a different area by rotating the target. A valve is added to allow replacement of the target without breaking the vacuum of the sample chamber. For the pulsed laser deposition a KrF excimer laser (Coherent COMPex Pro 201), 248 nm wavelength, is used. A uniform part of the laser spot is selected by a 5 x 15 mm aperture which is imaged on the target using a lens with a 407 mm focal length. This results in a 1/7 times magnification at the target. The laser hits the target under an angle of 22 degrees along the long side and 36.5 degrees along the short side of the laser beam, resulting in a 0.9 x 2.3 = 2.1 mm^2 exposed area on the target. For the fluence calculation, the energy is measured right after the aperture and a loss at the entrance window of 8% is taken into account. In order to change the fluence the power of the laser or the magnification of the imaging system can be changed. The sample-to-target position for the samples discussed in this paper was chosen to be 50 mm.

The material plume created after ablation from the target contains charged particles. These particles would break down the high electric field between objective lens and sample, with the risk of damaging the sample. In order to combine the low-energy electrons with the PLD we perform the deposition and imaging alternating in time. Before deposition, the ppm-stable voltage supply is ramped down in less than 15 seconds. The laser is started once the voltage is below 2 kV and will apply the first deposition pulses when the field is only several tens of volts. When the deposition is finished the sample voltage is automatically ramped up and is stable again with ppm stability at 15 kV within 11 seconds. The sample can now be imaged. We take diffraction images over an energy range typically from 0 to 30 eV, from which we can obtain film properties and film thickness as will be discussed in the results section. More imaging techniques can be added if required. By repeating this cycle of deposition and imaging many times per atomic layer, the growth can be studied carefully. In practice, a balance needs to be found between the need for information and the growth time for a layer. Although the typical growth time is 30 s per monolayer, it takes about 25 minutes for the deposition of one unit cell when basic characterization is performed for every 0.1 unit cell. During the whole experiment, the sample is heated with an electron bombardment heater from the back. Stable deposition and imaging can be done up to 1000 °C and 10^{-4} mbar of oxygen. The background pressure of the system is 10^{-9} mbar and by differential pumping these UHV conditions are preserved in the the electron gun and projector column.

5.2.3 LEEM extensions

To be able to obtain maximum information from the diffraction images, spot profile analysis of the low-energy electron diffraction spots (SPA-LEED) is performed. However, in the typical range of measured energies the variation in intensity of the reflected electrons can be up to almost 10^4. This makes small signals undetectable with the 12-bit CCD camera (image depth: 4096). Dynamically changing the signal amplification solves this problem and is achieved by automatically adapting the channel plate gain. In this way, the maximum intensity on the CCD can be kept around 75% of its maximum, resulting in maximal image depth to resolve the spot profiles without damaging the channel plates. We characterized our channel plates and found the gain to follow $I = (I_{cmr} - b)e^{-GV_{cp}}$, where I_{cmr} is the intensity measured by the camera, b the background signal, mainly caused by the CCD readout noise, V_{cp} is the voltage over the channel plates in kV, G is the gain and I is the final intensity. The gain was calibrated to be equal to 20 kV^{-1}. Realistic values of the channel plate voltage lie between 0.9 kV and 1.7 kV allowing for more than six orders of magnitude range in intensity. During the measurement of an IV-curve (the intensity versus incoming-electon-energy), we calculate the channel plate voltage required to saturate the CCD up to 75% after every image. This calculated channel plate voltage is used to capture the next image. By taking small steps through energy we expect the next image to be close in intensity to the current image, thus falling within range of the camera without further adjustments. By placing an aperture around the appropriate diffraction spot we avoid burning the channel plates due to other bright spots. Using this method we also optimized our earlier developed technique of angle-resolved reflection electron spectroscopy (ARRES)[16]. This technique will be further explained in section 5.3.4.

5.2.4 Sample preparation

Single crystals from Crystec GmbH were used as PLD target and as substrates for growth. The target-crystals were used as-received without further treatment while the sample substrates were prepared to be TiO_2-terminated. To obtain the TiO_2-termination, substrates were ultrasonicated in demineralized-water, etched for 30 s in buffered HF and annealed for one hour under oxygen flow[17]. The surface termination is verified by atomic force microscopy (AFM). Three samples were measured and will be called A to C. For real space experiments on sample B, markers were created to correct for sample drift. These markers are made by e-beam lithography and Ar-ion etching, and provide clear contrast in LEEM. For the PLD growth a pressure of 5×10^{-5} mbar was used for all samples and a 1 Hz repetition rate. Laser fluencies and growth temperatures for the three samples were as follows: sample A (1.4 J/cm^2, 665 °C), sample B (1.4 J/cm^2, 800 °C) and sample C (1 J/cm^2, 690 °C). Temperatures were measured by a pyrometer set to an emissivity of 0.8.

5.3 Results and discussion

The homo-epitaxial growth of $SrTiO_3$ strongly depends on the growth conditions. In the following we will show how the wide range of imaging techniques available in the LEEM allows in-situ characterizations of this growth.

Figure 5.2(a) shows a diffraction pattern of the bare $SrTiO_3$. A square surface net is clearly visible as well as traces of a 2x1 reconstruction. This surface reconstruction is described in earlier research[19–23]. Our temperature and pressure are very comparable to those used by Hesselberth *et al.*[23], who reported the reconstruction to form in UHV between 600 °C and 800 °C and to disappear in an oxygen pressure of 2×10^{-4} mbar. The origin of the reconstruction is believed to be oxygen loss. Our oxygen pressure of 5×10^{-5} mbar is in an intermediate regime where probably only part of the oxygen disappears, resulting in only a small amount of reconstruction.

More information can be obtained from the diffraction pattern by studying the shape and intensity of the specular beam. Figure 5.2(b) shows its maximum intensity as a function of landing energy. These so-called IV-curves, which measure the reflectivity of the surface, are correlated to the unoccupied band structure of the sample as we will discuss in section 5.3.4. For now we use it as a fingerprint of the

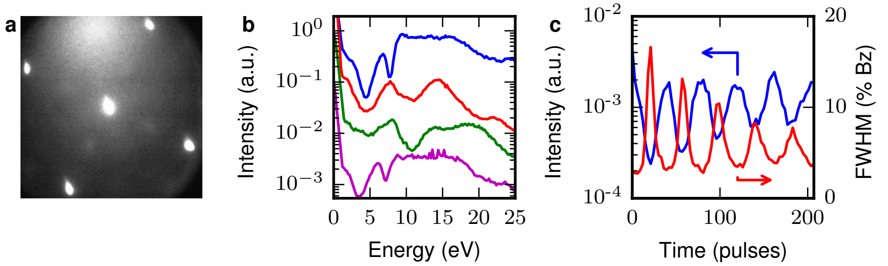

FIGURE 5.2: a) Diffraction pattern at bare TiO_2-terminated $SrTiO_3$ at 17 eV. A square surface net is visible, and traces of a 2x1 surface reconstruction. b) Maximum intensity versus landing energy of the specular spot for bare $SrTiO_3$ (blue, top) and after depositing 200 pulses of $SrTiO_3$ (red, 2nd from top). A reference curve on SrO-terminated $SrTiO_3$ substrate[18] (green, 3rd from top) and finally, an IV-curve after ex-situ annealing in an oxygen flow at 950 °C for one hour (magenta, bottom) are also shown. Data are taken on sample A. Curves are shifted for clarity. c) Maximum intensity (blue) and FWHM (red) of the specular spot versus layer thickness at a landing energy of 32 eV for sample A grown at 1.4 J/cm^2, 700 °C. The FWHM is presented in % Bz, the percentage of the Brillouin zone as measured by the average distance between the specular and first order spots.

material. Clear differences can be observed between bare TiO_2-terminated $SrTiO_3$ (figure 5.2(b), blue line, top) and the IV-curve taken after growth at sample A (figure 5.2(b), red line, 2nd from top). The IV-curve has strongly changed, in particular between 10 and 20 eV. This can both be due to the low oxygen pressure and/or be the result of off-stoichiometric (Sr/Ti ratio) growth. To investigate if off-stoichiometric growth could lead to Sr-excess on the surface, changing our IV-curve away from the TiO_2-termination fingerprint, we compare our results with a SrO-terminated $SrTiO_3$ sample. A sample with a double layer of SrO on TiO_2-terminated $SrTiO_3$ was grown in a different PLD system[18] and the resulting IV-curve is shown in figure 5.2(b) (green line, 3rd from top). This curve of SrO-termination is very similar to the after growth (red line, 2nd from top) curve for energies up to 15 eV, suggesting the presence of excess SrO. The excess SrO should be removable by the etching step performed to obtain TiO_2-terminated $SrTiO_3$. To confirm this, the IV-curve result after re-etching the grown surface in HF and annealing in oxygen flow for one hour at 950 °C is shown in figure 5.2(b) (magenta line, bottom). This IV-curve shows again the fingerprint of TiO_2-termination, confirming the grown $SrTiO_3$ had an excess of SrO on the surface.

5.3.1 Following the growth

Figure 5.2(c) show the maximum intensity (blue) and the full width at half maximum (FHWM) (red) versus growth time of the specular beam at a landing energy of 32 eV. The FWHM here is determined by averaging the horizontal en vertical sections of 60 pixels from the center of the specular beam and fitting the result by a single Lorentzian function of which the FWHM can be easily obtained. Even in cases where the spot shows structure as will be encountered later on, the single Lorentzian fit results in a reasonable approximation of the FWHM. The FWHM is presented in units of %Bz, where 100 %Bz is the size of the Brillouin zone determined as the averaged distance between the specular and first order spots of the substrate, measured as 294 pixels on the camera.

Clear oscillations, fading out with thickness, can be observed. The FWHM is out of phase with the intensity as expected. The oscillations are correlated with the surface roughness. For flat surfaces i.e. multiples of a full unit cell grown, the diffraction pattern is sharp (i.e. small FWHM, high intensity). When material is deposited, the surface roughens and the diffraction spots broaden (i.e. large FHWM, low intensity).

From these oscillations we can conclude layer-by-layer growth for the first unit cells grown. The damping is a result of a change in growth mode to bigger islands, possibly caused by a change from layer-by-layer growth to a more three dimensional growth.

5.3.2 Real space

Growth can also be imaged in real space. Figure 5.3 shows LEEM bright field images for every half unit cell grown. For the full unit cells we observe a clear phase

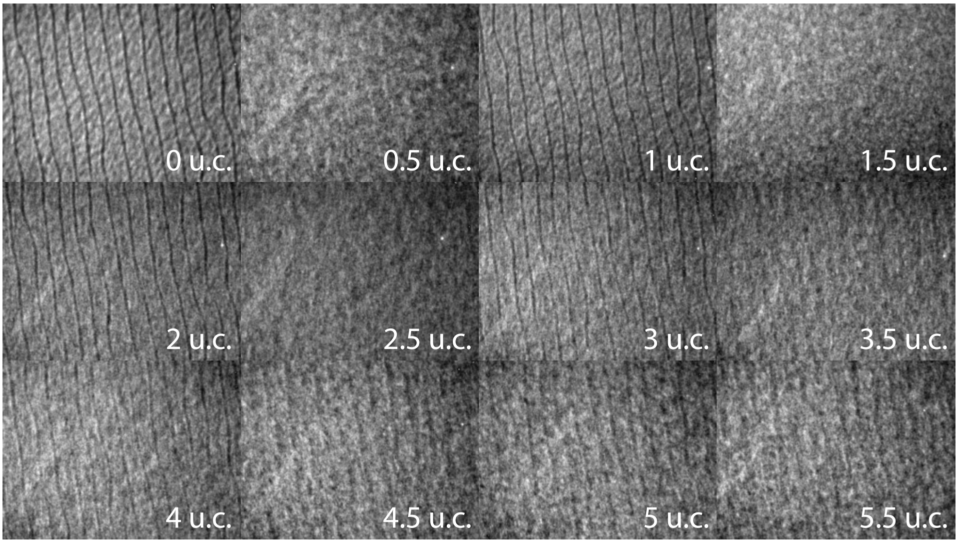

FIGURE 5.3: Normalized bright field images for every half unit cell up to 5.5 u.c, taken at 18 eV on sample B grown at a fluence of 1.4 J/cm^2. For full unit cell, terrace steps are visible as black lines by phase contrast. For half unit cell coverage the contrast disappears. At thicker layers 3D growth makes the intensity oscillations fade out.

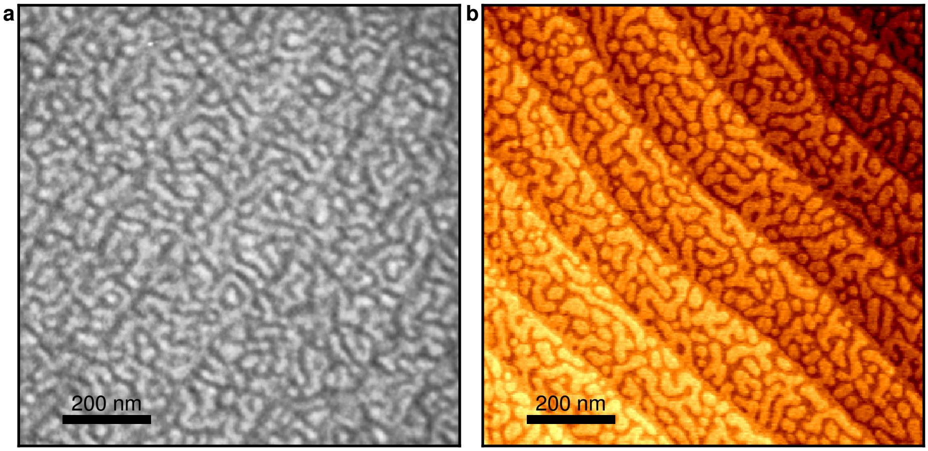

FIGURE 5.4: a) Bright field image at 13.6 eV after growth on sample C, grown at 700 °C and 1 J/cm^2. b) AFM image at same sample, but different area.

contrast at the terrace edges, visible as black lines due to destructive interference. On the other hand, at half unit cell coverage, the contrast has disappeared. The deposited material creates steps everywhere on the terrace, which are too small to detect. For thicker layers we also observe non-perfect growth. The step edges become blurred at full layer coverage, while for half layer coverage they do not fully disappear. Furthermore the real space images show that the step edges do not move, i.e. there is no step flow growth at this temperature.

In figure 5.4(a) we show a sample C which is grown with a fluence of 1 J/cm^2, instead of 1.4 J/cm^2. This changes the growth mode as can be clearly seen in the bright field image figure 5.4(a) and AFM image figure 5.4(b). The islands formed during the growth of a new layer are much bigger than in the other samples and can be clearly distinguished in bright field and AFM. These images are taken after growth of 225 pulses, just under 10 unit cells.

5.3.3 Spot-profile-analysis low-energy electron diffraction

Combining energy dependence (figure 5.2(b)) and growth time (figure 5.2(c)) for all energies one can create a full map. The specular beam intensity and FWHM variations can actually be measured at all energies, which results in the maps in figure 5.5(a), (b).

We observe a regular pattern in energy as well as in time. This is most clearly seen in the FWHM image of figure 5.5(b). To understand the energy dependence, we converted the energy axis to scattering phase[24] as shown on the axis on the right hand side of figure 5.5. The scattering phase is defined as $S = \frac{k_\perp d}{2\pi}$, with d the height of a unit cell $SrTiO_3$ and $k_\perp$ the out-of-plane wave vector. For the specular

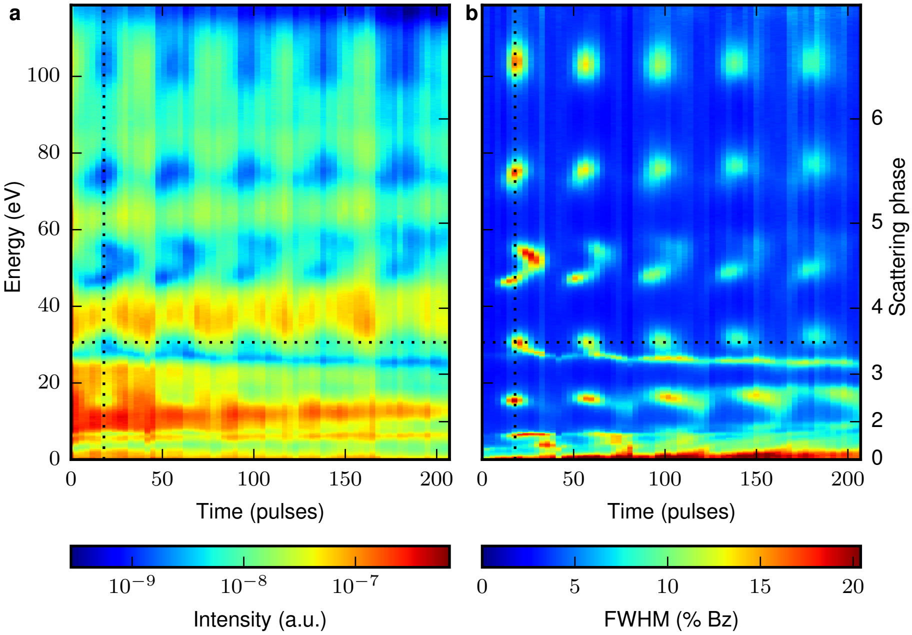

FIGURE 5.5: A map with intensity (left) and FWHM (right) of the specular beam on sample A. On the x-axis the time in units of pulses deposited is plotted while on the y-axis energy (left) or scattering phase (S) (right) is shown. S is defined in the text. The oscillations in energy follow the oscillations expected from the scattering phase. The peak splitting at S = 4.5 is not understood. Horizontal dotted line corresponds with the energy used for figure 5.2 and the vertical dotted line with half a unit cell where the data in figure 5.6 is taken.

spot $k_\perp = k$ (i.e. there is no in-plane component) and $S = \frac{kd}{2\pi} = 2d\sqrt{\frac{E(eV)}{150.4}}$. Here the zero of the energy, which depends on the gun potential and the work function of the sample, is determined by aligning the integer scattering phase values to the minima of the FWHM oscillations. When S is integer the electrons are in the in-phase (Bragg) condition. In this Bragg condition the electrons constructively interfere and are insensitive to the surface roughness. The diffraction spot is always sharp, i.e. the FWHM is low. For half integer values the electrons are in the out-of-phase (anti-Bragg) condition and destructively interfere at the terrace edges. When half a unit cell is grown the surface roughness is maximal (at least when the growth mode is island growth) and the specular beam has its maximum width. The effect of the scattering phase is more clear from the figure 5.6, where maximum intensity (blue) and FWHM (red) are plotted as function of scattering phase S for 1/2 unit cell of homo-epitaxial $SrTiO_3$. The scattering phase is in good agreement with the FWHM oscillations, except for S = 4.5 where the FWHM spot is split.

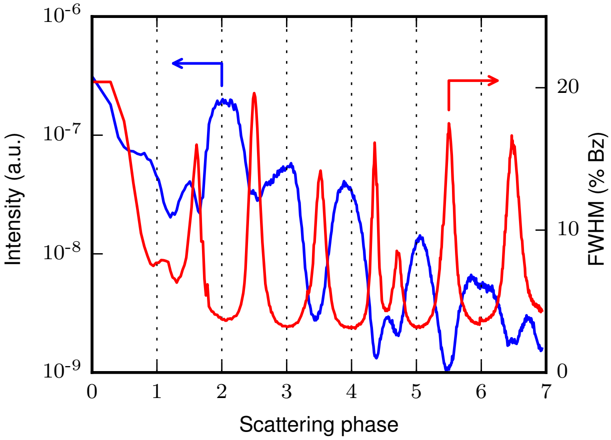

Figure 5.6: Maximum intensity (blue) and FWHM (red) of the specular beam versus scattering phase (S) after growth of 0.5 unit cell of homo-epitaxial $SrTiO_3$. The FWHM shows clear minima at integer values of the scattering phase and maxima at half integers. An exception is S = 4.5 where we observe a minimum instead of a maximum.

The cause of this splitting, which is also clearly visible in figure 5.5(b), is not understood. Other samples we measured showed the same behavior. We also note that for energies with a scattering phase below one, the interference signal deteriorates since not all electrons touch the surface any more before starting the return path.

Figure 5.7 presents a detailed view on the spot profiles at half a unit cell homo-epitaxial growth of $SrTiO_3$. The spot profiles in the anti-Bragg condition are broader than in the Bragg condition and they are actually split into two peaks, indicating a new diffraction condition caused by a regular terrace structure. This peak splitting is not found for S = 1.5 and S = 4.5. For S = 1.5 the electron wavelength of 0.55 nm is probably too large to resolve this terrace structure and at S = 4.5 we observe a small but sharp peak in agreement with the minimum observed in the FWHM in figure 5.6, which we cannot explain.

From the spot shape a more quantitative result can be extracted. The newly grown material forms small islands on the surface, slowly filling up a full layer. The characteristic parameters of this island formation are the average island size and the island size distribution width. These parameters can be extracted from the diffraction spot shape as discussed in ref.[25]. As an illustration the spot profiles for consecutive (n+$\frac{1}{2}$) unit cells (n integer) at S = 6.5 are plotted in figure 5.8(a), starting with 0.5 unit cell (blue, top) up to 4.5 unit cell (magenta, bottom).

These spot profiles can be reasonably well fitted with two Lorentzians, mirrored

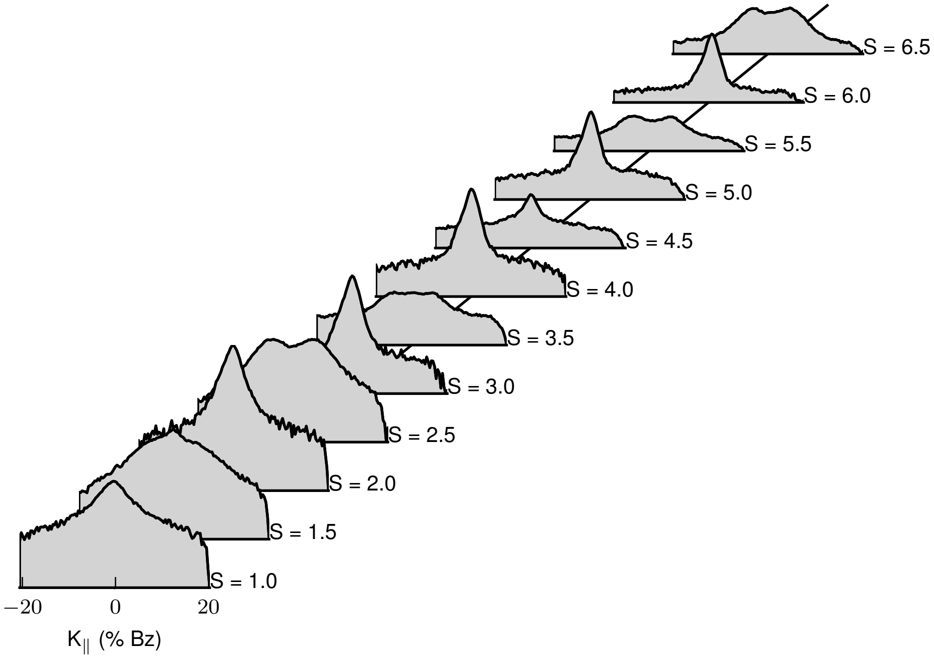

FIGURE 5.7: The beam shape vs scattering phase (S) for a half unit cell $SrTiO_3$ grown on sample A. The plot is on a log scale with background subtracted.

around the Brillouin zone center $x = 0$, as follows:

$$L_{double}(x) = A\left(\frac{\Gamma^2}{\Gamma^2 + (x - x_0)^2} + \frac{\Gamma^2}{\Gamma^2 + (x + x_0)^2}\right)$$

where A is the amplitude, 2Γ the FWHM of the Lorentzian and $2x_0$ the separation of the Lorentzians. Fits are shown in figure 5.8(a) as dotted lines. For very sharp island size distributions the diffraction spot would be split in two separate Lorentzians and the island size s_{island} can be obtained from the peak splitting $2x_0$. In our case the Lorentzians are strongly broadened and the peak splitting $2x_0$ and FWHM 2Γ are strongly correlated. Wollschläger[25] modeled the spot shape for the transition from sharp to broad island size distributions and the effect on the FWHM and spot splitting when this spot shape is approximated by two Lorentzians. In figure (3b) of his paper he plots the result for broad distributions, i.e. where the ratio of the standard deviation (σ) and island size (s_{island}) is greater than $\frac{\sigma}{s_{island}} > 0.6$. Figure 5.8(b) shows the island size s_{island} (blue, top) and distribution width σ (red, bottom) as obtained by applying the results of figure (3b) from Wollschläger on Γ and x_0. The ratio of σ/s_{island} confirms we are in the broad distribution limit.

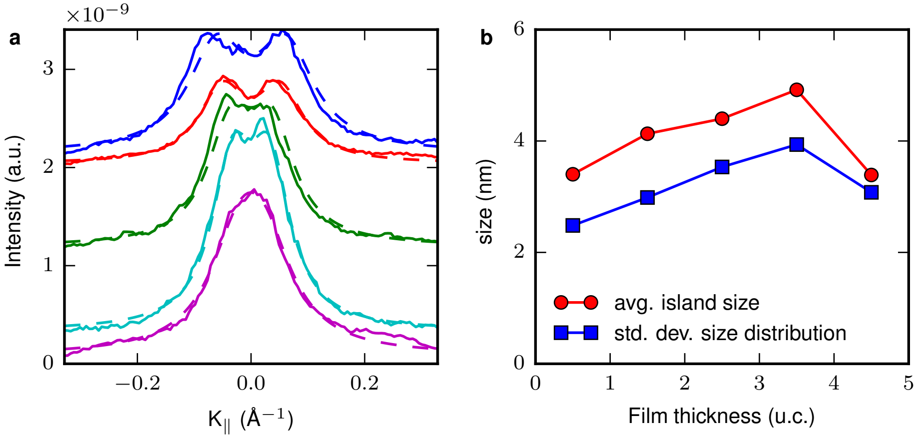

FIGURE 5.8: a) The beam profile at S = 6.5 on sample A, depending on layer thickness, shifted for clarity. From top to bottom 0.5, 1.5, 2.5, 3.5, 4.5 u.c. The spots become sharper over time, except at 4.5 u.c., indicating bigger island sizes. b) The average island size s_{island} versus layer thickness (blue, top) and the standard deviation of island size distribution σ (red, bottom).

Compared to literature our terraces sizes are relatively small. It is close to findings of Phark *et al.*[10], while Xu *et al.*[11] found much bigger island sizes, in the order of tens of nanometers. This can probably be explained by the relative low temperature of 670 °C, which is closer to Phark *et al.* (580 °C) and lower than the one used by Xu *et al.* (800 °C). The advantage of our technique above the earlier used AFM and STM is the continuous tracking over thickness at growth conditions, without the need for cooling down or sample transfer.

5.3.4 Angle-resolved reflection electron spectroscopy

As stated earlier the IV-curve in figure 5.2(b) is correlated with the unoccupied band structure of the material. In particular, the electron reflection probability is high when there is a band gap at that specific energy while the reflection probability is low when an electron can couple into an electronic state(1). Here zero energy corresponds with the vacuum level and thus the states probed are above the vacuum level, i.e. the unoccupied band structure. Figure 5.9(a) shows how the IV-curves change with time when homo-epitaxial $SrTiO_3$ is grown on sample A. For the $SrTiO_3$ substrate there is a small band gap at 8 eV and a large band gap between 10 and 17 eV. The small band gap stays constant during growth while the large band gap sharpens to only a small band gap around 15 eV. The change is more clear if we not only look at the landing energy E_0 but also at the in-plane momentum of the electron, $k_{\parallel}$. The electron reflectivity now depends on (E_0, $k_{\parallel}$) and a full

---

(1) Multiple scattering effects can influence the result.

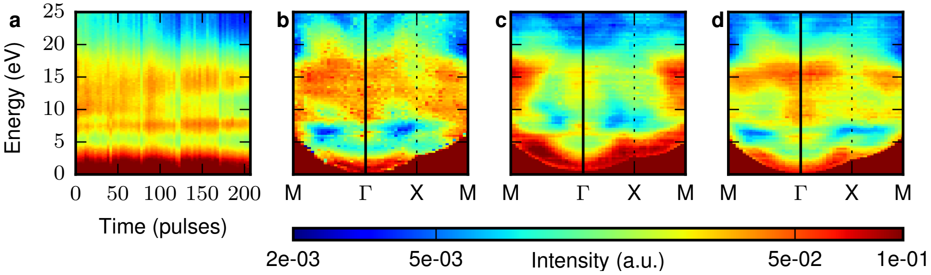

FIGURE 5.9: a) IV-curves versus growth time for sample A grown at 1.4 J/cm^2. b) ARRES map on bare typical TiO$_2$-terminated SrTiO$_3$ (not on sample A). c) ARRES map on sample A after growth and d) ARRES map after reviving the surface by a single termination step.

unoccupied band structure map can be made. Mapping the full energy versus $k_{\|}$ behavior is called angle-resolved reflection-electron spectroscopy (ARRES)[16]. Changing the in-plane momentum is achieved by deflecting the electron beam just behind the electron gun. The resulting in-plane momentum can be determined from the position of the specular spot in the Ewald-sphere. In practice, the deflection of the beam allows to reach the Brillouin zone edge comfortably. Figure 5.9(b), (c) and (d) show ARRES maps for bare TiO$_2$-terminated SrTiO$_3$, for sample A after growth of 5 unit cells of SrTiO$_3$ and after a single termination procedure where the sample after growth is etched in a buffered HF and ex-situ annealed in an oxygen flow at 950 °C. The IV-curves shown earlier are vertical cuts at the Γ-point, as indicated with a vertical black line. The large band gap between 8 and 17 eV at the SrTiO$_3$ substrate extends to the direction of the M and X-point. This band gap strongly changes after the growth. It shrinks and is not connected towards the M and X-point anymore. The bands around 6 eV halfway towards the M and X-point have moved upwards, making space for a large band gap at the lowest energies. After the single termination procedure the band gap between 8 and 17 eV has recovered to a great extent and the band gap at the lowest energies has shrunk back to the size seen at the SrTiO$_3$ substrate. This is also clear in figure 5.2(b), where in particular the behavior around 6-8 eV changes. Here, the bare SrTiO$_3$ shows a dip, the sample after growth a peak, and the annealed sample again a dip. The single termination procedure appears to do two things. In the first place excess SrO which is collected on the surface due to the off-stoichiometric growth is removed. Secondly, the anneal step replenishes any oxygen vacancies that are created during growth. The two steps together regenerate the surface of the stoichiometric SrTiO$_3$.

5.4 Conclusion

In summary, combining LEEM with PLD provides a unique possibility to in-situ analyze the growth of perovskites by the possibility to combine SPA-LEED with real space and unoccupied band structure information. We demonstrated this with the growth of homo-epitaxial $SrTiO_3$.

From the specular spot shape images and real space images we can conclude that the growth mode slowly changes from layer-by-layer growth to more 3 dimensional growth. Roughness oscillations slowly damp out, the size of the islands from which the newly grown layer forms slowly increases and in real space the difference between half and full unit cell grown disappears. The growth mode depends on the growth conditions. For low fluence we have seen microscopic island sizes, clearly distinguishable in real space. The electronic structure changes during the growth of homo-epitaxial $SrTiO_3$. This can be caused by off-stoichiometric growth as well as by oxygen vacancies due to the low oxygen pressure during growth. The excess SrO can be removed by buffered HF and the oxygen can be replenished by ex-situ annealing in an oxygen flow. These steps partially recover the ARRES map found in the stoichiometric $SrTiO_3$ substrate.

The full range of possibilities offered by LEEM clearly allows to perform thorough studies during growth of perovskites, making it possible to draw conclusions during growth without performing ex-situ studies afterwards.

References

[1] A. Ohtomo and H. Y. Hwang, *A high-mobility electron gas at the $LaAlO_3$/$SrTiO_3$ heterointerface*, Nature **427**, 423 (2004).

[2] S. Thiel, G. Hammerl, A. Schmehl, C. W. Schneider, and J. Mannhart, *Tunable Quasi-Two-Dimensional Electron Gases in Oxide Heterostructures*, Science **313**, 1942 (2006).

[3] M. P. Warusawithana, C. Richter, J. A. Mundy, P. Roy, J. Ludwig, S. Paetel, T. Heeg, A. A. Pawlicki, L. F. Kourkoutis, M. Zheng, M. Lee, B. Mulcahy, W. Zander, Y. Zhu, J. Schubert, J. N. Eckstein, D. A. Muller, C. S. Hellberg, J. Mannhart, and D. G. Schlom, *$LaAlO_3$ stoichiometry is key to electron liquid formation at $LaAlO_3$/$SrTiO_3$ interfaces*, Nature Communications **4** (2013).

[4] D. G. Schlom and J. Mannhart, *Oxide electronics: Interface takes charge over Si*, Nature Materials **10**, 168 (2011).

[5] A. Sambri, D. V. Cristensen, F. Trier, Y. Z. Chen, S. Amoruso, N. Pryds, R. Bruzzese, and X. Wang, *Plasma plume effects on the conductivity of amorphous-$LaAlO_3$/$SrTiO_3$ interfaces grown by pulsed laser deposition in O2 and Ar*, Applied Physics Letters **100**, 231605 (2012).

[6] G. Rijnders, Ph.D. thesis (2001).

[7] G. Koster, G. J. H. M. Rijnders, D. H. A. Blank, and H. Rogalla, *In situ initial growth studies of $SrTiO_3$ on $SrTiO_3$ by time resolved high pressure RHEED*, Materials Research Society symposia proceedings pp. 33–37 (1998).

[8] M. Lippmaa, N. Nakagawa, M. Kawasaki, S. Ohashi, Y. Inaguma, M. Itoh, and H. Koinuma, *Step-flow growth of $SrTiO_3$ thin films with a dielectric constant exceeding 104*, Applied Physics Letters **74**, 3543 (1999).

[9] S.-h. Phark, Y. J. Chang, and T. Won Noh, *Selective growth of perovskite oxides on $SrTiO_3$ (001) by control of surface reconstructions*, Applied Physics Letters **98**, 161908 (2011).

[10] S.-h. Phark and Y. J. Chang, *Nucleation and growth of primary nanostructures in $SrTiO_3$ homoepitaxy*, Nanoscale Research Letters **10**, 80 (2015).

[11] C. Xu, M. Moors, and R. Dittmann, *Impact of cation stoichiometry on the early stage of growth of $SrTiO_3$ deposited by pulsed laser deposition*, Applied Surface Science **359**, 68 (2015).

[12] R. Tromp, J. Hannon, A. Ellis, W. Wan, A. Berghaus, and O. Schaff, *A new aberration-corrected, energy-filtered LEEM/PEEM instrument. I. Principles and design*, Ultramicroscopy **110**, 852 (2010).

[13] S. M. Schramm, J. Kautz, A. Berghaus, O. Schaff, R. M. Tromp, and S. J. van der Molen, *Low-energy electron microscopy and spectroscopy with ESCHER: Status and prospects*, IBM Journal of Research and Development **55**, 1:1 (2011).

[14] S. M. Schramm, A. B. Pang, M. S. Altman, and R. M. Tromp, *A Contrast Transfer Function approach for image calculations in standard and aberration-corrected LEEM and PEEM*, Ultramicroscopy **115**, 88 (2012).

[15] R. Tromp, J. Hannon, W. Wan, A. Berghaus, and O. Schaff, *A new aberration-corrected, energy-filtered LEEM/PEEM instrument II. Operation and results*, Ultramicroscopy (2013).

[16] J. Jobst, J. Kautz, D. Geelen, R. M. Tromp, and S. J. van der Molen, *Nanoscale measurements of unoccupied band dispersion in few-layer graphene*, Nature Communications **6**, 8926 (2015).

[17] M. Kawasaki, K. Takahashi, T. Maeda, R. Tsuchiya, M. Shinohara, O. Ishiyama, T. Yonezawa, M. Yoshimoto, and H. Koinuma, *Atomic Control of the $SrTiO_3$ Crystal Surface*, Science **266**, 1540 (1994).

[18] C. Xu and R. Dittmann, *growth of SrO-terminated $SrTiO_3$ sample.*

[19] N. Erdman, K. R. Poeppelmeier, M. Asta, O. Warschkow, D. E. Ellis, and L. D. Marks, *The structure and chemistry of the TiO_2-rich surface of $SrTiO_3$ (001)*, Nature **419**, 55 (2002).

[20] N. Erdman and L. D. Marks, *$SrTiO_3$(001) surface structures under oxidizing conditions*, Surface Science **526**, 107 (2003).

[21] T. Kubo and H. Nozoye, *Surface structure of $SrTiO_3$(100)*, Surface Science **542**, 177 (2003).

[22] M. R. Castell, *Scanning tunneling microscopy of reconstructions on the $SrTiO_3$(001) surface*, Surface Science **505**, 1 (2002).

[23] M. B. S. Hesselberth, S. J. v. d. Molen, and J. Aarts, *The surface structure of $SrTiO_3$ at high temperatures under influence of oxygen*, Applied Physics Letters **104**, 051609 (2014).

[24] M. Horn-von Hoegen, *Growth of semiconductor layers studied by spot profile analysing low energy electron diffraction Part I1*, Zeitschrift fr Kristallographie - Crystalline Materials **214**, 591 (1999).

[25] J. Wollschlger, *Simple analysis of spot splitting due to diffraction at surfaces with atomic steps*, Surface Science **383**, 103 (1997).

6

Finding signatures of the conducting $LaAlO_3/SrTiO_3$ interface at the growth temperature by electron reflection

The two-dimensional electron gas occurring between the band insulators $SrTiO_3$ and $LaAlO_3$ has attracted a lot of interest. The formation of this conducting interface is sensitive to the growth conditions, but despite numerous investigations, there are still questions about the details of the physics involved. In particular, not much is known about the electronic structure of the growing $LaAlO_3$ layer at the growth temperature (around 800°C) in oxygen (pressure around 5×10^{-5} mbar), since analysis techniques at these conditions are not readily available. For this we developed a pulsed laser deposition system inside our low-energy electron microscope. Our setup allows for layer-by-layer growth control and in-situ measurements of the angle-dependent electron reflection intensity. This gives information on the surface layers as a fingerprint of their electronic structure during the growth.

This chapter will be submitted as:

A.J.H. van der Torren, Z. Liao, C. Xu, N. Gauquelin, C. Yin, J. Aarts, S.J. van der Molen,
Finding signatures of the conducting $LaAlO_3/SrTiO_3$ interface at the growth temperature by electron reflection

6.1 Introduction

Transition metal oxides, and in particular perovskites, form an exciting class of materials exhibiting a variety of physical phenomena such as superconductivity, magnetism and ferroelectricity. Expecially interesting for possible electronics applications was the discovery of the formation of a two-dimensional electron gas between the two band insulators $LaAlO_3$ and $SrTiO_3$ [1]. The emergence of this conducting interface can at least partially be explained by the so-called polar catastrophe model. In this model an increasing electrical potential builds up when charged $(LaO)^+$ and $(AlO_2)^-$ layers are alternatively stacked on top of neutral $SrTiO_3$. This potential is compensated by the transfer of half an electron from the surface to the interface. A relevant observation is that the electron gas only forms when the top $LaAlO_3$ layer is at least four unit cells thick [2]. Only for this thickness the potential buildup is apparently enough to transfer the electron to the interface. Furthermore, the electron gas only forms at the n-type interface (TiO_2/AlO_2) and not at the p-type interface (SrO/LaO) [1]. At the p-type interface a structural reconstruction is energetically favorable above the electronic reconstruction [3].

While these observations are in favor of the electronic reconstruction, defects in the crystal and in particular in the TiO_2-layer, also play an important role in the formation of the electron gas. Not surprisingly, therefore, it is very much the growth conditions which determine the conducting properties of the interface. Pulsed laser deposition (PLD) is the most commonly used technique to grow $LaAlO_3/SrTiO_3$ heterostructures. Here the exact plume shape and composition as well as the oxygen pressure are of great importance, influencing the cationic stoichiometry [4–6] of the $LaAlO_3$ film and the number of oxygen vacancies in the $SrTiO_3$ [7]. A La/Al-ratio exceeding 0.97 [4] has been shown to totally suppress the conductivity. Furthermore, magnetism [7–10] and superconductivity [11–13] have been shown to occur at low temperatures, depending on the oxygen pressure during growth.

Whereas differences in growth conditions are known to lead to conducting or insulating samples as measured afterwards, little is known about how the electronic properties of the material develop during growth. Unfortunately, electrical measurements are very difficult at the high growth temperatures.

Also, the high temperatures and high oxygen pressure required during growth limit the abilities for in-situ analysis. Most techniques cannot work in this environment. For this reason we recently developed an in-situ pulsed laser deposition system for our low-energy electron microscope. This not only allows for layer-by-layer growth control and structural information but also allows measurements of the electron reflectivity of the surface with sub-unit cell precision, which yields information on the empty band structure [14].

Here we use this information to investigate the differences in (surface) electronic structure between conducting and insulating samples. We will focus on the changing electron reflectivity during growth at the growth temperature.

6.2 Experimental setup and sample preparation

The $LaAlO_3/SrTiO_3$ interfaces are grown and studied in an aberration corrected low-energy electron microscope (LEEM) at Leiden university, called ESCHER[15–18]. This technique has been used before to study $SrTiO_3$[19] and $LaAlO_3$[20] separately but now a pulsed laser deposition (PLD) system has been developed inside the LEEM to allow for analysis during growth, see chapter 5. In order to study growth, pulsed deposition is performed alternatingly with LEEM imaging. In more detail, between every few pulses deposited, the LEEM is turned on (i.e. the high voltage between objective lens and sample, required for the low-energy electrons, is turned on) and diffraction images are obtained. From the diffraction images the intensity and shape of the specular diffraction spot is investigated for layer-by-layer growth control. After this measurement the high voltage is turned off and deposition can continue. For the layer-by-layer growth control we obtain the full-width-half-max (FWHM) and peak intensity of the specular spot. The FWHM and intensity oscillate with the surface roughness due to spot broadening. To obtain a fingerprint of the unoccupied band structure, angle-resolved reflected electron spectroscopy (ARRES) is also performed[14]. In this technique the electron reflection is measured depending on energy and in-plane wave vector. For the ARRES measurements we obtain the total spot intensity which is independent of the surface roughness i.e. the total intensity stays constant when the surface roughens since the spot broadening lowers the maximum.

As substrates, $SrTiO_3$ (100) single crystals from CrysTec GmbH are used which are TiO_2-terminated by a buffered HF etch[21] and annealing in oxygen at 950 °C for one hour. The SrO-terminated substrate was prepared in a different PLD system by growing a double SrO-layer on a TiO_2-terminated substrate. For the PLD targets, single crystals $LaAlO_3$ (100) from Crystal GmbH were used. The PLD growth is performed at a pressure of 5.5×10^{-5} mbar oxygen and if not otherwise stated at a 2 J/cm^2 laser fluence with 1 Hz repetition rate. Depending on deposition speed, the deposition is briefly intermitted each 5 to 50 pulses to perform imaging and spectroscopy. This results in around 10 measurements per unit cell grown. Samples are grown at temperatures between 800 and 860 °C as measured with a pyrometer (emissivity 0.8). Temperature-dependent resistance measurements were performed in a Physical Properties Measurement System (PPMS, Quantum Design) in a van der Pauw configuration. In order to facilitate the discussion, samples with a conducting interface will henceforth be designated with the suffix "C", insulating samples will be labeled "I".

6.3 Results

Three $LaAlO_3/SrTiO_3$ heterostructures were grown under two different growth conditions and on two kind of substrates. The first sample (S1-C) was grown with an optimal fluence of 2 J/cm^2 on a TiO_2-terminated $SrTiO_3$-substrate, the second sample (S2-I) was grown with a much lower fluence by defocusing the PLD laser on the same TiO_2-terminated substrate, and the third sample (S3-I) was grown with

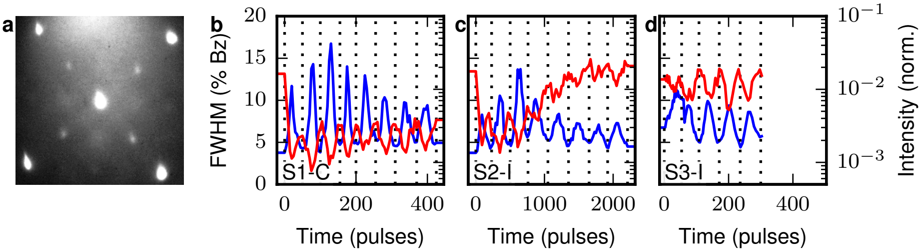

FIGURE 6.1: a) Diffraction pattern on bare $SrTiO_3$ at a growth temperature of 820 °C taken at 17 eV. b) FWHM (blue) and maximum intensity (red) of the specular diffraction spot for a conducting sample S1-C. c) Same for the insulating sample S2-I and d) same for the insulating sample S3-I. All data have been taken at 17 eV landing energy. The FWHM is given in percentage of the Brillouin zone, which is equal to the percentage of the distance from specular to the first order spots. The intensity has been normalized at the mirror mode (zero landing energy) intensity.

the optimal fluence of 2 J/cm^2 on the SrO-terminated $SrTiO_3$-substrate. For layer-by-layer growth control we took low-energy electron diffraction images as shown in fig. 6.1a for bare $SrTiO_3$. From the diffraction images, the peak intensity and full-width-half-maximum (FWHM) of the specular spot were recorded and are shown in fig. 6.1b, c, d in red and blue respectively for samples S1-C, S2-I and S3-I.

Clear oscillations can be observed in both FWHM and peak intensity, which are out of phase with one another. The landing energy of the electrons (17 eV) has been optimized for maximal contrast in the oscillations. This energy is close to the out-of-phase conditions where the electrons destructively interfere at the step edges on the surface. The oscillations can be understood by comparing a flat and rough surface. At the flat surface, typical for a fully grown unit cell layer, the electron constructively interfere along the out-of-plane axis of the crystal, resulting in a sharp diffraction spot (i.e. high peak intensity and small FWHM). On the other hand, at the rough surface (i.e. at n + 1/2 unit cell grown) the electrons interfere destructively at the new grown islands and scatter around, resulting in a broad diffraction peak (i.e. low peak intensity and high FWHM). As a guide to the eye, dotted lines are plotted to indicate integer number of unit cells grown. A total of eight unit cells was grown on S1-C, S2-I and five unit cells on S3-I. Much more pulses were needed for sample S2-I (Fig. 6.1c) than sample S1-C and S3-I (Fig. 6.1b, d). From this we can conclude that the growth speed is highly reduced for the out-of-focus laser beam, as expected.

For sample S1-C (Fig. 6.1b) the peak intensity strongly decreases at the start to oscillate around a constant background for the remainder of the time. Sample S2-I shows the same decrease but the background increases back to the starting value between three and five unit cells. Finally sample S3-I does not show the decrease at the start and keeps oscillating around a constant value. This change in background intensity is related to the electronic structure of the surface layer as we

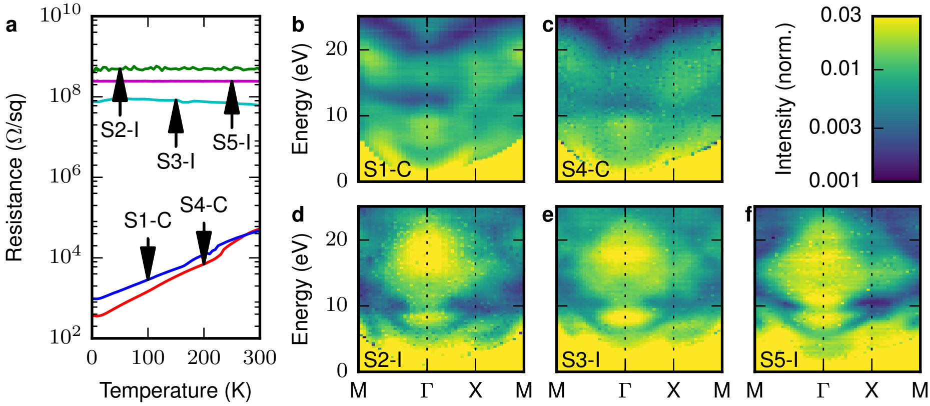

FIGURE 6.2: a) Sheet resistance versus temperature for five different samples. b-f) ARRES measurements for conducting (S1-C, S4-C) and non-conducting (S2-I, S3-I, S5-I) samples. Sample S1-C (b, blue) 8 u.c. $LaAlO_3$ grown in the LEEM, sample S4-C (c, red) 4 u.c. $LaAlO_3$ grown in a conventional PLD setup, sample S2-I (d, green) 8 u.c. $LaAlO_3$ grown with out-of-focus PLD laser, sample S3-I (e, cyan) 5 u.c. $LaAlO_3$ grown on SrO-terminated $SrTiO_3$ and sample S5-I (f, magenta) 5 nm $LaAlO_3$ grown with sputter deposition.

will elaborate on below. First we will characterize the electrical properties of these samples. For this, the temperature dependence of the sheet resistance is measured. The result is shown in fig. 6.2a for sample S1-C (blue), sample S2-I (green) and sample S3-I (cyan). Sample S1-C shows conducting behavior while sample S2-I and sample S3-I are insulating.

To fingerprint the difference between conducting and insulating samples at the growth temperature, we use angle-resolved reflected electron spectroscopy (ARRES)[14] as shown in fig. 6.2. ARRES utilizes the fact that the electron reflectivity strongly depends on the electron landing energy E_0 and the in-plane momentum $k_{\|}$. In particular the electron reflection is low if the material has a band at the specific (E_0, $k_{\|}$) of the electron so that it can couple into the band. In contrast, when (E_0, $k_{\|}$) of the electron coincide with a band gap the electron reflectivity is high. Hence the ”reflected-electron” or ARRES map shows a fingerprint of the unoccupied band structure(1).

ARRES maps of sample S1-C, S2-I and S3-I are shown in fig. 6.2b, d and e respectively. These maps were measured directly after growth, at the growth temperature. The conducting sample S1-C (Fig. 6.2b) shows a band (minimum in intensity) around 14 eV at the Γ-point and a V-shaped band at the top of the figure above 20 eV, while the insulating samples S2-I and S3-I (Fig. 6.2d, and e) shows a maximum (i.e. a band gap) between 14 and 22 eV around the Γ-point. This clear and strong difference between a conducting and non-conducting samples raises the question if this correlation is general.

---

(1) Multiple scattering effects can influence the result.

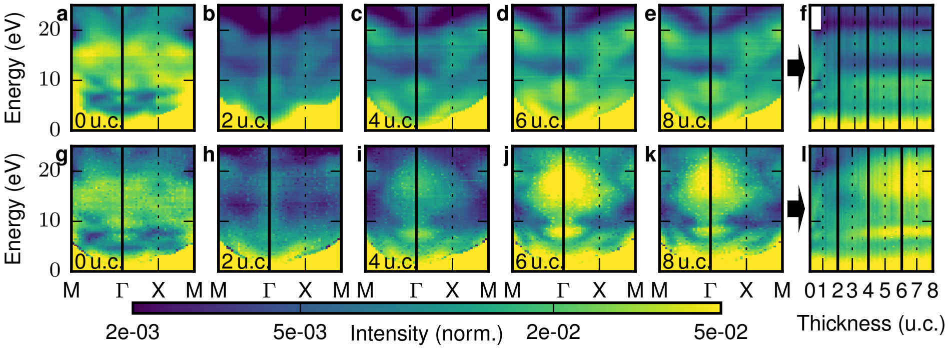

FIGURE 6.3: Conducting sample S1-C (top a-f) and non-conducting sample S2-I (bottom, g-l). From left to right ARRES maps for 0 (a, g), 2 (b, h), 4 (c, i), 6 (d, j) and 8 (e, k) unit cells respectively and an IV-curve versus thickness map (f, l). The black vertical lines at the Γ-point in the ARRES maps correspond with the black vertical lines in the IV-curve map including left and right edge. All images have the same color intensity.

For this we compare our samples with two more samples grown in other systems which are known from literature to produce conducting and non-conducting samples. These samples are sample S4-C grown in a conventional PLD system with the possibility to grow under higher oxygen pressures and known to result in conducting samples; and sample S5-I grown by on-axis sputter deposition, known to result in insulating samples[6]. ARRES maps are shown in figure 6.2c and f for the sample S4-C and S5-I respectively. Their (non-)conductance is confirmed by electrical measurements (Fig. 6.2a). During the ARRES measurements, both samples were kept at a high temperature in an oxygen pressure of 5×10^{-5} mbar to remove any contaminants and prevent the surface from charging. Exact growth and measurement conditions can be found in the appendix. Comparing S1-C and S4-C we conclude the ARRES map is stable under ex-situ transfer and against heating. The insulating samples S2-I, S3-I and S5-I in the bottom row of fig. 6.2 are similar, independent of how they are made. Remarkably, we find a clear difference between conducting and non-conducting samples at the growth temperature. Due to surface charging we cannot measure at room temperature, but the ex-situ grown and transferred samples S4-C and S5-I show our electron reflectivity measurements are stable.

Until now we focused on samples exceeding the critical thickness of four unit cells, required for samples to show conductivity[2]. Next we consider the influence of the thickness on the electron reflectivity, by measuring changes in the ARRES map during growth. Fig. 6.3 shows ARRES maps at the growth temperature for every second unit cell grown. Conducting sample S1-C is shown at the top (Fig. 6.3a-e) and insulating sample S2-I at the bottom (Fig. 6.3g-k). Both samples start with a TiO_2-terminated $SrTiO_3$ surface (a, g), showing the same ARRES map only slightly different in brightness. The ARRES maps show a strong change as soon as two unit cells of $LaAlO_3$ are grown (b, h). However, the maps of the conducting sample S1-C (top, b) and insulating sample S2-I (bottom, h) still show many similarities. This changes at four unit cells of $LaAlO_3$. While for the conducting sample S1-C (Fig. 6.3c) the band around Γ at 14 eV becomes a little bit more pronounced compared to two unit cells, the non-conducting sample S2-I (Fig. 6.3i) strongly changes and develops a pronounced band gap around the Γ-point for energies between 14 and 22 eV, observed as a high-intensity area. Adding more $LaAlO_3$ up to 6 (Fig. 6.3d, j) and 8 (Fig. 6.3e, k) unit cells only leads to little changes, both for the conducting and the non-conducting samples.

To probe the changes during growth in more detail we focus on the electron reflectivity at the Γ-point ($k_{\|} = 0$). This is nothing else than a LEEM (or LEED) IV-curve, which is the intensity variation of a diffracted beam, in this case the specular beam, as function of electron energy. Such curves are indicated with a vertical black line in the ARRES maps in fig. 6.3. These curves were taken during growth at regular intervals of 8 to 10 times per unit-cell. Results are shown in fig. 6.3f and l (sample S1-C top (f) and sample S2-I bottom (l)). They show the gradual change from the $SrTiO_3$ fingerprint to the final IV-curve of the $SrTiO_3/LaAlO_3$ heterostructure. The five black vertical lines (including the edges) correspond to the vertical black lines at the Γ-point in the five ARRES maps on the left side of fig. 6.3.

The IV-curve map fig. 6.3f shows that the band at 14 eV in sample S1-C appears just after two unit cells have been grown. The band around 21 eV has already appeared at this thickness. The non-conducting sample S2-I (Fig. 6.3l) shows both bands around two unit cells, but they vanish between three and four unit cells when the band gap appears between 14 and 22 eV. The band gap at 8 eV also clearly appears at this thickness.

A zoomed-in part of the IV-curve maps in figure 6.3f and l, for zero to five unit cells, is shown in figure 6.4a and b together with an IV-curve map of sample S3-I with $LaAlO_3$ on SrO-terminated $SrTiO_3$ (Fig. 6.4c), the substrate prepared in a different PLD system. For comparison, the IV-curves after deposition of 0, 2 and 5 unit cells of $LaAlO_3$ are plotted in figure 6.4d, e and f. Here the IV-curves from sample S1-C (Fig. 6.4a) are plotted in blue, sample S2-I (Fig. 6.4b) in green and sample S3-I (Fig. 6.4c) in red. These plots show clearly two distinct starting (0 u.c.) IV-curves and two distinct IV-curves after deposition of 5 u.c. of $LaAlO_3$. The starting IV-curves correspond with the TiO_2- (blue, green) and SrO-terminated (red) $SrTiO_3$ while in the IV-curves after deposition we distinguish the conducting (blue) and non-conducting (green, red) samples.

The transition from the starting to the after-growth curve is different for the two insulating samples. This is very clear around two unit cells where sample S2-I (green) is still close to sample S1-C (blue) and not to sample S3-I (red), which is already close to the insulating final IV-fingerprint found on the non-conducting samples. As a matter of fact, the IV-curves for S3-I hardly change during growth on the SrO-terminated surface.

With these results, we can return to figure 6.1, where for sample S1-C (Fig 6.1b)

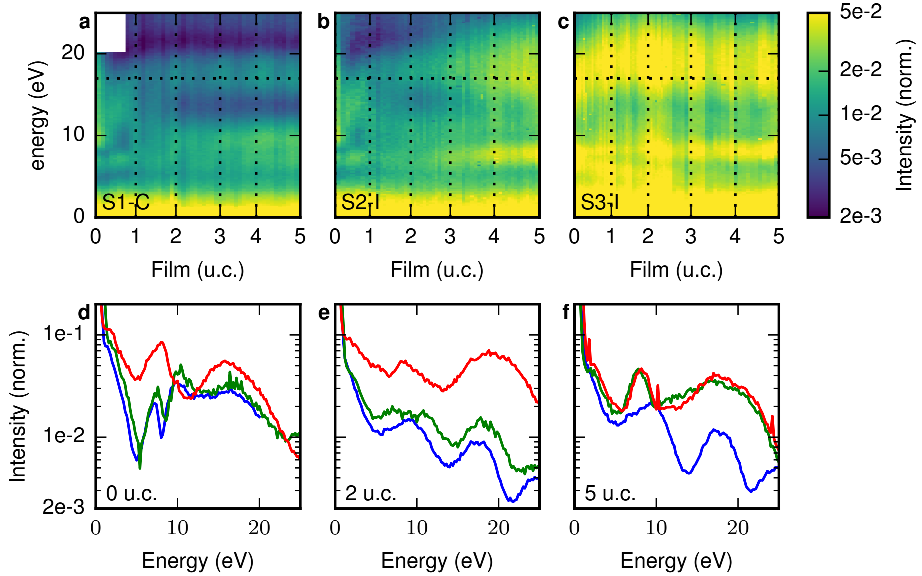

FIGURE 6.4: IV-curve versus thickness maps for sample S1-C (a), sample S2-I (b) and sample S3-I (c). d, e, f) IV-curves after deposition of 0, 2 and 5 unit cells of $LaAlO_3$, respectively, for sample S1-C (blue), sample S2-I (green) and sample S3-I (red). Horizontal dotted lines in a,b and c indicate the energy where fig. 6.1 is measured. IV-curves are obtained by the integrated intensity of the specular diffraction spot, filtering out any influence of the surface roughness.

the intensity strongly decreased at the start and continued to oscillate around a low value; for sample S2-I (Fig 6.1c) the intensity decreased at the start, but recovered between three and five unit cells; and for sample S3-I (Fig 6.1d) the intensity oscillated around the start value, and did not decrease at all. The energy of 17 eV where the data of fig. 6.1 was taken is indicated with a horizontal dotted line in the IV-curve maps, fig. 6.4a, b and c. Note that in fig. 6.1 the maximum of the specular diffraction spot is plotted, which is sensitive to spot broadening due to surface roughening. This results in growth oscillations superimposed on the electron reflectivity signal. On the other hand, for fig. 6.4 the intensity of the total specular spot is integrated, resulting in an intensity independent of spot shape (i.e. surface roughness) and only depending on the electron reflectivity. Combining fig. 6.1 and 6.4 we can now conclude that the increasing background signal between three and four unit cells in fig. 6.1c is caused by the appearance of the band gap shown in fig. 6.4b.

One question which may be raised with respect to the out-of-focus grown sample is whether the epitaxy is impaired by the ill-defined fluence. For that we performed a scanning transmission electron microscopy (STEM) experiment with high-angle annular dark-field imaging (HAADF) on sample S6-I, grown under the

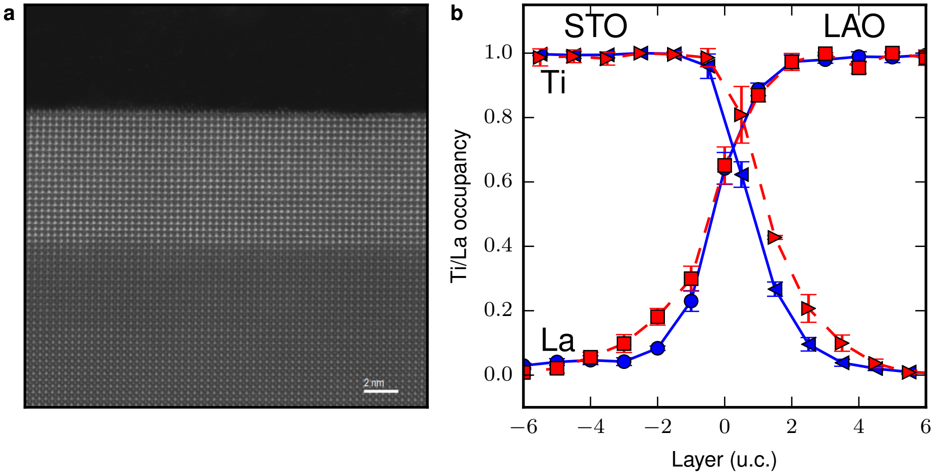

FIGURE 6.5: a) STEM-HAADF image of sample S6-I grown under same circumstances as S2-I, but with 20 unit cells of $LaAlO_3$. A slight misorientation between film and substrate can be observed. b) Normalized Ti- (◁, ▷) and La-occupancy (○, □) for S7-C, (blue, solid line, ○ and ◁) and S6-I (red, dashed line, □ and ▷). Sample S7-C has been grown under same conditions as S4-C. (experiment by N. Gauquelin, Antwerp)

same conditions as the out-of-focus sample S2-I, but with 20 unit cells $LaAlO_3$. The experiment also yields the concentration variation of the various elements when going through the interface. The results are shown in figure 6.5. Besides a slight misorientation, nice epitaxial growth can be observed. Figure 6.5b shows the Ti- and La-occupancy normalized to the total A- and B-site occupancy for the samples S6-I and S7-C. The sample S7-C is grown under comparable conditions as sample S4-C. Ti-diffusion into the $LaAlO_3$ can be observed for the out-of-focus sample S6-I, compared to the conducting sample S7-C.

6.4 Discussion

Even after many years of research, the outstanding question with respect to understanding the conductivity of the $SrTiO_3/LaAlO_3$ interface still is whether that is due to the electronic reconstruction of a basically perfect interface, or that defect generation in the $SrTiO_3$ is an essential ingredient. Secondary questions then exist about the role of intermixing, oxygen vacancies, the strain gradients and the ensuing buckling of the oxygen octahedra at the interface, or the stoichiometry of the $LaAlO_3$ layer. Central to the discussion are the two observations that conductance only occurs after growth on the TiO_2-terminated surface, not on the SrO-termination; and that 4 unit cells of $LaAlO_3$ are required to generate conductance. Especially the latter fact is often used to argue electronic reconstruction: the potential build-up in the polar $LaAlO_3$ is countered by charge transfer to the interface after reaching a critical thickness. On the other hand, the importance of defects is supported by the observation of the influence of oxygen[7] and La/Al-stoichiometry[4–6] on the conductance.

The discussion on the La/Al-stoichiometry has started relatively recently. It has been found that the $LaAlO_3$ film has to be Al-rich for conductance to appear[4,5] and also that the $LaAlO_3$ stoichiometry is strongly dependent on the PLD parameters[22]. We will now argue that our electron reflectivity experiments precisely address the issue of (non-)stoichiometry and defects, which are crucial for the occurrence of interface conductivity. Our observations are that (i) the difference between C- and I-samples is already apparent during growth and at the growth temperature and (ii) the differences between C- and I-samples are significant on the scale of eVs. The conclusion we draw from this is that the (electronic) structure of the $LaAlO_3$ surface layer which is the one we are most sensitive to, is different for C-samples and for I-samples. The sensitivity of the electron reflectivity to the surface layer can be concluded from the strong change in IV-curve seen in figure 6.4d between TiO_2-terminated and SrO-terminated $SrTiO_3$. We note that the sensitivity depends on the penetration depth, which is energy dependent. Unfortunately, we cannot compare our data to calculations of the electron reflectivity, or the empty band structure of different possible surfaces. We can however sketch a scenario which can be contemplated for such calculations.

The scenario is as follows. We note that the $LaAlO_3$ grown on TiO_2-terminated $SrTiO_3$ should be AlO_2-terminated, while the $LaAlO_3$ grown on SrO-terminated $SrTiO_3$ should be LaO-terminated. We surmise that this difference in termination causes the strong difference between the conducting sample S1-C and the non-conducting sample S3-I. The most intriguing sample is S2-I, which shows an IV-curve comparable to sample S1-C (AlO_2-terminated) for two unit cells (Fig. 6.4e) and changes to the signature of sample S3-I (LaO-terminated) for five unit cells (Fig. 6.4f). In contrast to the other samples, sample S2-I was grown with an out-of-focus laser. As stated before, from literature we know that changing the PLD parameters, in particular the fluence, changes the stoichiometry of the grown film. Furthermore, we know that Al-rich $LaAlO_3$ results in a conducting interface and La-rich $LaAlO_3$ in an insulating interface. From this we infer sample S2-I with out-of-focus laser is La-rich. This together with the growth on TiO_2-terminated $SrTiO_3$ suggests the following. We start with the growth on TiO_2-terminated $SrTiO_3$ resulting in a AlO_2-termination, as seen after growth of two unit cells. Growing further the La-excess slowly builds up, changing the surface to LaO-rich. We further note that the Ti-intermixing into the $LaAlO_3$ found for sample S2-I could compensate the Al-deficits in the first unit cells, suppressing the effects of the La-excess in the first two unit cells.

Here we should remark that DFT calculations in Ref. 23 showed that the surface is not AlO_2- or LaO-terminated, but rather that $Al_{3/2}O_2$ and $La_{5/6}O$ are the stable surface terminations. This implies that the AlO_2 surfaces mentioned above are actually $Al_{3/2}O_2$ and the LaO surface are $La_{5/6}O$, which does not conflict with our results. On the contrary, the fact that less La is required for the $La_{5/6}O$ and more Al for the $Al_{3/2}O_2$ surface could stimulate the transition from a $Al_{3/2}O_2$ to a $La_{5/6}O$ surface for our La-rich sample S2-I. In any case, the La-enrichment at the surface appears to be stronger than concluded in Ref. 23, which would certainly influence charge transfer to the interface.

Summarizing, we find that the strong change in electron reflectivity, which is correlated to the unoccupied band structure, depends on the surface termination. From the importance of the surface for the interface conductivity as described in literature[24,25] and our findings deduce that the excess La on the surface could be an essential step in suppressing the electron transfer to the interface. More research has to be done to investigate what exactly happens here.

Finally, we note that our La-rich and Al-rich surface signatures do not correspond with the IV-curves measured on bulk mixed ordered terminated $LaAlO_3$ measured in chapter 4. This can however be explained by the surface reconstructions found on the bulk $LaAlO_3$ and the difference between bulk and strained thin films.

6.5 Summary

We have shown results of electron reflectivity experiments (ARRES) on conducting and insulating $LaAlO_3/SrTiO_3$-heterostructures during growth, at the growth temperature with sub-unit cell precision. We find distinct signatures for the conducting and non-conducting samples independent of their growth conditions. In other words, the electron reflectivity (ARRES) can predict during growth whether a sample will be able to show conductivity.

We find that the two families of reflectivity curves (maps) can be assigned to the surface termination being either AlO_2 or LaO-rich. For samples with Al-rich $LaAlO_3$ the surface termination is directly couples to the termination of the $SrTiO_3$. A SrO-termination results in a LaO-rich surface, while a TiO_2-termination results in an AlO_2-rich surface. For the growth of La-rich $LaAlO_3$, which we believe we achieve by out-of-focus laser growth, we find the surface termination slowly changes from AlO_2-rich to LaO-rich during growth. From the importance of the surface for the interface conductivity as described in literature[24,25], we infer that it could be this change in surface termination that is essential in suppressing the interface conductivity for the La-rich growth.

6.6 Appendix

Five samples have been grown for LEEM analysis. The PLD and sputter growth parameters of this films are shown in table 6.1 together with the temperature where the ARRES maps are measured.

Sample Nr.	Fluence J/cm^2	Growth °C	Termination	Pressure mbar	Measure °C
S1-C	2	780	TiO_2	5×10^{-5}	795
S4-C	1	720	TiO_2	$1{\times}10^{-4}$	630
S2-I		770	TiO_2	5×10^{-5}	770
S3-I	2	700	SrO	5×10^{-5}	600
S5-I	na	830	TiO_2	$3{\times}10^{0}$	560

TABLE 6.1: PLD and sputter growth conditions for samples analyzed in LEEM as well as the temperature where the ARRES maps were taken.

References

[1] A. Ohtomo and H. Y. Hwang, *A high-mobility electron gas at the $LaAlO_3/SrTiO_3$ heterointerface*, Nature **427**, 423 (2004).

[2] S. Thiel, G. Hammerl, A. Schmehl, C. W. Schneider, and J. Mannhart, *Tunable Quasi-Two-Dimensional Electron Gases in Oxide Heterostructures*, Science **313**, 1942 (2006).

[3] L. Zhang, X.-F. Zhou, H.-T. Wang, J.-J. Xu, J. Li, E. G. Wang, and S.-H. Wei, *Origin of insulating behavior of the p-type $LaAlO_3/SrTiO_3$ interface: Polarization-induced asymmetric distribution of oxygen vacancies*, Physical Review B **82**, 125412 (2010).

[4] M. P. Warusawithana, C. Richter, J. A. Mundy, P. Roy, J. Ludwig, S. Paetel, T. Heeg, A. A. Pawlicki, L. F. Kourkoutis, M. Zheng, M. Lee, B. Mulcahy, W. Zander, Y. Zhu, J. Schubert, J. N. Eckstein, D. A. Muller, C. S. Hellberg, J. Mannhart, and D. G. Schlom, *$LaAlO_3$ stoichiometry is key to electron liquid formation at $LaAlO_3/SrTiO_3$ interfaces*, Nature Communications **4** (2013).

[5] E. Breckenfeld, N. Bronn, J. Karthik, A. R. Damodaran, S. Lee, N. Mason, and L. W. Martin, *Effect of Growth Induced (Non)Stoichiometry on Interfacial Conductance in* $LaAlO_3/SrTiO_3$, Physical Review Letters **110**, 196804 (2013).

[6] I. M. Dildar, D. B. Boltje, M. H. S. Hesselberth, J. Aarts, Q. Xu, H. W. Zandbergen, and S. Harkema, *Non-conducting interfaces of $LaAlO_3/SrTiO_3$ produced in sputter deposition: The role of stoichiometry*, Applied Physics Letters **102**, 121601 (2013).

[7] A. Brinkman, M. Huijben, M. van Zalk, J. Huijben, U. Zeitler, J. C. Maan, W. G. van der Wiel, G. Rijnders, D. H. A. Blank, and H. Hilgenkamp, *Magnetic effects at the interface between non-magnetic oxides*, Nature Materials **6**, 493 (2007).

[8] Ariando, X. Wang, G. Baskaran, Z. Q. Liu, J. Huijben, J. B. Yi, A. Annadi, A. R. Barman, A. Rusydi, S. Dhar, Y. P. Feng, J. Ding, H. Hilgenkamp, and T. Venkatesan, *Electronic phase separation at the $LaAlO_3/SrTiO_3$ interface*, Nature Communications **2**, 188 (2011).

[9] D. A. Dikin, M. Mehta, C. W. Bark, C. M. Folkman, C. B. Eom, and V. Chandrasekhar, *Coexistence of Superconductivity and Ferromagnetism in Two Dimensions*, Physical Review Letters **107**, 056802 (2011).

[10] J. A. Bert, B. Kalisky, C. Bell, M. Kim, Y. Hikita, H. Y. Hwang, and K. A. Moler, *Direct imaging of the coexistence of ferromagnetism and superconductivity at the $LaAlO_3/SrTiO_3$ interface*, Nature Physics **7**, 767 (2011).

[11] N. Reyren, S. Thiel, A. D. Caviglia, L. F. Kourkoutis, G. Hammerl, C. Richter, C. W. Schneider, T. Kopp, A.-S. Ruetschi, D. Jaccard, M. Gabay, D. A. Muller, J.-M. Triscone, and J. Mannhart, *Superconducting Interfaces Between Insulating Oxides*, Science **317**, 1196 (2007).

[12] A. Joshua, S. Pecker, J. Ruhman, E. Altman, and S. Ilani, *A universal critical density underlying the physics of electrons at the* $LaAlO_3/SrTiO_3$ *interface*, Nature Communications **3**, 1129 (2012).

[13] A. D. Caviglia, S. Gariglio, N. Reyren, D. Jaccard, T. Schneider, M. Gabay, S. Thiel, G. Hammerl, J. Mannhart, and J.-M. Triscone, *Electric field control of the* $LaAlO_3/SrTiO_3$ *interface ground state*, Nature **456**, 624 (2008).

[14] J. Jobst, J. Kautz, D. Geelen, R. M. Tromp, and S. J. van der Molen, *Nanoscale measurements of unoccupied band dispersion in few-layer graphene*, Nature Communications **6**, 8926 (2015).

[15] R. Tromp, J. Hannon, A. Ellis, W. Wan, A. Berghaus, and O. Schaff, *A new aberration-corrected, energy-filtered LEEM/PEEM instrument. I. Principles and design*, Ultramicroscopy **110**, 852 (2010).

[16] S. M. Schramm, J. Kautz, A. Berghaus, O. Schaff, R. M. Tromp, and S. J. van der Molen, *Low-energy electron microscopy and spectroscopy with ESCHER: Status and prospects*, IBM Journal of Research and Development **55**, 1:1 (2011).

[17] S. M. Schramm, A. B. Pang, M. S. Altman, and R. M. Tromp, *A Contrast Transfer Function approach for image calculations in standard and aberration-corrected LEEM and PEEM*, Ultramicroscopy **115**, 88 (2012).

[18] R. Tromp, J. Hannon, W. Wan, A. Berghaus, and O. Schaff, *A new aberration-corrected, energy-filtered LEEM/PEEM instrument II. Operation and results*, Ultramicroscopy (2013).

[19] M. B. S. Hesselberth, S. J. v. d. Molen, and J. Aarts, *The surface structure of* $SrTiO_3$ *at high temperatures under influence of oxygen*, Applied Physics Letters **104**, 051609 (2014).

[20] A. J. H. van der Torren, S. J. van der Molen, and J. Aarts, *Formation of a mixed ordered termination on the surface of* $\mathrm{LaAlO_3}$(001), Physical Review B **91**, 245426 (2015).

[21] M. Kawasaki, K. Takahashi, T. Maeda, R. Tsuchiya, M. Shinohara, O. Ishiyama, T. Yonezawa, M. Yoshimoto, and H. Koinuma, *Atomic Control of the* $SrTiO_3$ *Crystal Surface*, Science **266**, 1540 (1994).

[22] E. Breckenfeld, R. Wilson, J. Karthik, A. R. Damodaran, D. G. Cahill, and L. W. Martin, *Effect of Growth Induced (Non)Stoichiometry on the Structure, Dielectric Response, and Thermal Conductivity of* $SrTiO_3$ *Thin Films*, Chemistry of Materials **24**, 331 (2012).

[23] C. Weiland, G. E. Sterbinsky, A. K. Rumaiz, C. S. Hellberg, J. C. Woicik, S. Zhu, and D. G. Schlom, *Stoichiometry dependence of potential screening at* $La_{(1-\delta)}Al_{(1+\delta)}O_3/SrTiO_3$ *interfaces*, Physical Review B **91**, 165103 (2015).

[24] Y. Xie, C. Bell, T. Yajima, Y. Hikita, and H. Y. Hwang, *Charge Writing at the* $LaAlO_3/SrTiO_3$ *Surface*, Nano Letters **10**, 2588 (2010).

[25] R. Pentcheva, R. Arras, K. Otte, V. G. Ruiz, and W. E. Pickett, *Termination control of electronic phases in oxide thin films and interfaces:* $LaAlO_3/SrTiO_3$*(001)*, Philosophical Transactions of the Royal Society A: Mathematical, Physical and Engineering Sciences **370**, 4904 (2012).

7

Growing a $LaAlO_3$/$SrTiO_3$ heterostructure on $Ca_2Nb_3O_{10}$ nanosheets

The two-dimensional electron gas between the band insulators $LaAlO_3$ and $SrTiO_3$ is a promising component for oxide eletronics, but the requirement of single crystal substrates for the growth limits its applications. It is therefore important to find ways to deposit these materials on other substrates. Interesting candidates are nanosheets of $Ca_2Nb_3O_{10}$ which can be used as seed layers for perovskite materials on any substrate. These nanosheets can reach a lateral size of several microns. Low-energy electron microscopy with in-situ *pulsed laser deposition allows us to study the growth on these flakes as well as to fingerprint the electronic properties. We grow a $LaAlO_3$/$SrTiO_3$ heterostructure on $Ca_2Nb_3O_{10}$ nanosheets deposited on a Si substrate and find that it shows the fingerprints of a two-dimensional electron gas.*

This chapter will be submitted as:

A.J.H. van der Torren, H. Yuan, J. Jobst, J.E. ten Elshof, M. Huijben, A.J.H.M. Rijnders, G. Koster, S.J. van der Molen, J. Aarts, *Growing a* $LaAlO_3/SrTiO_3$ *heterostructure on* $Ca_2Nb_3O_{10}$ *nanosheets*

7.1 Introduction

Transition metal oxides (TMO's) and especially the group with the perovskite crystal structure is an interesting group of materials with a great varity of physical properties. Moreover, stacking layers of different metal oxides allows for new properties to be made on design. A well known example is the formation of the two-dimensional electron gas (2-DEG) between $SrTiO_3$ and $LaAlO_3$[1].

Typically, these materials are grown on single crystals, which is impractical for industrial applications. This limitation can be overcome by growing $SrTiO_3$ on a simpler substrate. Growth on Si is possible[2], but here we use a different approach and use inorganic nanosheets. Such sheets can be obtained through exfoliation of materials which allow a close match with the lattice parameter of the deposited $SrTiO_3$ layer. In our case that is $Ca_2Nb_3O_{10}$ on which the growth of epitaxial $SrTiO_3$, $SrRuO_3$ and $BiFeO_3$ has already been shown[3]. This nanosheet approach is very flexible, as nanosheets can be deposited on virtually any substrate[3–6], rendering design freedom in tailoring device properties.

Compared to the conventional case where the $LaAlO_3/SrTiO_3$ 2-DEG resides on top of half a millimeter thick $SrTiO_3$ substrate, the exfoliated nanosheets have a thickness of only 1.5 to 4 nm[6–9]. This allows to dramatically reduce the thickness of the $SrTiO_3$ dielectric, which is particularly useful if that is to be used as a backgate.

To make optimal use of this advantage, it is important to understand the formation of the 2-DEG in the limit of a minimal thickness of the $LaAlO_3/SrTiO_3$ grown on the nanosheets. Low-energy electron microscopy (LEEM) with *in-situ* pulsed laser deposition (PLD) is the ideal tool to study the growth and electronic properties of these heterostructures in a laterally resolved manner[10]; as already discussed in chapter 5.

In this chapter we show the growth of $LaAlO_3/SrTiO_3$ heterostructures on $Ca_2Nb_3O_{10}$ nanosheets which have been deposited on a Si substrate. We use a combined LEEM/PLD system to study the details of the growth in real time and to investigate the electronic structure of the material we grow. We compare the results obtained on nanosheets with conventional $LaAlO_3/SrTiO_3$ heterostructures on a $SrTiO_3$ substrate to judge the quality of the heterostructure.

7.2 Experimental

$Ca_2Nb_3O_{10}$ nanosheets where synthesized and deposited by Langmuir-Blodgett (LB) deposition on insulating Si substrates as described elsewhere[6]. The samples were first transferred into the ESCHER LEEM system[10–13] with *in-situ* pulsed laser deposition as described in chapter 5. Before starting the growth, they were annealed at 570 °C (measured with a pyrometer using an emissivity of 0.7) for at least half an hour in an oxygen background pressure of 5×10^{-5} mbar, in order to remove any contaminants.

A home-built PLD system was used to grow the materials *in-situ*. In fact, PLD growth and LEEM imaging is performed in an alternating fashion: the high voltage between objective lens and sample, which is required to decelerate the low-energy electrons for imaging, is turned off during the deposition performed by 5 to 10 laser pulses, depending on the material growth speed. After that the high voltage is quickly ramped up again to image the sample. These cycles of roughly 3 min each are repeated until a film of the desired thickness is grown. During the process, temperature and pressure are kept constant.

For the deposition of $SrTiO_3$ onto the nanosheets, the temperature was raised to 660 °C. PLD was performed with a laser fluence of 1.4 J/cm^2 and a 1 Hz repetition rate in 5×10^{-5} mbar oxygen. In chapter 5 it was discussed that these parameters for the growth of $SrTiO_3$ can result in slightly off-stoichiometric growth. However, it was not possible to further optimize the growth at the low pressures our microscope is limited to. Following the deposition, the sample was annealed at 770 °C for at least half an hour in the same oxygen pressure, in order to improve the surface flatness. The sample was then cooled down and moved to the transfer chamber (2×10^{-9} mbar) while the $SrTiO_3$-target was replaced with a $LaAlO_3$-target. After a pre-ablation step of the $LaAlO_3$-target, the sample was transferred back to the measurement position. It was heated to 750 °C at the same oxygen pressure of 5×10^{-5} mbar. $LaAlO_3$ was then deposited at a laser fluence of 2.0 J/cm^2 and 1 Hz repetition rate. In chapter 6 it was shown that these parameters result in a conducting $LaAlO_3/SrTiO_3$ interface. Three samples were made, called A to C, with $SrTiO_3$ thicknesses estimated to be 3.4 nm, 5.6 nm and 5.5 nm, respectively. For comparison, $LaAlO_3$ was grown on a TiO_2-terminated[14] $SrTiO_3$-substrate under the same growth conditions (sample D).

The nanosheet starting material, the whole growth process and the final heterostructures were investigated by various techniques available in the LEEM. LEEM provides real-space images while low-energy electron diffraction (LEED) is used to study the crystal structure. The ability to quickly switch between real-space imaging and diffraction in combination with µLEED (confining the probing electron beam to sub-micron size by putting an aperture in the beam path) allows for investigation of the crystal structure of the independent flakes. LEEM-IV spectra or IV-curves (the intensity of reflected electrons as a function of their landing energy) yield clear fingerprints of the different surface layers[15]. Angle-resolved reflected-electron spectroscopy (ARRES)[16] extends the concept of IV-curves by recording electron reflectivity maps as a function of landing energy and in-plane wave vector $k_\parallel$ of the electrons. Such ARRES maps are correlated with the unoccupied band structure of the surface layer and are therefore well suited to probe the surface stoichiometry of the $LaAlO_3$-layer. This implicitly indicates whether or not a 2-DEG is formed at the $LaAlO_3/SrTiO_3$ interface as was shown in chapter 6.

7.3 Results

Figure 7.1a shows a LEEM image of $Ca_2Nb_3O_{10}$ nanosheets deposited on Si (sample A). Individual nanosheets can clearly be recognized, of which the sheet covering the bottom half of the image is the biggest. In the top half, four medium size flakes

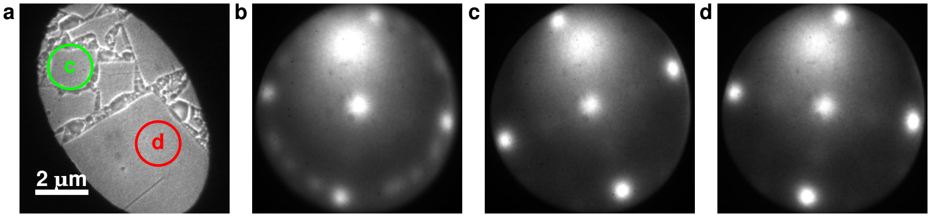

FIGURE 7.1: a) LEEM image of nanosheets on Si (sample A) with circles in red (lower right) and green (upper left) around the areas where images c and d are taken. b) Diffraction pattern taken on sample A. Note that apart from the four strong reflections there are numerous weak ones on the circle in between them. c) µLEED image of area indicated with the green circle (upper, left) in (b). d) µLEED pattern of area indicated with the red circle (lower, right). All diffraction patterns are taken at 14 eV landing energy. The real-space image is taken close to 0 eV landing energy.

can be recognized with some smaller ones in between. The square surface net expected for $Ca_2Nb_3O_{10}$ is visible in the LEED image (Fig. 7.1b) taken on the same area as fig. 7.1a. Besides the bright four spots originating from the big flake covering the bottom half of the image, many other rotated patterns are visible originating from the flakes in the top half of the image. This indicates that the individual nanosheets are rotated with respect to one another. The rotations of the individual flakes can be determined by taking µLEED images. Figure 7.1c,d show such µLEED patterns of the areas indicated with green (left, top) and red (right, bottom) circles in the LEEM image in Fig. 7.1a. Note that the diffraction spots are not very sharp. This could be caused by imperfect crystallinity of the nanosheets or absorbates at the surface[17].

After characterizing the starting material, we grew $SrTiO_3$ on the sheets by PLD. For the growth, the temperature was raised to 660 °C. Higher temperatures showed degradation of the diffraction pattern. Figure 7.2a and b show the evolution of the intensity and full-width-half-maximum (FWHM) of the specular (0,0) diffraction spot during the growth process for the whole range of energies between 0 and 25 eV. Basically, figure 7.2a shows a series of IV-curves for the specular beam. This reflected intensity is related to the unoccupied band structure (see discussion below) and therefore is a fingerprint of the material studied. During growth we observe a clear change of the IV-curves (vertical cuts through Fig. 7.2a) and therefore a change in the electronic fingerprint of the surface. The IV-curves converge to a constant spectrum around 300 pulses which consists of maxima around 3, 8 and 15 eV. A typical single IV-curve out of this collection will be given and discussed below.

The FWHM of the specular (0,0) diffraction spot (Fig. 7.2b) is sensitive to the crystallinity of the material as well as to the surface roughness. While a small coherence length in the crystal structure broadens the FWHM over all the energies,

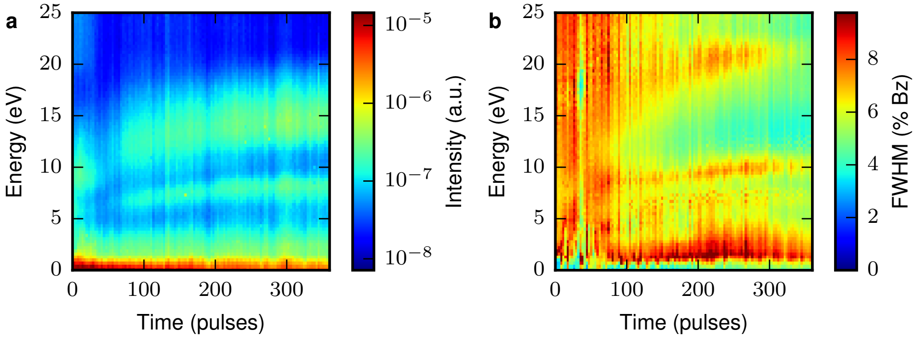

FIGURE 7.2: intensity (a) and FWHM (b) map of the specular (0,0) diffraction spot versus energy during deposition of $SrTiO_3$ on sample A. The intensity map shows a clear change in material, while the FHWM maps shows sharpening of the diffraction spots. Moreover the FWHM becomes energy dependent. The FWHM is given in percentage of the Brillouin zone size.

the surface roughness only influences the FWHM at energies where the incoming and reflected electrons destructively interfere along the out-of-plane axis of the crystal[17]. During growth, the diffraction spots became sharper, quantified by a global reduction of the FWHM (Fig. 7.2b). Moreover, the FWHM became energy-dependent. In other words, the crystallinity improved, but the surface was still rough.

Important, however, is that neither the intensity nor the FWHM showed oscillations during growth. Normally, in layer-by-layer growth of these perovskites a completed and flat layer shows high intensity and small FWHM, while a half-completed and rough layer shows a low intensity and large FWHM. This was demonstrated in chapters 5 and 6 for the growth of $SrTiO_3$ and $LaAlO_3$ on $SrTiO_3$. With respect to the intensity it is the same phenomena as is seen in reflection high energy electron diffraction (RHEED).

Such oscillations can hence be used to count the number of layers but, as noted, they were not visible. Instead, both intensity and FWHM are constant, and the FWHM is large. It is not clear whether that is caused by a small coherence length in the material or a non layer-by-layer growth mode with a constant rough surface. Comparing the growth conditions and amount of pulses to earlier measurements in chapter 6, we can however estimate a film thickness close to 9 unit cells. With this estimation the minimal thickness of 300 pulses is equal to about 7 unit cells.

Figure 7.3a shows a section of the specular (0,0) diffraction spot for the original nanosheets (blue, dashed) and nanosheets with $SrTiO_3$ (green, solid) taken at 17 eV. To compare their FWHM, both curves have been normalized, since the intensity on the nanosheets is 8 times smaller than on the $SrTiO_3$/nanosheet heterostructure. The FWHM has been reduced by about a factor two in growing $SrTiO_3$, indicating a factor 2 increase in the coherent size of the lattice. The in-

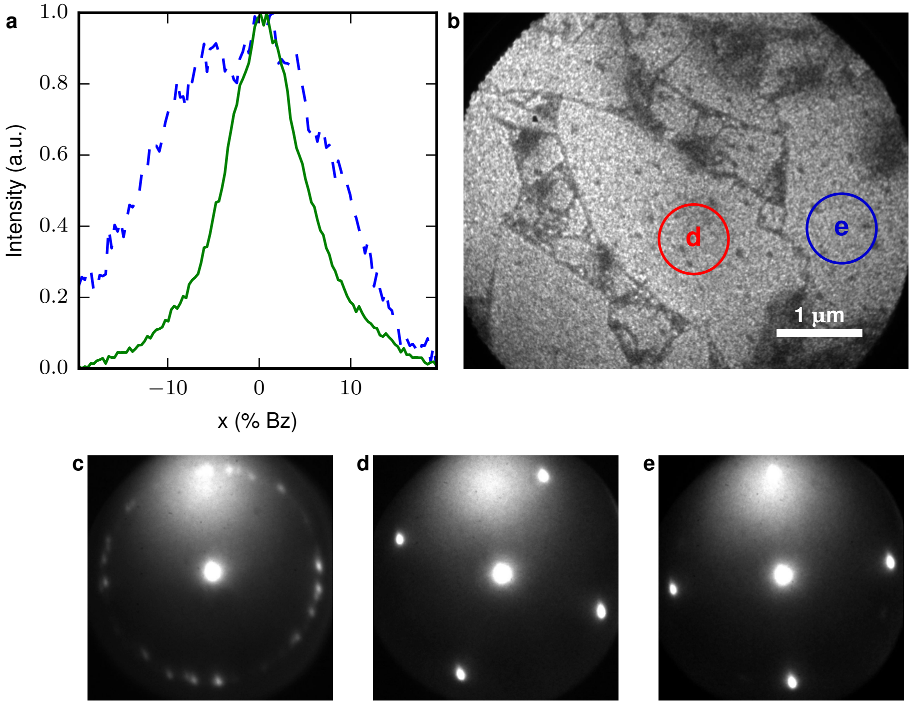

FIGURE 7.3: a) Normalized section of the specular (0,0) diffraction spot on nanosheets (blue, dashed) and after growth of $SrTiO_3$ (green, solid) on sample A taken at 17 eV. The intensity of the blue curves was 1/8 of that of the green curve. b) Bright field image at 29.6 eV with locations of µLEED images d and e indicated in red (left) and blue (right). c) LEED image of the area shown in b. d, e) µLEED image of areas indicated in b. All LEED/µLEED images were taken at 17 eV landing energy.

dividual nanosheets are still clearly visible in the bright field image (Fig. 7.3b), indicating that the STO only grew epitaxially on the sheets. Indeed, the black areas separating individual nanosheets did not show a diffraction pattern, i.e. the material there was not crystalline. Just as on the bare nanosheets, the LEED pattern in Fig.7.3c shows multiple diffraction patterns, while µLEED patterns in Fig. 7.3d and e show single orientations for every $SrTiO_3$/nanosheet heterostructure. These µLEED patterns were taken on the areas indicated with circles in red (left) and blue (right) in Fig. 7.2b, respectively. This suggests the $SrTiO_3$ follows the crystal structure of the underlying nanosheets.

Although the grown $SrTiO_3$ layer was crystalline after deposition, the FWHM of the specular spot was still broad compared to measurements on a single crystal $SrTiO_3$ substrate. To further improve the surface quality we annealed the sample with the following procedure: the sample was slowly heated from 660 °C to 770 °C

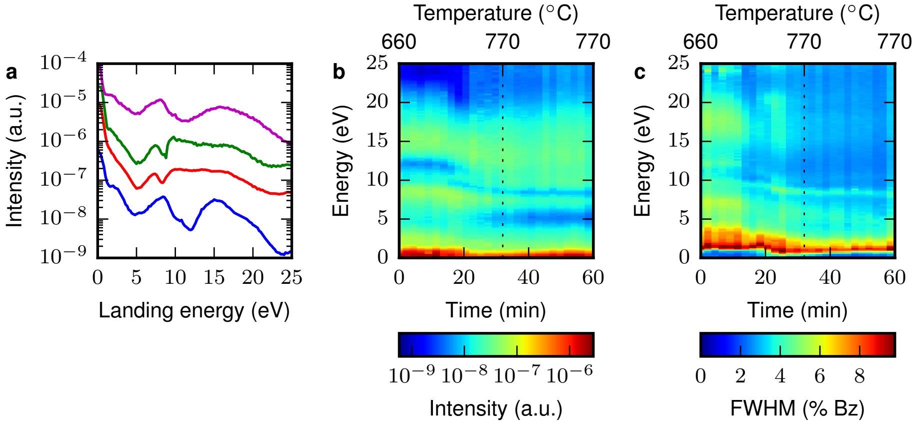

FIGURE 7.4: a) IV-curve before (blue, bottom) and after (red, 2nd from bottom) annealing. As comparison, two IV-curves on a $SrTiO_3$-substrate are shown, TiO_2-terminated (green, 2nd from top) and SrO-terminated (magenta, top). Curves are shifted for clarity. Intensity (b) and FWHM (c) versus energy during the annealing process on sample B. Over the first half an hour the temperature was slowly increased from 660 °C to 770 °C and was kept constant for the next half an hour. The dotted line separates the time the temperature was ramped and the time it was kept constant. The FWHM is given in percentage of Brillouin zone.

in 30 min and was held there for another 30 min. During the annealing the oxygen pressure was 5×10^{-5} mbar, equal to the pressure used during PLD. The maximum of 770 °C was the maximum temperature for which the diffraction pattern does not start to degrade.

The annealing not only changes the surface roughness but also the surface electronic properties. This is demonstrated in figure 7.4 taken on sample B ($SrTiO_3$ thickness of about 5.6 nm, i.e. 600 PLD pulses). Figure 7.4a shows four IV-curves, from bottom to top: sample B before annealing (blue), sample B after annealing (red), a reference curve taken on a TiO_2-terminated $SrTiO_3$-substrate (green) and a curve taken on a SrO-terminated $SrTiO_3$-substrate (magenta). The reference curves were taken from chapter 6 where the $SrTiO_3$ was TiO_2-terminated by HF-etching[14] and the SrO-termination was obtained by the growth of an SrO bilayer on a TiO_2-terminated substrate. From the IV-curves before and after annealing we can conclude the surface changes from a dominantly SrO-termination to a TiO_2-termination.

The material evolution is shown in more detail in figure 7.4b, which shows the IV-curve change over time during annealing, and figure 7.4c which shows the corresponding change of the FWHM. The FWHM further decreased and the energy dependence disappeared, i.e. the surface flattened. From the FWHM and intensity together we conclude that the change of the material and the flattening of the surface go hand in hand.

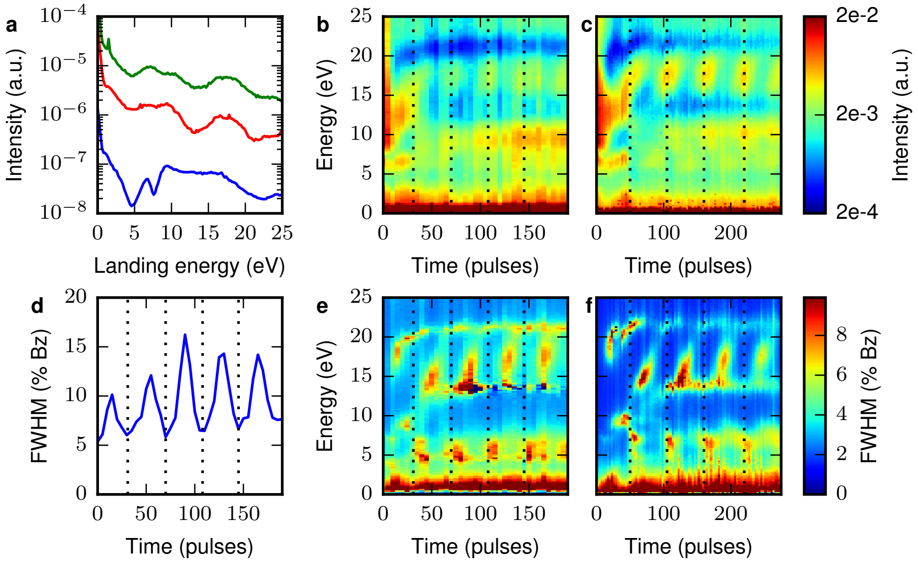

FIGURE 7.5: a) IV-curve before (blue, bottom) and after (red, middle) growth of $LaAlO_3$ on sample C. Furthermore, a reference curve of 5 unit cells $LaAlO_3$ on a $SrTiO_3$ substrate on sample$\tilde{D}$ (green, top) is shown. b) Intensity map versus time and energy of the specular (0,0) diffraction spot on sample C. c) the same map on reference sample D. d) FWHM oscillations versus time at 16 eV, on sample C. This energy is close to the out-of-phase conditions where maximal surface sensitivity is reached. e) FWHM map for all energies on sample C and f) FWHM map on sample D.

After improving the $SrTiO_3$ surface in this way and confirming it is TiO_2-terminated, a thin film of $LaAlO_3$ was grown. Figure 7.5a shows the IV-curves before (blue, bottom) and after (red, middle) growth on sample C ($SrTiO_3$ thickness of about 5.5 nm, i.e. 588 PLD pulses). Furthermore, a reference curve of 5 unit cells $LaAlO_3$ grown under the same conditions on a $SrTiO_3$-substrate (sample D) (green, top) is shown. The IV-curves after growth on the nanosheets and on the $SrTiO_3$-substrate are very similar, confirming that the same quality $LaAlO_3$ was grown in both cases. The evolution of the IV-curves during growth is shown in figure 7.5b for sample C and in figure 7.5c for the reference sample D. The same structure is found for both samples, i.e. they show the same type of growth. Both samples show oscillations in intensity around 16 eV, indicating layer-by-layer growth. As a guide to the eye, vertical dotted lines indicate the full unit cells. These growth oscillations are more clear from the FWHM at 16 eV, which is plotted for the nanosheet sample in figure 7.5d. This energy is close to the interference condition with the out-of-plane crystal axis. The FWHM for all energies from 0 to 25 eV is shown in figure 7.5e and f for the nanosheet sample C and the reference sample D. Here again we observe the same growth pattern for $LaAlO_3$ grown on the $SrTiO_3$/nanosheet heterostructure

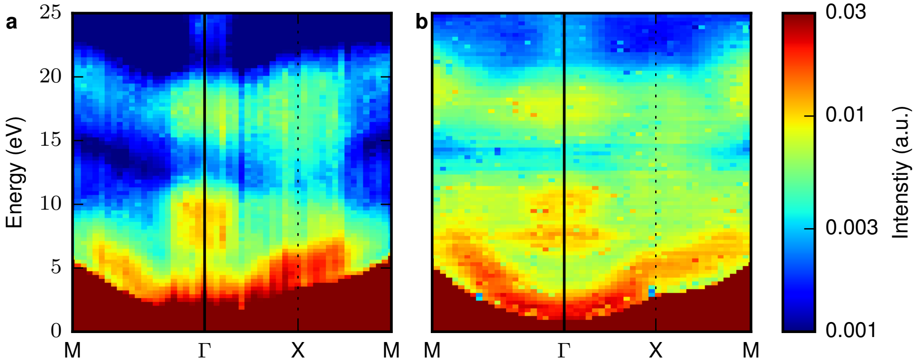

FIGURE 7.6: a) ARRES map of $LaAlO_3/SrTiO_3$ on $Ca_2Nb_3O_{10}$ nanosheets (sample C) and b) ARRES map of $LaAlO_3$ on $SrTiO_3$ substrate (sample D). On both samples 5 unit cells of $LaAlO_3$ have been grown. Both images are on the same energy scale.

and on a TiO_2-terminated $SrTiO_3$-substrate. Comparing the IV-curves to earlier measurements on conducting and non-conducting samples in chapter 6 suggests that the interface between the $LaAlO_3$ and $SrTiO_3$ should show conductivity.

The possible presence of a 2-DEG at the $LaAlO_3/SrTiO_3$ interface can be probed in more detail by comparing ARRES[16] measurements of the $LaAlO_3/SrTiO_3$/nanosheets heterostructure (Fig. 7.6a, sample C) and the reference sample D of $LaAlO_3$ on a TiO_2-terminated $SrTiO_3$-substrate (Fig. 7.6b).

ARRES is, as explained earlier, an extension of the IV-curve by recording electron reflectivity maps as a function of landing energy and in-plane wave vector $k_{||}$ of the electrons, forming a kind of band structure map of the unoccupied bands above the vacuum energy. Both of the ARRES maps show similar features. Most pronounced is the band gap just above the mirror mode energy, the lowest energy when the electrons just touch the sample, for all $k_{||}$. Furthermore, pronounced features can be found at energies between 7 and 10 eV and around 17 eV both around the Γ-point. Band gaps are presented in ARRES as maxima because the probing low-energy electrons are reflected with high probability if no states exist in the material at that energy (E) and in-plane wave vector ($k_{||}$). The dispersion of band gaps and bands was also similar for both samples, e.g. the band gap around 17 eV extends parabolically to the M-point around 20 eV and the band gaps around the X-point at 10 and 17 eV connect.

The differences between the two maps can partially be explained by the different data acquisition methods used. For reference sample D, data is obtained from diffraction patterns, averaging a 20 µm^2 area. On the other hand, for the nanosheet sample C, data from a 20 µm^2 area would average the signal of multiple flakes. Due to the random orientation of the flakes, the in-plane wave vector of the electrons would be badly defined in the crystal bases. This can be solved by taking real-space

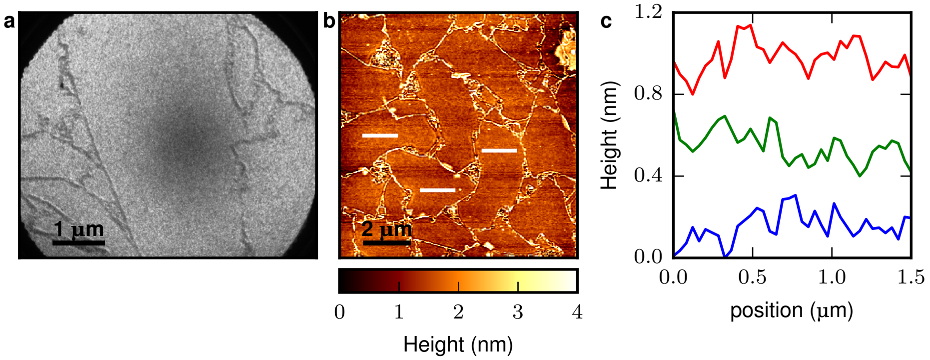

FIGURE 7.7: a) Bright field image at 16 eV and b) AFM image of the $LaAlO_3/SrTiO_3/Ca_2Nb_3O_{10}$ heterostructure (sample C). c) Line profiles of the relative height difference on the nanosheets, profiles from bottom to top correspond to white lines in (b) from left to right. The dark area in the center of image (a) is due to an inhomogeneous channel plate.

data, where the signal of a single flake can be selected in the post processing[16]. In order to take real-space images the specular diffraction spot has to be selected by an aperture during acquisition. Due to the finite size of the aperture, an average is taken over the specular diffraction spot. This comes with the advantage of filtering out the contribution of the surface roughness in the electron reflectivity signal. However, due to misalignment of the aperture, slight intensity variations can occur. These misalignments probably cause the reduction in overall intensity and the striped artifacts in Fig. 7.6a. Filtering out of the surface roughness from the electron reflectivity data is also achieved in the diffraction data by averaging a few pixels around the maximum of the specular diffraction spot.

Finally, we investigated the surface of the $LaAlO_3/SrTiO_3/Ca_2Nb_3O_{10}$ heterostructure. Figure 7.7 shows a LEEM (a) and an AFM image (b). The nanosheets were still clearly visible. Line profiles were taken to obtain the surface roughness on top of a single flake (Fig. 7.7c). The surface roughness was less than a unit cell, pointing to an atomically flat surface.

7.4 Discussion

The first examples of perovskite growth on $Ca_2Nb_3O_{10}$ nanosheets in the literature already showed they are promising candidates for transfer of TMO devices to literally any substrate.

Here we show how low-energy electron microscopy studies can help to find the growth conditions and annealing steps required to build TMO devices on $Ca_2Nb_3O_{10}$ nanosheets. While the growth of $SrTiO_3$, $SrRuO_3$ and $BiFeO_3$ have been shown before[3], only relatively thick layers have been grown, without layer-by-layer growth control. We found that such control is not possible directly on top of the nanosheets. A buffer layer is required to create a flat and well defined surface on the atomic scale. For $SrTiO_3$, we showed the surface changes during growth of the first 7 unit cells and this number seems to be required for the well defined surface with $SrTiO_3$-substrate-like properties. This is much more than the 1 to 2 unit cells range in which the IV-curve changes when growing $LaAlO_3$ on $SrTiO_3$.

For the first $SrTiO_3$ layer we could not obtain a crystalline film at temperatures above 660 °C and degradation of the diffraction pattern was observed before the growth started. In literature however films are grown at 700 °C[3,6]. The main difference between the conditions in Ref. 3, 6 and those reported here is the oxygen background pressure. From this we infer that nanosheets degrade in low oxygen pressures for temperatures above 660 °C. This could be caused by the reduction of oxygen in the nanosheet.

The $SrTiO_3$ film grown did not show a well-defined surface. This could be improved by annealing, which suggests that the growth temperature was too low for ideal growth. The just grown surface showed an IV-curve with many similarities to a SrO-terminated $SrTiO_3$, while after annealing at 770 °C the surface showed the IV-curve TiO_2-terminated $SrTiO_3$. This is somewhat surprising since the SrO-terminated reference curve was taken at a temperature of 770 °C, from which it can be concluded that the SrO-termination is stable at this temperature. However, the SrO-terminated reference sample was fully covered with a double layer of SrO. From this we conclude that the SrO on the grown $SrTiO_3$ is only seen on the surface due to the rough surface where it is unstable at high temperatures. Annealing reorders the surface to a well defined TiO_2-termination.

While the nanosheets were unstable at temperatures above 660 °C, no degradation is found during the annealing of the $SrTiO_3$ film on nanosheets at 770 °C. Apparently the $SrTiO_3$ layer protects the nanosheets from oxygen reduction. However, the temperature dependence is still fragile and temperatures above 770 °C are not recommended at these low pressures.

Once a well-defined surface is obtained, layer-by-layer growth of $LaAlO_3$ can be achieved. We do not find any difference between the growth of $LaAlO_3$ on our $SrTiO_3$ film on nanosheets and a TiO_2-terminated $SrTiO_3$ substrate. The final ARRES map is very similar to ARRES maps found on conducting $LaAlO_3/SrTiO_3$ heterostructures as found in chapter 6. From the comparison with the measurements performed in chapter 6, we conclude all the requirements such as surface termination en stoichiometry are in place for the $LaAlO_3/SrTiO_3$-interface to show conductivity. We however could not confirm conductivity by transport measurement because of the difficulty to contact the interface of individual flakes.

Lastly we stress the opportunity of electronic gating of TMO devices on nanosheets. We infer a minimum $SrTiO_3$ buffer layer thickness of only ≈7 unit cells. For bottom gating of devices this would mean a gate dielectric of only 7 unit cells plus the thickness of the nanosheets, which was reported to be between 1.5 and 4 nm[6–9]. This would give an upper bound of the gate dielectric of only 7 nm and provide a great possibility to improve bottom gating.

7.5 Summary

In this chapter we have shown the growth of a $LaAlO_3/SrTiO_3$ heterostructure on $Ca_2Nb_3O_{10}$ nanosheets on Si. Low-energy electron microscopy has allowed us to combine crystal information by LEED with real-space images of the nanosheets and band structure information by ARRES. The ability of in-situ PLD allows to combine this with growth analysis.

For the starting $SrTiO_3$-layer on the nanosheets, no layer-by-layer growth can be observed. The $SrTiO_3$ grown was not flat and the surface changed up to ≈7 unit cells as was obtained from IV-curves. A flat TiO_2-terminated $SrTiO_3$ surface could be obtained by annealing the grown $SrTiO_3$ at 770 °C. A combination of diffraction and real-space imaging showed that the $SrTiO_3$ crystal orientation depends on the underlying $Ca_2Nb_3O_{10}$ crystal structure. Between the nanosheets no crystalline $SrTiO_3$ is formed. On the flat TiO_2-terminated $SrTiO_3$ surface, layer-by-layer growth of $LaAlO_3$ could be observed.

With a combination of IV-curves and ARRES maps we could analyze the surface of the grown $LaAlO_3$ by comparing it to earlier measurements. The growth of $LaAlO_3$ showed the fingerprint of a conducting $LaAlO_3/SrTiO_3$ heterostructure found in chapter 6. Conductance however could not be measured, as this was obstructed by the difficulty to measure on as single nanosheet.

The minimum thickness of the $SrTiO_3$/nanosheet stack was determined to be around 7 nm. This implies a great opportunity to improve bottom gating of the $LaAlO_3/SrTiO_3$ interface.

References

[1] A. Ohtomo and H. Y. Hwang, *A high-mobility electron gas at the* $LaAlO_3/SrTiO_3$ *heterointerface*, Nature **427**, 423 (2004).

[2] J. W. Park, D. F. Bogorin, C. Cen, D. A. Felker, Y. Zhang, C. T. Nelson, C. W. Bark, C. M. Folkman, X. Q. Pan, M. S. Rzchowski, J. Levy, and C. B. Eom, *Creation of a two-dimensional electron gas at an oxide interface on silicon*, Nature Communications **1**, 94 (2010).

[3] A. P. Dral, M. Nijland, G. Koster, and J. E. ten Elshof, *Film transfer enabled by nanosheet seed layers on arbitrary sacrificial substrates*, APL Materials **3**, 056102 (2015).

[4] M. Nijland, S. Kumar, R. Lubbers, D. H. A. Blank, G. Rijnders, G. Koster, and J. E. ten Elshof, *Local Control over Nucleation of Epitaxial Thin Films by Seed Layers of Inorganic Nanosheets*, ACS Applied Materials & Interfaces **6**, 2777 (2014).

[5] T. Shibata, K. Fukuda, Y. Ebina, T. Kogure, and T. Sasaki, *One-Nanometer-Thick Seed Layer of Unilamellar Nanosheets Promotes Oriented Growth of Oxide Crystal Films*, Advanced Materials **20**, 231 (2008).

[6] H. Yuan, M. Nguyen, T. Hammer, G. Koster, G. Rijnders, and J. E. ten Elshof, *Synthesis of* $KCa_2Nb_3O_{10}$ *Crystals with Varying Grain Sizes and Their Nanosheet Monolayer Films As Seed Layers for PiezoMEMS Applications*, ACS Applied Materials & Interfaces **7**, 27473 (2015).

[7] H. Tetsuka, H. Takashima, K. Ikegami, H. Nanjo, T. Ebina, and F. Mizukami, *Nanosheet Seed-Layer Assists Oriented Growth of Highly Luminescent Perovskite Films*, Chemistry of Materials **21**, 21 (2009).

[8] M. Osada, K. Akatsuka, Y. Ebina, H. Funakubo, K. Ono, K. Takada, and T. Sasaki, *Robust High-nkappa Response in Molecularly Thin Perovskite Nanosheets*, ACS Nano **4**, 5225 (2010).

[9] K. Akatsuka, G. Takanashi, Y. Ebina, M.-a. Haga, and T. Sasaki, *Electronic Band Structure of Exfoliated Titanium- and/or Niobium-Based Oxide Nanosheets Probed by Electrochemical and Photoelectrochemical Measurements*, The Journal of Physical Chemistry C **116**, 12426 (2012).

[10] S. M. Schramm, J. Kautz, A. Berghaus, O. Schaff, R. M. Tromp, and S. J. van der Molen, *Low-energy electron microscopy and spectroscopy with ESCHER: Status and prospects*, IBM Journal of Research and Development **55**, 1:1 (2011).

[11] R. Tromp, J. Hannon, A. Ellis, W. Wan, A. Berghaus, and O. Schaff, *A new aberration-corrected, energy-filtered LEEM/PEEM instrument. I. Principles and design*, Ultramicroscopy **110**, 852 (2010).

[12] S. M. Schramm, A. B. Pang, M. S. Altman, and R. M. Tromp, *A Contrast Transfer Function approach for image calculations in standard and aberration-corrected LEEM and PEEM*, Ultramicroscopy **115**, 88 (2012).

[13] R. Tromp, J. Hannon, W. Wan, A. Berghaus, and O. Schaff, *A new aberration-corrected, energy-filtered LEEM/PEEM instrument II. Operation and results*, Ultramicroscopy (2013).

[14] M. Kawasaki, K. Takahashi, T. Maeda, R. Tsuchiya, M. Shinohara, O. Ishiyama, T. Yonezawa, M. Yoshimoto, and H. Koinuma, *Atomic Control of the* $SrTiO_3$ *Crystal Surface*, Science **266**, 1540 (1994).

[15] J. B. Hannon, J. Sun, K. Pohl, and G. L. Kellogg, *Origins of Nanoscale Heterogeneity in Ultrathin Films*, Physical Review Letters **96**, 246103 (2006).

[16] J. Jobst, J. Kautz, D. Geelen, R. M. Tromp, and S. J. van der Molen, *Nanoscale measurements of unoccupied band dispersion in few-layer graphene*, Nature Communications **6**, 8926 (2015).

[17] M. Horn-von Hoegen, *Growth of semiconductor layers studied by spot profile analysing low energy electron diffraction Part I1*, Zeitschrift fr Kristallographie - Crystalline Materials **214**, 591 (1999).

Summary

The ongoing performance increase of electronics will reach its limit when Si-based devices reach the size of a few atoms only. As an alternative for Si, transition-metal oxides (TMOs) form an interesting materials group with new physical properties, which could be used for performance increase and novel devices. Research and development of TMO devices has long been held back by the difficulty to grow these materials. The development of pulsed laser deposition (PLD) and reflection high-energy electron diffraction (RHEED) made it possible to control growth up to unit cell precision. However, to really understand the growth process and the evolution in physical properties of the TMOs, it is important to further characterize the material during this growth process. Most of the common analysis techniques cannot be used in-situ due to the high growth temperatures and oxygen pressures. Hence, characterization of films is typically done afterwards when the full film has been grown. Here we use low-energy electron microscopy (LEEM) as a technique that cannot only work under these conditions and, when combined with PLD, control the thickness with sub-unit cell precision, but that can also directly monitor the structural and electronic properties during growth.

A very interesting phenomenon in TMOs is the presence of a two-dimensional electron gas (2-DEG) between the band insulators $LaAlO_3$ and $SrTiO_3$, which forms when at least four unit cells of $LaAlO_3$ are deposited on a $SrTiO_3$ substrate. Despite a considerable amount of research in the last years, there are many open questions around the formation of this electron gas. Our combination of LEEM and PLD allows us to study the layer by layer formation of this heterostructure in real time.

After a general introduction in chapter 1, chapter 2 provides a more detailed background on TMOs with the perovskite structure and especially the $LaAlO_3$/ $SrTiO_3$ heterostructure. The two most important parameters for this thesis are bulk stoichiometry and surface termination. From literature it is known that the heterostructure only shows conductance when the $SrTiO_3$ substrate is TiO_2-terminated. Furthermore, it has been shown that the $LaAlO_3$ film has to be Al-rich, and that oxygen vacancies play an important role in the conductance.

I have used LEEM to study the properties and growth of $LaAlO_3$ and $SrTiO_3$. This technique is described in detail in chapter 3. Low-energy electrons used in LEEM make it a surface sensitive technique. Moreover, LEEM allows for real-time imaging at elevated temperatures up to 1500 °C with oxygen pressures up to 1×10^{-4} mbar. A combination of real space (LEEM) and diffraction (LEED) imaging results in complementary information about morphology and structure. Apertures allow to obtain this information on the nanometer scale. LEEM-IV (intensity versus voltage) curves can be used to probe the surface electronic structure. This can be

extended to a full band-structure map of the unoccupied bands by a new technique called angle-resolved reflection electron spectroscopy (ARRES). Here the energy dependence is not only measured for the specular reflection, but also for non-zero in-plane wave vectors, which makes it possible to obtain the dispersion of these bands. Chapter 3 describes how the resolution of this technique is extended by a combination of automation and extension of the dynamic range of the camera. Furthermore, spot-profile-analysis (SPA)-LEED is introduced. Film growth can be controlled with layer-by-layer precision by analyzing the width of the specular diffraction spot.

As a first set of results from using LEEM, chapter 4 describes the $LaAlO_3$ surface after high-temperature annealing. A mixed ordered surface of an unreconstructed AlO_2 surface and a reconstructed ($\sqrt{5}\times\sqrt{5}\,\mathrm{R}26$) LaO surface is found, with the LaO fraction being about one third. These results are not different when the annealing is performed in UHV or air. The ordering of the surface termination can be imaged starting from small $\sqrt{5}\times\sqrt{5}\,\mathrm{R}26$ islands until stripes in the middle of the terraces of AlO_2. Atomic force microscopy (AFM) shows the reconstructed LaO lies below the surrounding AlO_2 terraces. Furthermore, the IV-curves can be compared to a single AlO_2-terminated sample, confirming the terraces are AlO_2 with LaO strips.

Chapter 5 shows the first results from the combined PLD-LEEM system. I demonstrate its abilities by studying the growth of homo-epitaxial $SrTiO_3$. The combination allows for a unique possibility for in-situ growth analysis by SPA-LEED, real-space imaging and probing of the unoccupied band structure with ARRES. For the growth of homo-epitaxial $SrTiO_3$ we observe layer-by-layer growth, which changes slowly with thickness to a more three-dimensional growth. The electronic structure of the grown $SrTiO_3$ is different from the TiO_2-terminated $SrTiO_3$ substrate. This can be caused by oxygen vacancies due to the low oxygen pressure and by off-stoichiometric growth. The IV-curve shows the signature of a SrO termination, which can be restored to the IV-curve of the TiO_2-termination by buffered HF-etching (hydrofluoric acid) and annealing with the same parameters as the single termination procedure performed at new substrates. The conclusion is that our growth is Sr-rich.

In chapter 6 we use the combination of LEEM and PLD developed in the previous chapter to study the $LaAlO_3/SrTiO_3$ heterostructure. The electron reflectivity or ARRES maps give information about the electronic properties of the surface as it develops during growth, at the growth temperature. We make a connection between our measurements and the electronic properties of the $LaAlO_3/SrTiO_3$ interface by comparing samples that do and do not show a conducting interface. We find distinct signatures for the conducting versus non-conducting interfaces independent of their growth conditions. This, in principle, allows us to predict during growth whether a sample is going to show a conducting interface. From literature it is known that the two important ingredients related to the conducting interface are the surface termination of the $SrTiO_3$ and the stoichiometry of the $LaAlO_3$. We find that these same two ingredients are responsible for those distinct signatures. We demonstrate this by three samples, an TiO_2-terminated

$SrTiO_3$ substrate with an Al-rich $LaAlO_3$ film, a SrO-terminated $SrTiO_3$ substrate with an Al-rich $LaAlO_3$ film, and a TiO_2-terminated $SrTiO_3$ sample with a La-rich $LaAlO_3$ film. Combining the results, we show that substrate B-site termination (TiO_2) together with Al-rich growth, leads to a B-site terminated surface (AlO_2) and a conducting interface. On the other hand A-site termination (SrO) or La-rich growth leads to an A-site terminated (LaO) surface and a non-conducting interface.

Finally in chapter 7 the various earlier observations and data come together. To overcome the limitations of the $SrTiO_3$ substrate onto which the $LaAlO_3/SrTiO_3$ heterostructure is grown, we use $Ca_2Nb_3O_{10}$-nanosheets in the form of micron-sized flakes as seed layers to grow the heterostructure on any substrate. In this chapter I show how LEEM can be used to investigate the growth on such flakes. We can image the $Ca_2Nb_3O_{10}$-nanosheets in LEEM and follow the growth on the flakes. Growth control on such small areas would be impossible by other techniques. We show that the first layers of $SrTiO_3$ do not grow in a layer-by-layer mode due to the imperfections in the nanosheets. The $SrTiO_3$ can only be grown at relative low temperatures, probably as a consequence of the low oxygen background pressure. At these temperatures we have imperfect $SrTiO_3$ growth as seen before in chapter 5. The $SrTiO_3$ can be improved by annealing. After annealing we find a TiO_2-terminated $SrTiO_3$ layer. Onto this, we can grow $LaAlO_3$ in a layer-by-layer mode. Such growth is very comparable to the growth on a $SrTiO_3$ substrate. The final ARRES map shows many similarities with the ARRES maps on the conducting interface in chapter 6, suggesting that also this interface is conducting. We could not verify this, however, with conductance measurements. The nanosheets bear promise to make devices of the $LaAlO_3/SrTiO_3$ heterostructure with thin $SrTiO_3$ bottom layer, allowing effective bottom gating.

Samenvatting

Het verkleinen van elektronica zal zijn limiet bereiken wanneer de kleinste onderdelen niet groter zijn dan een aantal atomen. Om toch vooruitgang te boeken moet er gekeken worden of de huidige elektronica die gebaseerd is op silicium (Si) vervangen kan worden door andere materialen. Als alternatief voor Si vormen overgangsmetaaloxiden (OMO) een interessante groep materialen, met andere fysische eigenschappen. Onderzoek naar deze fysische eigenschappen moet de vraag beantwoorden of elektronica efficiënter gemaakt kan worden. Onderzoek naar en ontwikkeling van OMO schakelingen is lang vertraagd doordat het moeilijk was dunne films met hoge kwaliteit te maken. De ontwikkeling van gepulste laser depositie (PLD) en reflectie hoge-energie elektronen diffractie (RHEED) maakten het mogelijk om de groei te controleren tot op het niveau van een enkele atoomlaag of eenheidscel. Om beter te begrijpen hoe tijdens de groei van de dunne OMO films de fysische eigenschappen veranderen, hebben we meer nodig dan RHEED. De meeste andere analyse technieken werken echter niet bij de hoge temperaturen en zuurstofdrukken, die nodig zijn tijdens de groei van deze materialen. Daarnaast is het belangrijk om een techniek te gebruiken die niet in contact komt met het preparaat om het groei proces niet te beïnvloeden. Hier introduceren we lage-energie elektronen microscopie (LEEM) als techniek die kan werken onder deze extreme groei-omstandigheden en een scala aan informatie kan geven tijdens het proces. Naast controle over de laagdikte van de groeiende film krijgen we ook structurele en elektronische informatie van de bovenste laag van de film.

Een interessant verschijnsel in OMOn is de aanwezigheid van een tweedimensionaal elektronengas (2-DEG) tussen de band isolatoren $LaAlO_3$ en $SrTiO_3$. Opmerkelijk is dat het 2-DEG alleen ontstaat wanneer er minimaal vier eenheidscellen $LaAlO_3$ gedeponeerd zijn op het $SrTiO_3$. Ondanks veel onderzoek in de afgelopen jaren zijn er nog veel open vragen rond de vorming van het elektronengas. Met onze combinatie van LEEM en PLD kunnen we de vorming van dit systeem laag voor laag in "real time"bestuderen.

Na een algemene introductie in hoofdstuk 1, geeft hoofdstuk 2 een gedetailleerdere beschrijving van OMOn met de perovskiet structuur en in het bijzonder het $LaAlO_3/SrTiO_3$ systeem. De perovskiet structuur heeft de chemische formule ABO_3 met een kubische structuur. Deze kan gezien worden als opgebouwd uit lagen met de chemische formule AO en BO_2. De belangrijkste parameters die in dit proefschrift zijn bekeken bij de groei van $SrTiO_3$ en $LaAlO_3$ zijn de terminatie van de materialen (ligt de AO-laag of de BO_2-laag aan het oppervlak) en de stoichiometrie, dit is de verhouding A versus B. Deze verhouding is in het ideale geval een op een, maar wijkt in de praktijk af. Uit de literatuur is bekend dat het $LaAlO_3/SrTiO_3$ systeem alleen geleiding vertoont wanneer het $SrTiO_3$ substraat een TiO_2-oppervlak heeft en de $LaAlO_3$ film Al-rijk is. Ook spelen zuurstofvacatures in het $SrTiO_3$ een belangrijke rol in de geleiding.

In dit proefschrift is LEEM het belangrijkste instrument om de eigenschappen van het $LaAlO_3$ en $SrTiO_3$ te bestuderen. Deze techniek wordt in detail beschreven in hoofdstuk 3. Door het gebruik van laagenergetische elektronen is de LEEM zeer oppervlaktegevoelig. Daarnaast is het mogelijk om met LEEM tijdens de groei het systeem te bekijken, te werken met preparaattemperaturen tot 1500 °C, zuurstof achtergronddrukken tot 1×10^{-4} mbar en met een resolutie van 1,5 nanometer. Een combinatie van microscopie (LEEM) en diffractiemetingen (LEED) geeft een totaal beeld van morfologie en de atomaire structuur. LEEM-IV (intensiteit (I) versus spanning (V)) curves maken het mogelijk om de onbezette banden van de elektronische structuur af te beelden. Deze curves worden in eerste instantie als handtekening van het oppervlaktemateriaal gebruikt, maar de IV-curve kan worden uitgebreid tot een volledige bandstructuur van de onbezette banden door een nieuwe techniek genaamd hoekopgeloste reflectie elektron spectroscopie (ARRES). Met deze techniek wordt niet alleen de energie-afhankelijkheid van de elektronen, maar ook hun impuls, in het vlak van het preparaat, gemeten om de dispersie van de banden te verkrijgen. Aan het eind van hoofdstuk 3 beschrijf ik hoe de resolutie van deze techniek wordt uitgebreid met een combinatie van automatisering en uitbreiding van het dynamisch bereik van de camera. Verder introduceer ik spotprofiel analyse voor lage-energie elektronen diffractie, SPA-LEED. De filmgroei kan met eenheidscelprecisie gecontroleerd worden door het bepalen van de spotbreedte van de primaire diffractiespot.

Als een eerste set van resultaten van de LEEM, beschrijft hoofdstuk 4 het $LaAlO_3$ oppervlak na gloeien op hoge temperatuur. Het resultaat is een gemengd oppervlak met gebieden met LaO en met AlO_2 terminatie. De LaO gebieden vertonen een $\sqrt{5} \times \sqrt{5}\,\mathrm{R}26$ reconstructie, waarbij er eens in de 5 eenheidscellen een La atoom mist. De verhouding LaO tot AlO_2 oppervlak is ongeveer 1:2. Dit resultaat is onafhankelijk van druk en is zowel gevonden na gloeien in lucht als in vacuüm. De vorming van de LaO eilanden met $\sqrt{5} \times \sqrt{5}\,\mathrm{R}26$ reconstructie kan worden afgebeeld tijdens het gloeien. Eerst ontstaan er kleine eilanden, die langzaam strepen om het midden van de atomaire terrassen vormen. Met atomic force microscopie (AFM) kan worden aangetoond dat de LaO eilanden een halve eenheidscel lager liggen dan het omringende AlO_2 terras. Bovendien kunnen de IV-curves worden vergeleken met een preparaat dat na chemische behandeling een volledig AlO_2 oppervlak vertoont. Dit bevestigt dat de terrassen AlO_2 oppervlak vertonen en de eilanden dus LaO zijn.

Hoofdstuk 5 toont de eerste resultaten van het gecombineerde LEEM-PLD systeem door het bestuderen van groei van $SrTiO_3$ op $SrTiO_3$. Deze combinatie geeft de unieke mogelijkheid om in-situ de groei te analyseren door het combineren van SPA-LEED, afbeelden van het oppervlak en het meten van de onbezette banden structuur met ARRES. We zien tijdens de depositie van homo-epitaxiaal $SrTiO_3$ dat de groei langzaam verandert van laag voor laag naar een driedimensionale groei. Dit gaat gepaard met een verandering in de elektronische structuur van het gegroeide $SrTiO_3$ ten opzichte van het TiO_2 getermineerde $SrTiO_3$ substraat. Dit verschil kan veroorzaakt worden door zuurstofvacatures of door off-stoichiometrische groei waarbij de gegroeide laag meer strontium (Sr) bevat dan titanium (Ti). Als we de IV-curve meten vinden we de handtekening van een SrO getermineerd oppervlak. Dit kan teruggebracht worden tot een TiO_2 terminatie met dezelfde procedure als gebruikt wordt voor nieuw geleverde substraten. We concluderen dat onze groei strontium-rijk is.

In hoofdstuk 6 gebruiken we de combinatie van LEEM en PLD om het $LaAlO_3$/$SrTiO_3$ systeem te bestuderen. Elektronenreflectie of ARRES geeft informatie over de elektronische eigenschappen van het oppervlak tijdens de groei, bij de groei temperatuur. We vinden een verband tussen onze metingen en de elektronische eigenschappen van het $LaAlO_3$/$SrTiO_3$ grensvlak door preparaten zonder en met een geleidend grensvlak te vergelijken. Er is een duidelijk verschil in de IV-curve onafhankelijk van de groei-condities. Dit geeft ons de mogelijkheid om tijdens groei te voorspellen of het preparaat een geleidend grensvlak gaat vertonen. Uit de literatuur is het bekend dat er twee belangrijke ingrediënten zijn die het ontstaan van het geleidende grensvlak beïnvloeden. Dit zijn de oppervlakteterminatie van het $SrTiO_3$ hetgeen TiO_2 moet zijn en de stoichiometrie van het $LaAlO_3$ waarbij er meer aluminium (Al) moet zijn dat lanthaan (La). Het zijn deze twee ingrediënten die het karakteristieke verschil in de IV-curve geven. We demonstreren dit aan de hand van drie preparaten: een TiO_2 getermineerd $SrTiO_3$ substraat met een Al-rijke $LaAlO_3$ film, een SrO getermineerd $SrTiO_3$ substraat met een Al-rijke $LaAlO_3$ film en een TiO_2 getermineerd $SrTiO_3$ substraat met een La-rijke $LaAlO_3$ film. Het combineren van deze resultaten laat zien dat een B-site (TiO_2) getermineerd substraat samen met een Al-rijke $LaAlO_3$ groei resulteert in een B-site (AlO_2) getermineerd oppervlak en een geleidend grensvlak. Daarentegen leidt een A-site (SrO) terminatie of een La-rijke groei tot een A-site (LaO) oppervlak en een niet geleidend grensvlak.

Tenslotte beschrijven we in hoofdstuk 7 de groei van het $LaAlO_3$/$SrTiO_3$ systeem op nanovellen van $Ca_2Nb_3O_{10}$. Deze nanovellen hebben een perovskiet kristalstructuur met een roosterconstante dichtbij die van $SrTiO_3$ en kunnen dienen als grondlaag om de beperkingen van het gebruik van $SrTiO_3$ substraten te omzeilen, door deze grondlaag op een willekeurig substraat te plaatsen. In dit hoofdstuk laat ik zien hoe LEEM gebruikt kan worden om de groei te observeren op deze nanovellen ter grootte van maximaal een micron. Hierbij is de mogelijkheid van de LEEM om kleine oppervlakten te bestuderen essentieel. We laten zien dat $SrTiO_3$ op deze nanovellen niet laag bij laag groeit. Dit kan veroorzaakt worden door onvolkomenheden in de nanovellen of doordat we het $SrTiO_3$ groeien bij een relatief lage temperatuur van 660 °C. De nanovellen blijken bij de ook al relatief lage zuurstof achtergronddruk die we gebruiken te beschadigen als de temperatuur verder verhoogd wordt. In hoofdstuk 5 hebben we eerder gezien dat de groei van $SrTiO_3$ niet optimaal is bij deze condities. We zien dat het $SrTiO_3$ verbeterd kan worden door de temperatuur na depositie de verhogen naar 770 °C. De nanovellen lijken deze temperatuur nu aan te kunnen doordat ze beschermd worden door de $SrTiO_3$ laag.

Na deze behandeling vinden we een oppervlak dat atomair vlak is met een TiO_2 handtekening. De volgende stap is het deponeren van $LaAlO_3$. Dit laat dezelfde structuur zien als het deponeren van $LaAlO_3$ op een $SrTiO_3$ substraat en we vinden dan ook een handtekening die overeenkomt met de geleidende preparaten van hoofdstuk 6. Helaas hebben we geen geleiding kunnen meten, maar dit is ook niet eenvoudig op de kleine oppervlakte van een micron. De gemaakte structuren op de nanovellen zouden kunnen helpen bij het maken van elektronische onderdelen met zeer dunne $SrTiO_3$ lagen als onderdeel van de heterostructuur, waardoor de elektronische eigenschappen van het elektronengas gemakkelijker kunnen worden beïnvloed vanaf de substraatkant.

Curriculum Vitae

Alexander Johannes Hendrikus van der Torren

Born 23 October 1987 in Heerlen.

Education

2012–2016	Ph.D. thesis, Universiteit Leiden *Growing oxide thin films in a Low-Energy Electron Microscope* under supervision of Dr.ir. S. J. van der Molen and Prof.dr. J. Aarts.
2009–2012	Master in physics, Universiteit Leiden Internship 1: Quantum Optics and Quantum Information Universiteit Leiden Internship 2: Nanoelectronics group Basel University, Switzerland
2006–2009	Bachelor in physics, Universiteit Leiden
1999–2006	Grammar school, Goudse Waarden, Gouda

List of publications

- A. J. H. van der Torren, H. Yuan, J. Jobst, J. ten Elshof, M. Huijben, A. J. H. M. Rijnders, G. Koster, S. J. van der Molen, and J. Aarts, *Growing a* $LaAlO_3/SrTiO_3$ *heterostructure on* $Ca_2Nb_3O_{10}$ *nanosheets*, in preparation.
- A. J. H. van der Torren, Z. Liao, C. Xu, N. Gauquelin, C. Yin, J. Aarts, and S. J. van der Molen, *Finding signatures of the conducting* $LaAlO_3/SrTiO_3$ *interface at the growth temperature by electron reflection*, in preparation.
- A. J. H. van der Torren, S. J. van der Molen, and J. Aarts, *Imaging pulsed laser deposition growth of homo-epitaxial* $SrTiO_3$ *by Low-Energy Electron Microscopy*, Nanotechnology (2016), accepted.
- J. Jobst, A. J. H. van der Torren, E. E. Krasovskii, J. Balgley, C. R. Dean, R. M. Tromp, and S. J. van der Molen, *Quantifying Electronic Band Interactions in Graphene, Hexagonal Boron Nitride and their Heterostructures*, Nature Communications (2016), accepted.
- C. Xu, H. Du, A. J. H. van der Torren, J. Aarts, C.-L. Jia, and R. Dittmann, *Formation mechanism of Ruddlesden-Popper-type antiphase boundaries during the kinetically limited growth of Sr rich* $SrTiO_3$ *thin films* (2016), submitted to Scientific Reports.
- G. Mattoni, P. Zubko, F. Maccherozzi, A. J. H. van der Torren, D. B. Boltje, M. Hadjimichael, N. Manca, S. Catalano, M. Gibert, Y. Liu, J. Aarts, J.-M. Triscone, S. S. Dhesi, and A. D. Caviglia, *Striped nanoscale phase separation at the metal-insulator transition of heteroepitaxial nickelates*, Nature Communications (2016), accepted.
- A. J. H. van der Torren, S. J. van der Molen, and J. Aarts, *Formation of a mixed ordered termination on the surface of* $LaAlO_3$(001), Physical Review B **91**, 245426 (2015).
- A. J. H. van der Torren, S. C. Yorulmaz, J. J. Renema, M. P. van Exter, and M. J. A. de Dood, *Spatially entangled four-photon states from a periodically poled potassium-titanyl-phosphate crystal*, Physical Review A **85**, 043837 (2012).

Acknowledgements

Here I would like to use the opportunity to thank the people who contributed to this thesis. First of all, Jan Aarts, my promotor who gave me the opportunity to work on this project. His experience in the field of perovskites and his trust in my work have been of great help. My copromotor Sense Jan van der Molen I would like to thank for always being available for discussion and his quick response and care about the LEEM. Furthermore, for the discussion about science and LEEM Ruud Tromp was always available.

From outside the university I am grateful for the discussions with Gertjan Koster from the university of Twente and for the helpful comments which he and Guus Rijnders from Twente gave around designing the PLD system. I am grateful for the people who supported me by making and measuring samples. Thanks to Zhaoliang Zhao and Huiyu Yuan for making samples at the university of Twente, Chencheng Xu for making samples in Jülich, Chunhai Yin and Nikita Lebedev for helping with samples in Leiden and Nicolas Gauquelin for measuring samples in Antwerp.

A big part of this thesis has been the development of a pulsed laser deposition system inside the low-energy electron microscope. This would not have been successful without the help of Ruud van Egmond and his colleagues at the fine mechanical department (FMD) for making all the parts. Special thanks to Marcel Hesselberth who was of great help when technical problems appeared and who always was available for discussion. His input in the discussion on the design of the pulsed laser deposition system was very valuable. Special thanks also to Daan Boltje, Johannes Jobst, Jaap Kautz, Daniël Geelen and Aniket Thete for discussions and working together on the LEEM. Also thanks to Ko Koning, Arno van Amersfoort, Peter van Veldhuizen and their colleagues from the electronic department (ELD).

I was happy to be able to work together with my two bachelor students Renger Zoonen and Lennert Prins and to receive support with sample preparation and measurements from Stefano Voltan, Amrita Singh, Kaveh Lahabi, Anne France and Thomas Mechielsen and other members of the MSM group. Federica Galli is acknowledged for helping me with the AFM. I would also like to acknowledge very efficient and friendly administrative assistance from Daniëlle Duijn, Ellie van Rijsewijk and Charlotte Laurense-Griffioen.

Finally, I would like to thank my friends and family, and especially my wife Antien Mooyaart for their continued support during the period of my PhD work.